The Lattice Constant of High Tc Superconductor La_2-_xSr_xCuO_4 in High Precision

山田, 浩志
九州大学理学研究科物理学専攻

https://doi.org/10.11501/3134852

出版情報：九州大学, 1997, 博士（理学）, 課程博士
バージョン：
権利関係：

The Lattice Constant of High T_C Superconductor $La_{2-x}Sr_xCuO_4$ in High Precision

山田浩志

The Lattice Constant of High T_c Superconductor $La_{2-x}Sr_xCuO_4$ in High Precision

Hiroshi Yamada

Contents

Summary

The temperature dependence of the lattice constant of $La_{2-x}Sr_xCuO_4$ single crystals with $x = 0.110$ and $x = 0.143$ has been measured by means of high resolution X–ray diffractometry. The measurements were made for the 6 0 0, 0 6 0 and 0 0 14 diffractions in the temperature range from 17 to 300 K through both the structural and superconducting phase transitions. Below the structural phase transition T_s, the temperature dependence of the lattice constants a and b indicates the deformation of CuO_2 square in CuO_6 octahedra into the rectangular lattice, in addition to the tilt of the octahedra. The transition is characterized by three–dimensional X–Y model with a critical exponent $\beta = 0.39 \pm 0.01$: this suggests that the transition takes place in three–dimensional interaction of the lattice construction even the structure consists of two–dimensional stacking. According to the observed thermal expansivity around the superconducting transition T_c, the uniaxial stress dependencies of T_c, (dT_c/dP_i), are obtained to be -10.8 and 18.9 respectively along a and c–axis. This suggests that the appearance of the superconductivity is strongly related to the lattice stresses accompanying with the deformation of the CuO_2 planes and the tilt of CuO_6 octahedra.

1 Introduction

Since the discovery of the copper–oxide–based high–T_c compounds by Bednortz and Müller [1], there have been a number of reports on unusual behaviour of the structural and elastic properties at the superconducting transition temperature T_c, and therefore, this brings a great deal of interest in studying the relation of superconductivity with the structural parameters. Direct indications for a structural response to the appearance of superconductivity have been shown by capacitance–dilatometer measurements: an anisotropic discontinuity of thermal expansivities at T_c has been observed in both YBa_2CuO_{7-x} [2, 3] and $La_{2-x}Sr_xCuO_4$ [4, 5]. By ultrasonic measurements, Nohara, Suzuki, Maeno, Fujita, Tanaka, and Kojima have also found a unusual lattice stiffening in the superconducting state, which contrasts with the continuous softening observed in most of the conventional superconductors [6].

$La_{2-x}M_xCuO_4$ (M=Sr, Ba, etc.) compounds have been very well studied to investige the relation between the lattice properties and an appearance of high–T_c superconductivity. As shown in Fig. 1 and 2, the crystal structure shows various change with temperature and doping [7] and the changes mean the deformation of the CuO_2 planes which is considered to be proper stage of the superconductivity. Both $La_{2-x}Sr_xCuO_4$ and $La_{2-x}Ba_xCuO_4$, which are abbreviated to LSCO and LBCO respectively, undergo a second–order tetragonal–to–orhtorhombic phase transition; It is well known that the CuO_6 octahedron tilts around either the $[1\ 1\ 0]_t$ or $[1\ \bar{1}\ 0]_t$ axis. Here subscripts indicate tetragonal unit cell. The tetragonal structure belongs to the space group I4/mmm, and is so-called HTT (high temperature tetragonal), and the orthorhombic structure to Bmab, as LTO (low temperature orthorhombic). The structural phase transiton temperature T_s monotonically decreases with increasing Sr or Ba concentration x: For $x = 0$ and 0.22, T_s is 540 and 0 K respectively. Superconductivity appears in a range $0.05 \leq x \leq 0.25$; the superconductive transition temperature T_c shows a maximum at 38 K for LSCO with $x \simeq 0.15$ [8] and at 30 K for LBCO with $x \simeq 0.15$ [9]. LBCO exhibits an additional structural transition from LTO to the second tetragonal phase LTT (low temperature tetragonal) belonging to $P4_2/ncm$ [9, 10, 11]. T_c is considerably suppressed in the LTT phase at $x \simeq 1/8$ [9], while the LTO–to–LTT phase transition occur in a fairly wide composition range(see Fig. 2). It is suggested that this suppression is caused by superlattice formation in the LTT phase [12]. LSCO also shows a small dip of phase boundary at $x \simeq 1/8$(see Fig. 1) [8], but no LTT phase is obserbed in X–ray and Neutron diffraction experiments. On the contrary, by means of the polarized EXAFS method, which

Table 1. The various measurements of the lattice strain in $La_{2-x}Sr_xCuO_4$.

Authors	specimen	method	Precision
Ono and Narita [16]	powder	X–ray(Rietveld analysis)	?
Maeta *et al.* [17]	single	X–ray(Bond method)	2×10^{-6}
Yang *et al.* [18]	single	X–ray	5×10^{-6}
Braden *et al.* [4]	single(twinned)	capacitance dilatometer	$< 10^{-9}$
Gugenberger *et al.* [5]	single(untwinned)	capacitance dilatometer	$10^{-8} - 10^{-9}$
Present work	single(twinned)	X–ray(ED–HADOX)	$1.7 - 3.9 \times 10^{-6}$

probes a local atomic structure, the coexistence of the local lattice distortions of LTO and LTT in a form like as domains were observed [13, 14]. Anomalous behaviour of the elastic constant was observed at 60 K, and this is interpreted as evidence of a frustrated phase transition with formation of LTT domains [6, 15]. Braden *et al.* [4] suggested that the evolution of the orthrohmbic distortion is forbidden by the onset of superconductivity. These results suggests an intimate correlation of the crystal structure with superconductivity in LSCO and LBCO materials.

The measurement of lattice constants is one of effective method to investigate a lattice distortion and a structural change. In spite of the fact, the investigation on the lattice constants as a function of temperature, in particular around T_c , has not been made in good enough accuracy for the discussion. As for LSCO, there have been only a few measurements on the lattice distortion around T_c: the measurements in literature are listed in Table 1. Ono and Narita have measured lattice constants with Sr concentration x =0.05, 0.10 and 0.15 by Rietveld analysis using X–ray powder diffraction data, and Maeta *et al.* and Yang *et al.* made the conventional X-ray diffraction measurements with the optimum Sr concentration $x = 0.15$. A number of data are also inadequate for clarification of relation of the appearance of superconductivity with lattice constant, and the results are in disagreement with each other

In the present paper, in order to determine the lattice constant as a function of temperature, a high–resolution X–ray diffraction experiment has been carried for high–quality single crystals with $x = 0.110$ and 0.143 in a temperature range 17–300 K and 10–76 K. The present study is the first measurement providing the complete information on the temperature dependence of lattice constants in a high precision. We will show that the HTT–to–LTO transition of LSCO has a three–dimensional nature despite that the crystal has a quasi–two–dimensional layered structure. The possibility of the existence of LTO–to–LTT structural phase transition obseved in LBCO are also discussed. Moreover, uniaxial stress (dT_c/dP_i) and strain ($dT_c/d\epsilon_i$) dependences of T_c are deduced from the discontinuity of a thermal expansivity at T_c using the Ehrenfest relation.

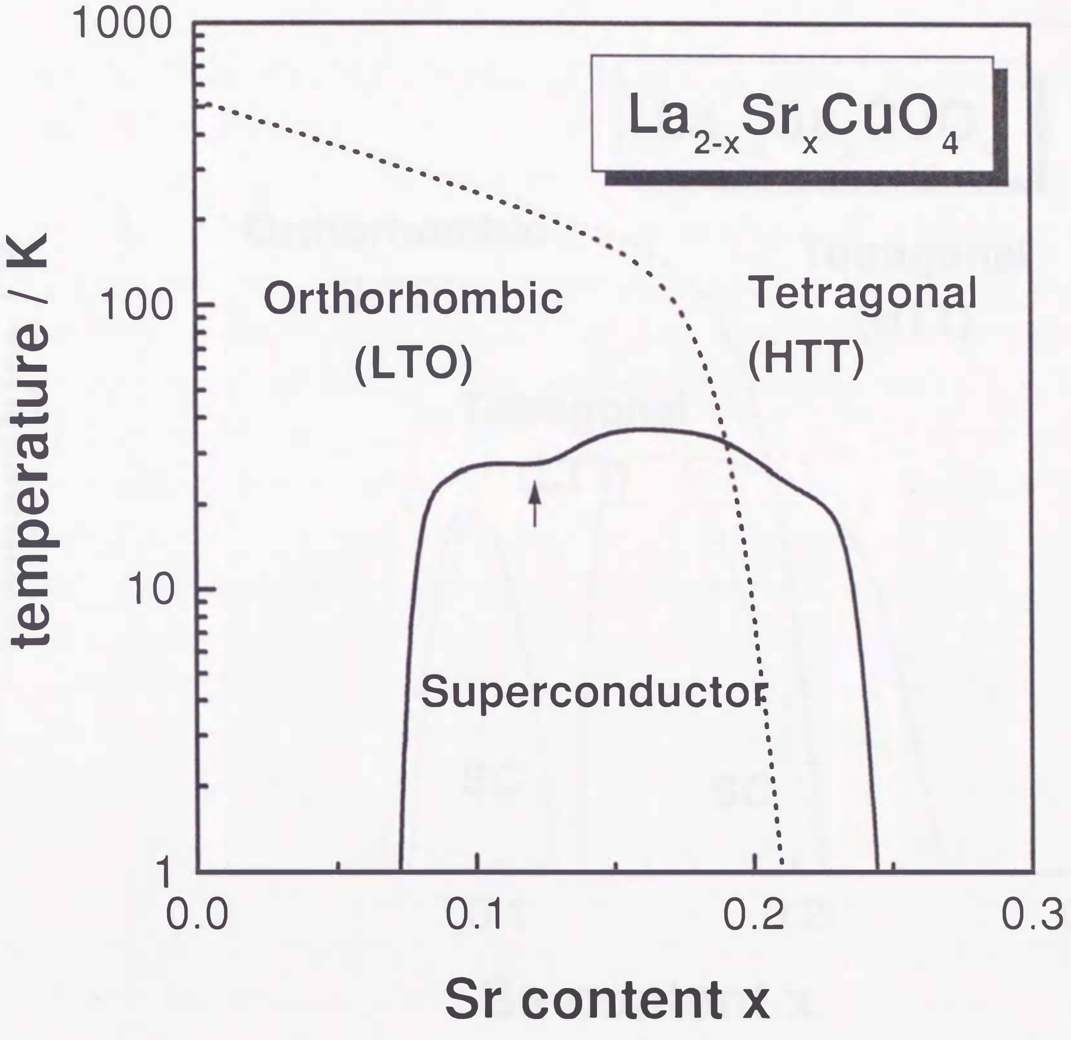

Figure 1: Phase diagram of LSCO. The boundaries of HTT–to–LTO phase transition and of superconducting phase transition are given in the dotted and solid lines respectively ; the dip on the phase boundary at $x \simeq 1/8$ mentioned in the text is indicated by an arrow. (after Fisher, Gordon, and Phillips [7])

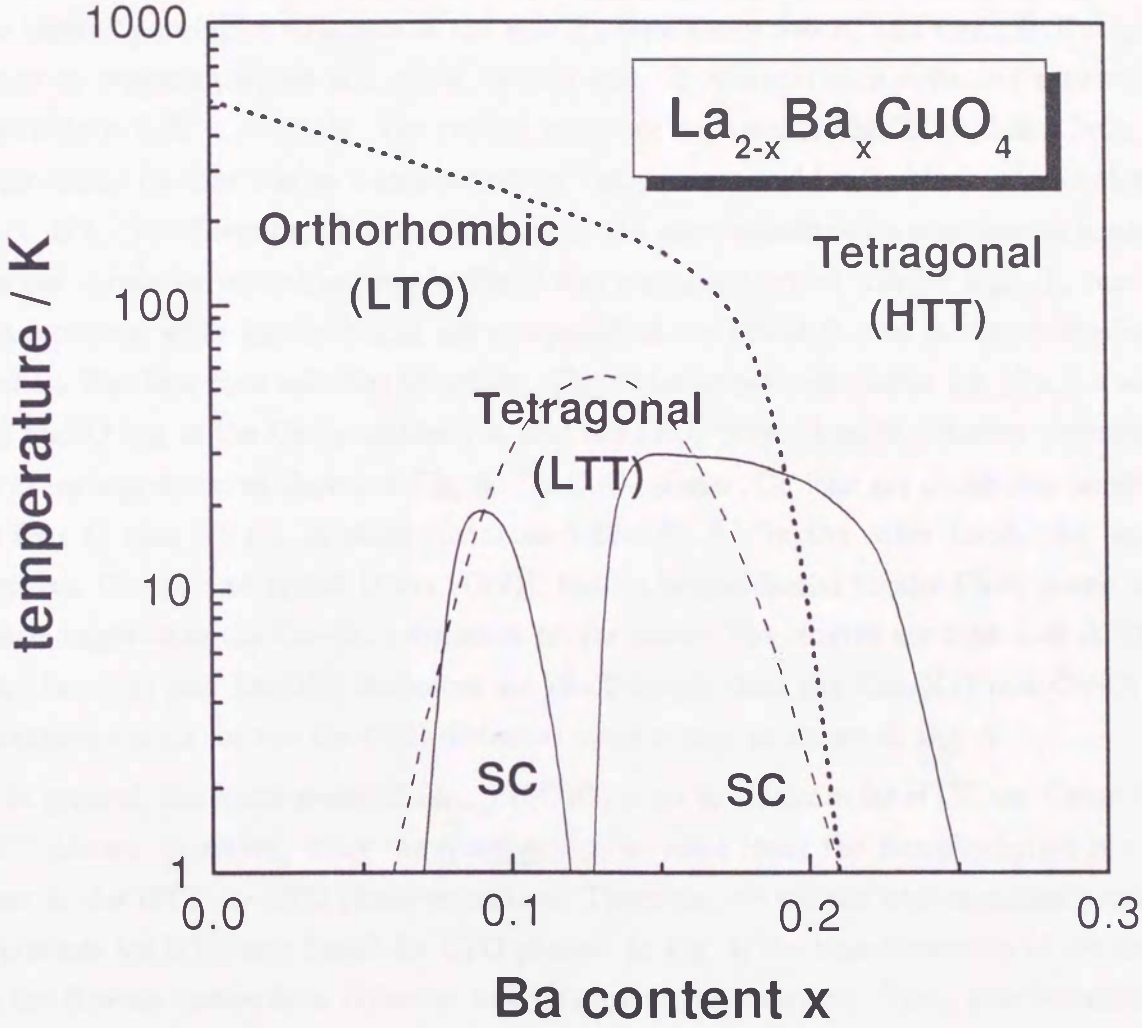

Figure 2: Phase diagram of LBCO. The boundaries of HTT–to–LTO phase transition and of superconducting phase transition are given as same manner as Fig.1. The boundary of LTO–to–LTT phase transition is given in the dashed lines. (after Fisher, Gordon, and Phillips [7])

2 Specimen crystal

2.1 Crystal structure

La_2CuO_4 that is the parent material of $La_{2-x}A_xCuO_4$ compounds (A=Sr, Ba or Ca) have the layered perovskite structure of the K_2NiF_4 type above 540 K, and $La_{2-x}Sr_xCuO_4$ is made by replacing a part of La ions with Sr ions. Sr concentration indicated superconductivity is $0.06 < x < 0.24$. The crystal structure is shown in Fig. 3. $La_{2-x}Sr_xCuO_4$ is constructed by that a layer which consist of CuO_2 planes and La_2O_2 blocks stacks along ($a/2$, $b/2$, $c/2$) direction. The CuO_2 plane in the layer consists of a sequence of square lattices shown by dotted pattern in Fig. 4 and play a important role for high$-T_c$ superconductivity, while La_2O_2 blocks are comprised of the apical O ions in the octahedron and La ions in a rock salt–like structure. The distance between cation ion (Cu, La and Sr) and O ion in the CuO_6 octahedron and the LaO_9 polyhedron is different according as O ion's position as shown in Fig. 5. On CuO_2 planes, Cu ions are covalently bonded to four O ions (O(1)), in short distances 1.88–1.90 Å. On the other hand, the bond between Cu ion and apical O ion (O(2)), that is perpendicular to the CuO_2 plane are much longer than the Cu-O(1) distances on the plane: The lengths are 2.39–2.42 Å [19]. The La–O(1) and La–O(2) distances are much longer than the Cu–O(1) and Cu–O(2) distances except for the Cu–O(2) distances along c–axis as shown in Fig. 5.

In general, the space group of $La_{2-x}Sr_xCuO_4$ is set in I4/mmm for HTT and Cabm for LTO phases. However, using the space group, we must make the transformation of the axes at the HTT–to–LTO phase transition. Therefore, we use the non–standard setting F4/mmm for HTT and Bmab for LTO phases. In Fig. 4, the transformation of the axes in the Bravais lattice from I4/mmm to F4/mmm is demonstrated. The c axis is common for both the phases, while the a and b axes are rotated to the each other by 45° around c. Correspondingly, the diffraction indices are transformed as follows:

$$\begin{pmatrix} \mathrm{h_F} \\ \mathrm{k_F} \\ \mathrm{l_F} \end{pmatrix} = \begin{pmatrix} 1 & 1 & 0 \\ -1 & 1 & 0 \\ 0 & 0 & 1 \end{pmatrix} \begin{pmatrix} \mathrm{h_I} \\ \mathrm{k_I} \\ \mathrm{l_I} \end{pmatrix}, \tag{1}$$

where the subscripts F and I indicate F4/mmm and I4/mmm respectively. Henceforth, the indices and the axes is used.

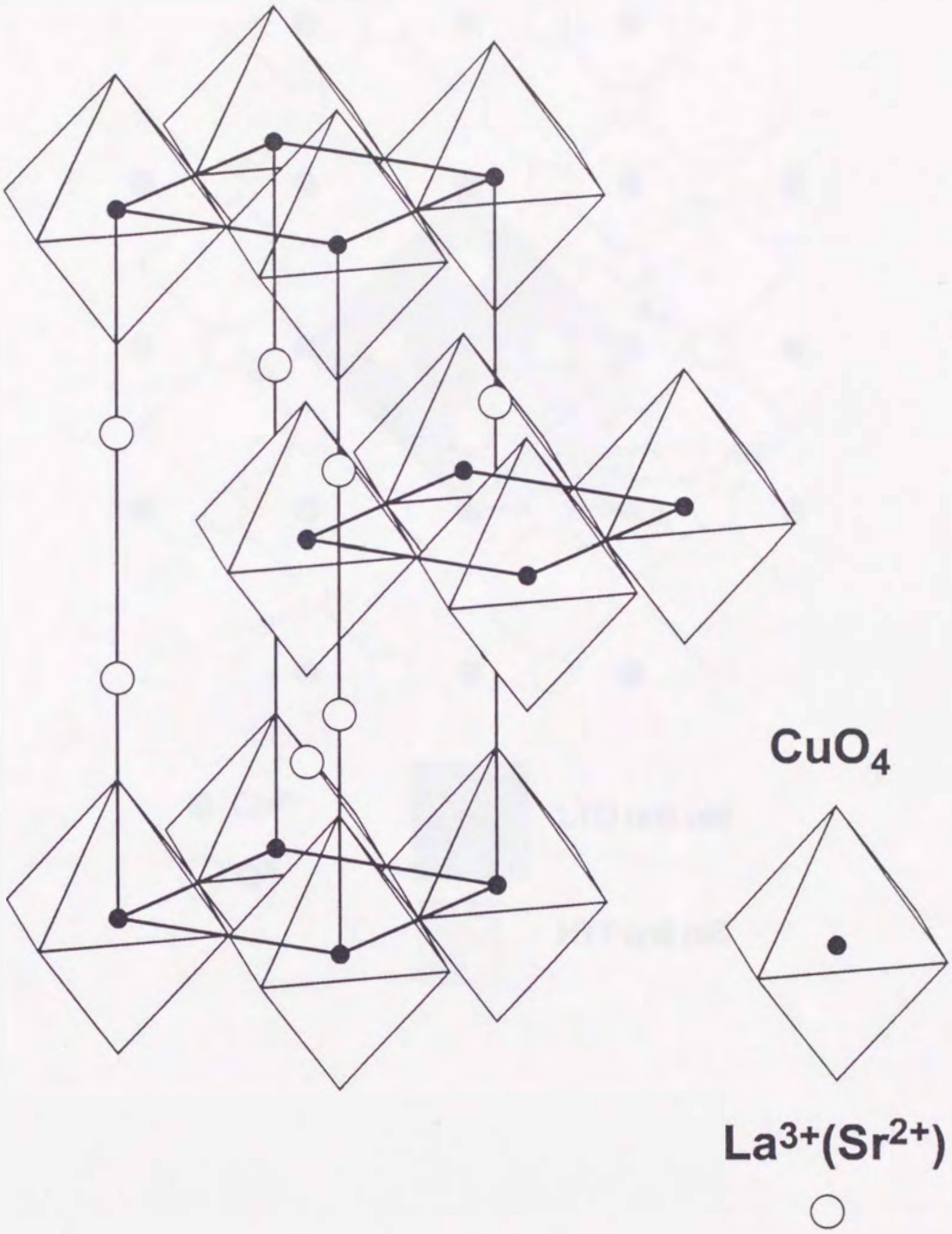

Figure 3: The crystal structure of $La_{2-x}Sr_xCuO_4$ in HTT phase (I4/mmm). Unit cell is indicated by solid lines.

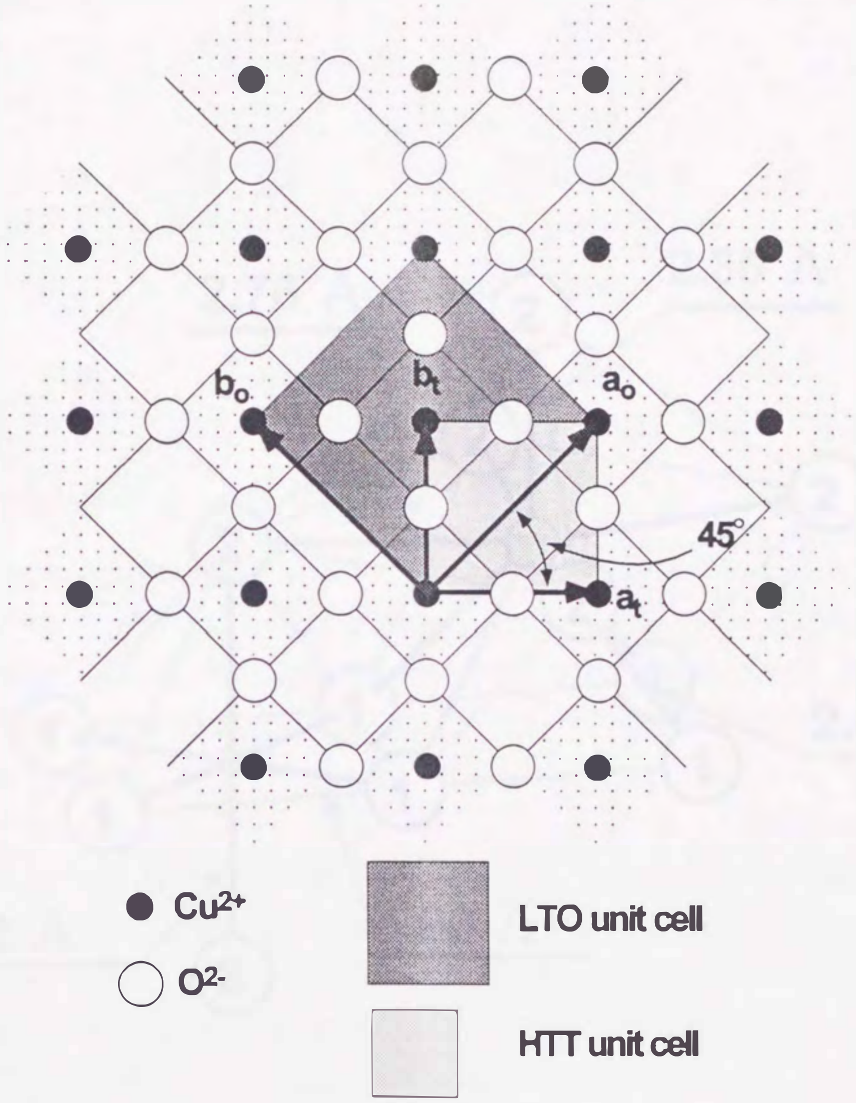

Figure 4: CuO$_2$ plane projected along c: The uint cells for I4/mmm ang F4/mmm are shown by shaded squares.

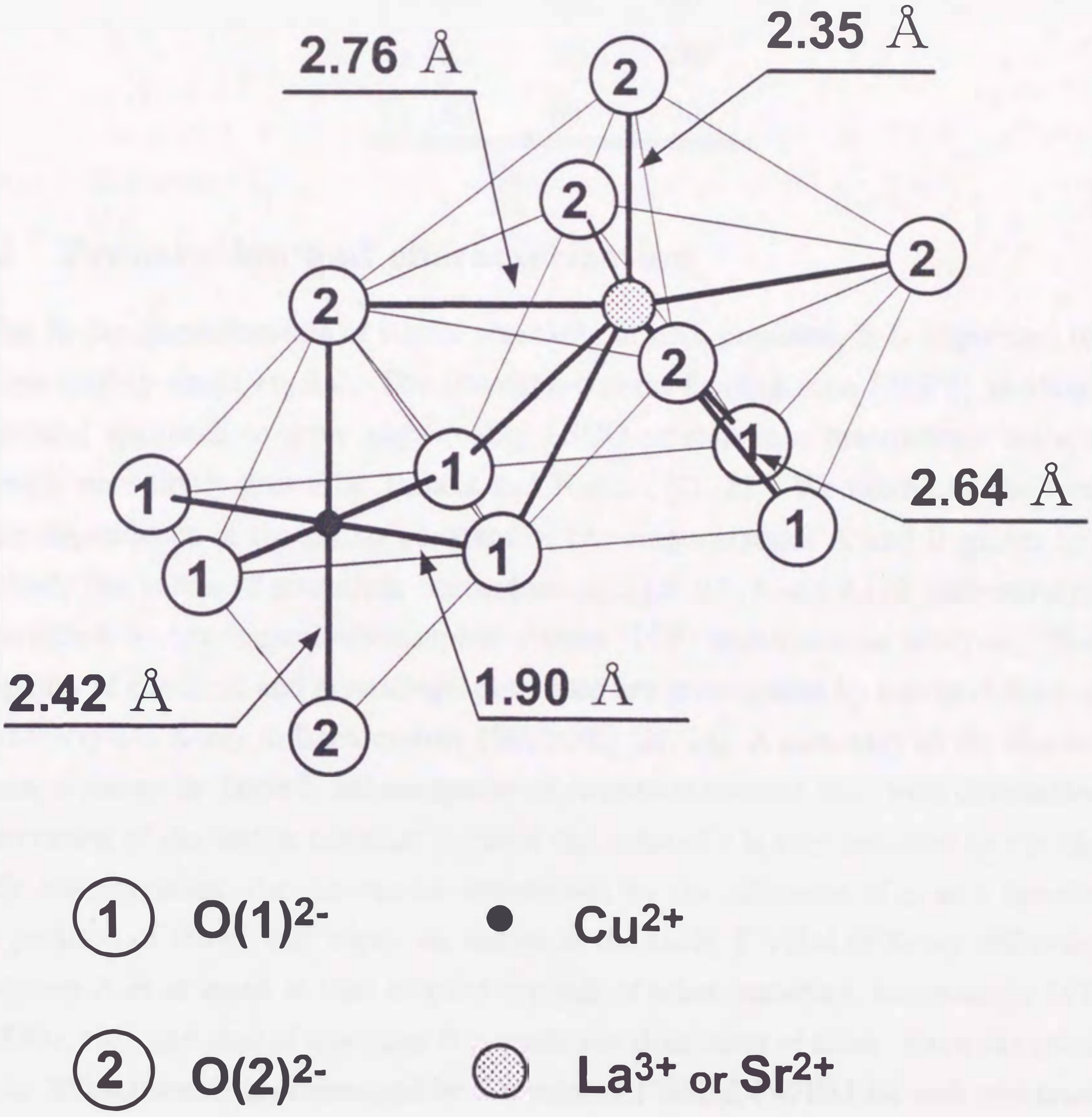

Figure 5: The structure of the CuO_6 octahedron and the LaO_9 polyhedron, and the bonding distance between ions in HTT phase.

Table 2: Chemical and crystallographic characteristics of specimens A ($x = 0.143$) and B ($x = 0.110$).

specimen	A	B
x	0.143	0.110
Δx	0.01	< 0.002
FWHM	200	50
T_S (K)	185	280
T_C (K)	35	30

2.2 Preparation and characterization

For X–ray measurements of lattice constants in high precision, it is important to use a high quality single crystal. The traveling–solvent floating zone (TSFZ) method is a successful approach to grow high–quality LSCO crystals in a macroscopic scale: such crystals were firstly grown by Tanaka and Kojima [21, 22]. We examined the temperature dependence of the lattice constant of two single crystals A and B grown by this method; the values of strontium concentration x are 0.143 and 0.110 respectively, and determined by the inductively–coupled–plasma (ICP) spectroscopic analysis. The homogenity of chemical and crystallographic state are investigated by means of high–angle double–crystal X–ray diffractometery (HADOX) [23, 24]. A summary of the characterization is shown in Table 2. Inhomogenity of strontium content, Δx, were determined by observation of the lattice constant c: Since the value of c is very sensitive to the change in Sr concentration, the Δx can be determined by the difference of c, as a function of the position of the crystal ingot. As shown in the table, FWHM of X–ray diffraction of specimen A is as small as that of good crystals of other materials, for example $SrTiO_3$, $BaTiO_3$, etc., and that of specimen B is much less than those of them. Since the precision of the diffractometer is determined by the value of FWHM, FWHM for each specimen are adequate for measurements in high pricision. Structural phase transition temperature T_s and superconducting phase transition temperature T_c in each specimen that are referred to the literatureare [7] are shown in Table 2. In Figs. 6 (a) and (b), sketches of the shape and size of the specimens are given; the specimen A is cut from as–grown crystal into nearly cube shaped in dimensions about $4.6 \times 2.7 \times 2.0$ mm^3, and two specimens B1 and B2 were prepared respectively for the measurements of the lattice constant c, and a, b

:B1 is cut into pellet form being about 5.3 mm in diameter and 1.0 mm in thick, and B2 is cut into the form as shown in (b). The relation between the shape of the specimens and scattering vectors are described in the figures.

In general, the HTT–to–LTO phase transition cause the appearance of twin strucuture in the LTO phase, and the twin make difficult that determine the strucutural parameter in precision. The twinning mechanism in LSCO is demonstrated in Fig. 7. The twin results in the difference of lattice constants a from b, and specimen has a mirror plane along [1 1 0] socalled a twin boundary. As the result, a reciprocal point in HTT phase splits to two ones in LTO phase. As shown in Fig. 7, an angle ϕ between a^* and b^* axes is expressed by $\phi = 90 - 2\arctan(a/b)$, and ϕ increases with decreasing temperature. In STOE experiments, the split of a reciprocal lattice point can be observed because an adequate space in a reciprocal space is scanned.

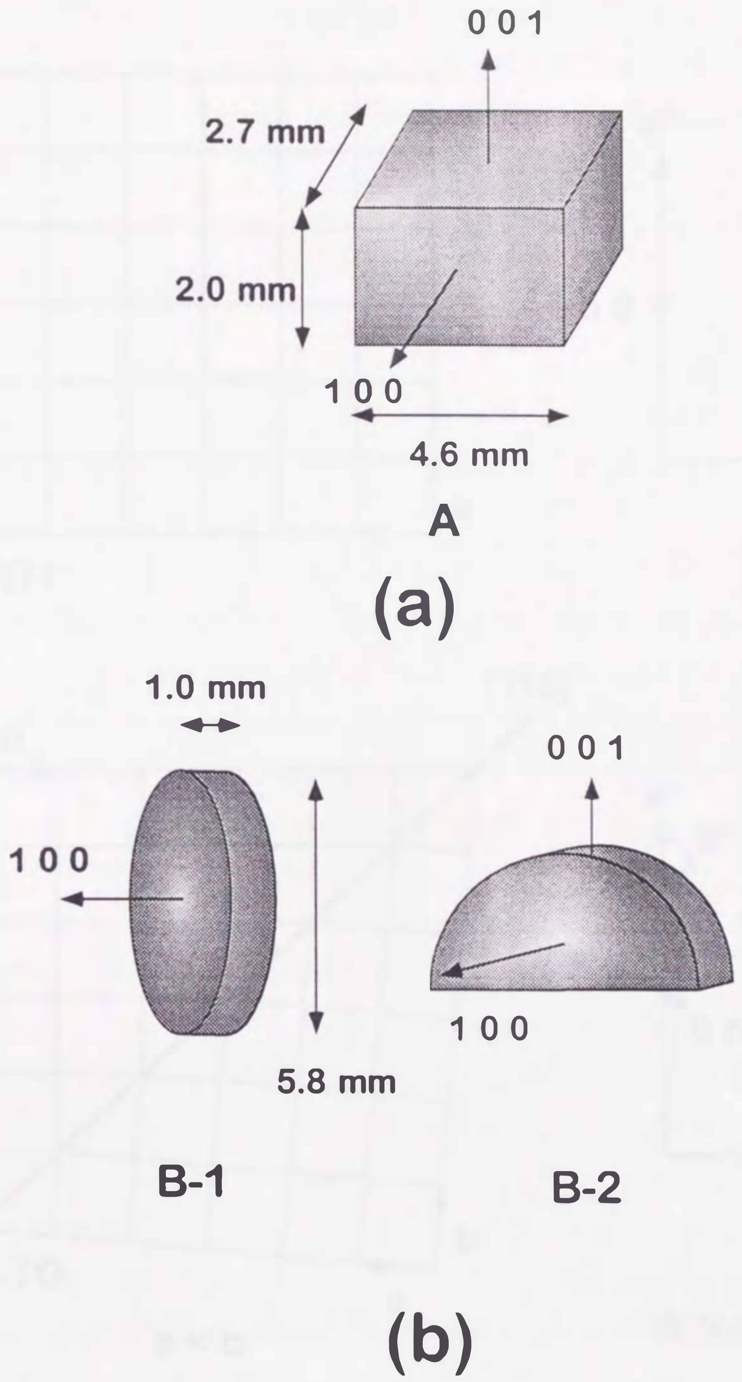

Figure 6: The specimen crystals used in the present experiments. The Sr concentration x of specimens A and B are 0.143 and 0.110 respectively.

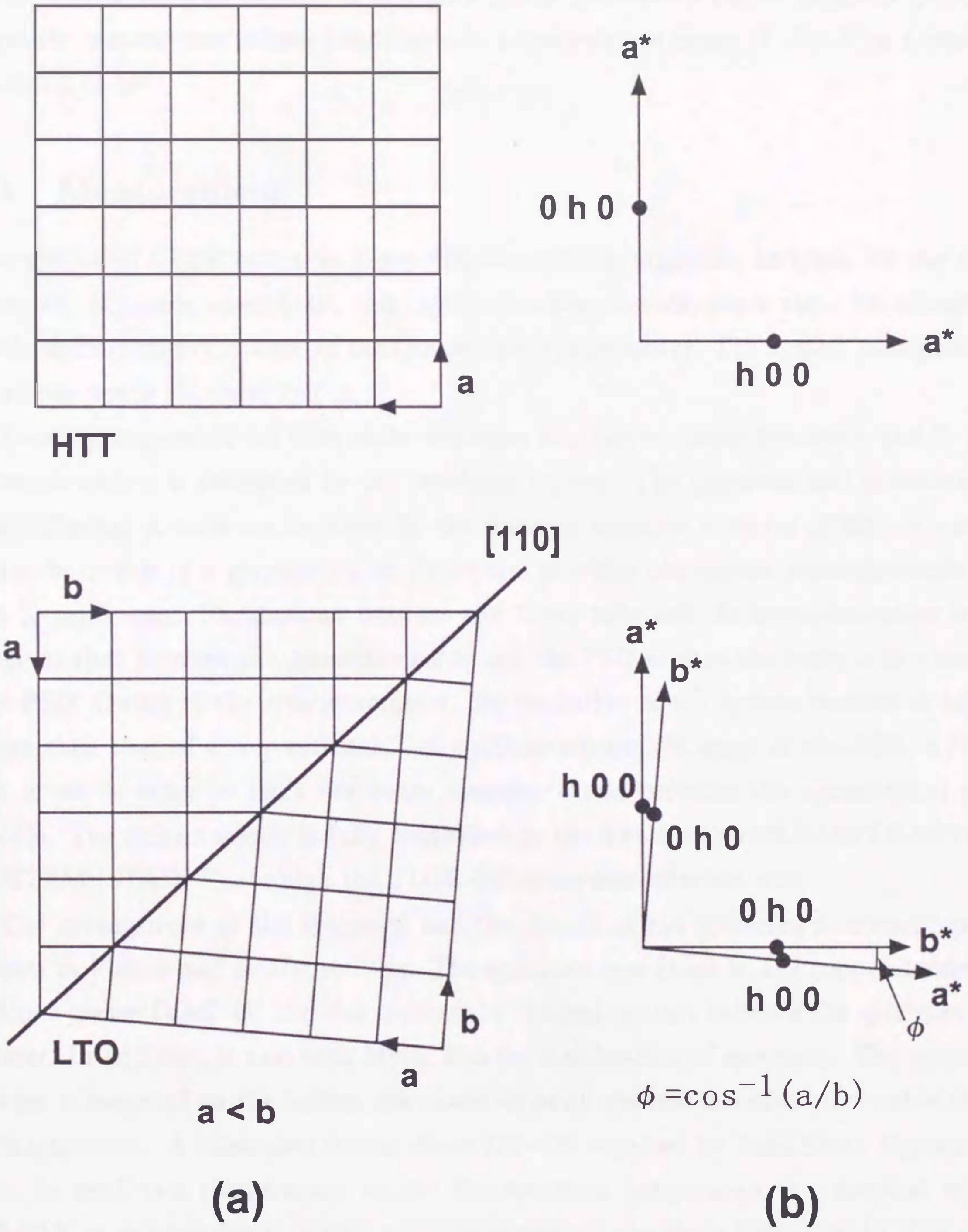

Figure 7: Demonstration of appearance of twin strucure (a) in real space and (b) in reciprocal space. a^* and b^* indicate reciprocal lattice in ab plane.

3 STOE experiments

In order to obtain overall infomation on the temperature dependence of the lattice constants and investigate whether a new LTT phase observed in LBCO exists in low temperature, measurements have been made in a temperature range 17–300 K in a relative precision of 10^{-5}.

3.1 Measurement

The system of STOE two–axis X–ray diffractometer is originally designed for the measurement of powdered crystals, thin layers, seramics, liquids, glass, etc.. An advantage of the diffractometry is a use of the Guinier method geometry. The system configuration is schematically shown in Fig. 8.

X–rays generated X–ray tube make incidence to a curved monochromator, and X–rays monochromized is diffracted by the specimen crystal. The positions and intensities of the diffracted X–rays are detected by the position sensitive detector (PSD). A curved monochromator of a germanium single crystal provides convergent monochromatic Cu Kα X–ray beams. The distance between the X–ray tube and the monochromator is the same as that between the monochromator and the PSD so that the beam is forcused at the PSD. Owing to the monochrometer, the resolution of the system reaches in higher order than that of a conventional X–ray diffractometer. In front of the PSD, a Soller slit is set in order to limit the beam divergence and provides the symmetrical peak profile. The diffractometer is fully controlled by the STOE POWDER DIFFRACTION SYSTEM (STADI P) through the STOE diffractometer interface unit.

The arrangement of the specimen and the deatail of the specimen surroundings are shown in Figs. 9 and 10 respectively. The specimen was glued to the copper–holder by silicone grease(IVAC–G) and this insures the thermal contact between the specimen and holder. In addition, it tied with Mylar film for stabilization of specimen. The specimen holder is mounted on the helium gas closed–type of cryostat installed on ω–table of the diffractometer. A calibrated silicon diode DT–470 supplied by Lake Shore Cryotronics Inc. is used as a temperature sensor; the specimen temperature is controlled within ±0.02 K at any temperature with a PID–controller (Lake Shore DRC–93CA). The cover made by copper is set at the top of the cold finger for shielding specimen from external thermal radiation.

The relations between the indices and the lattice constans for specimen A and B are

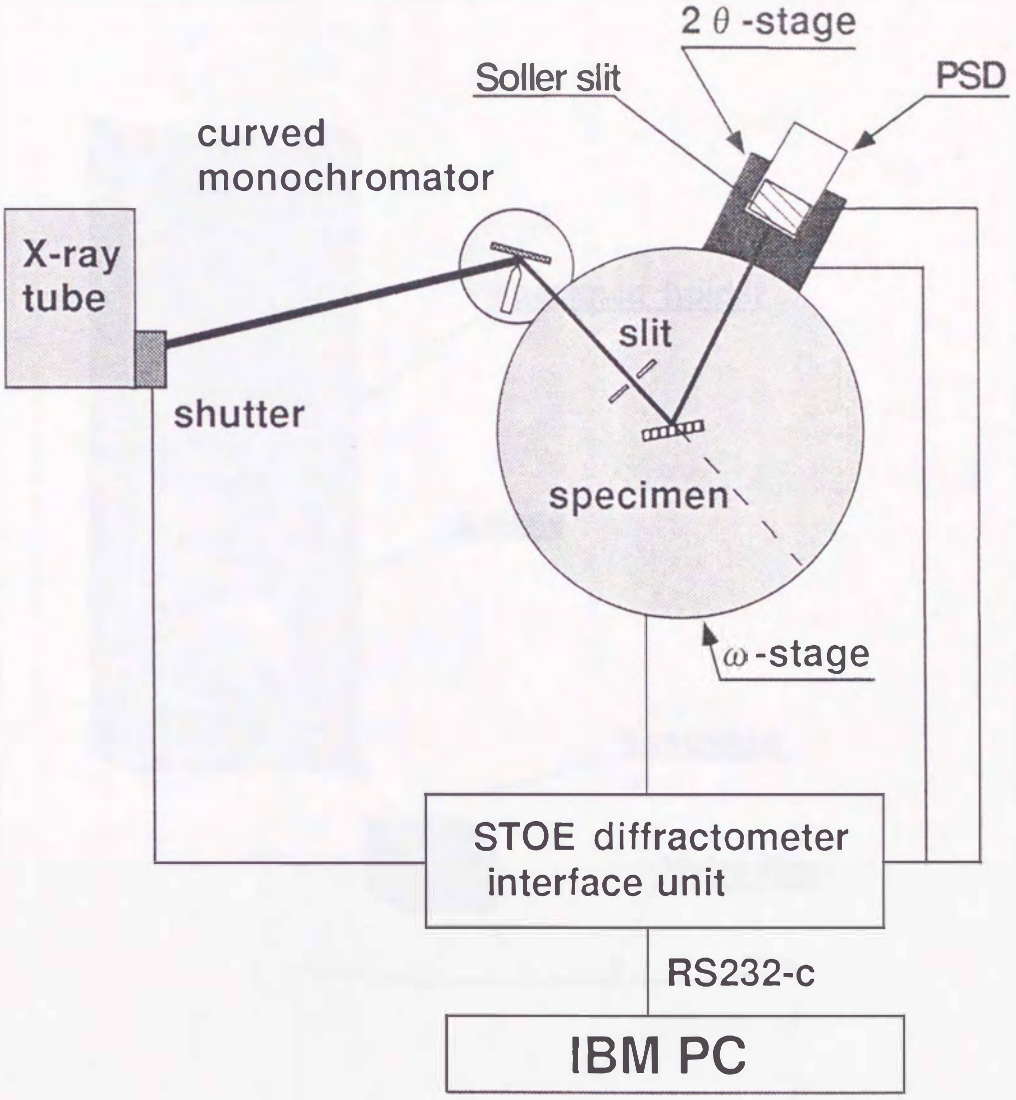

Figure 8. The configuration of the STOE diffractometer and the control system.

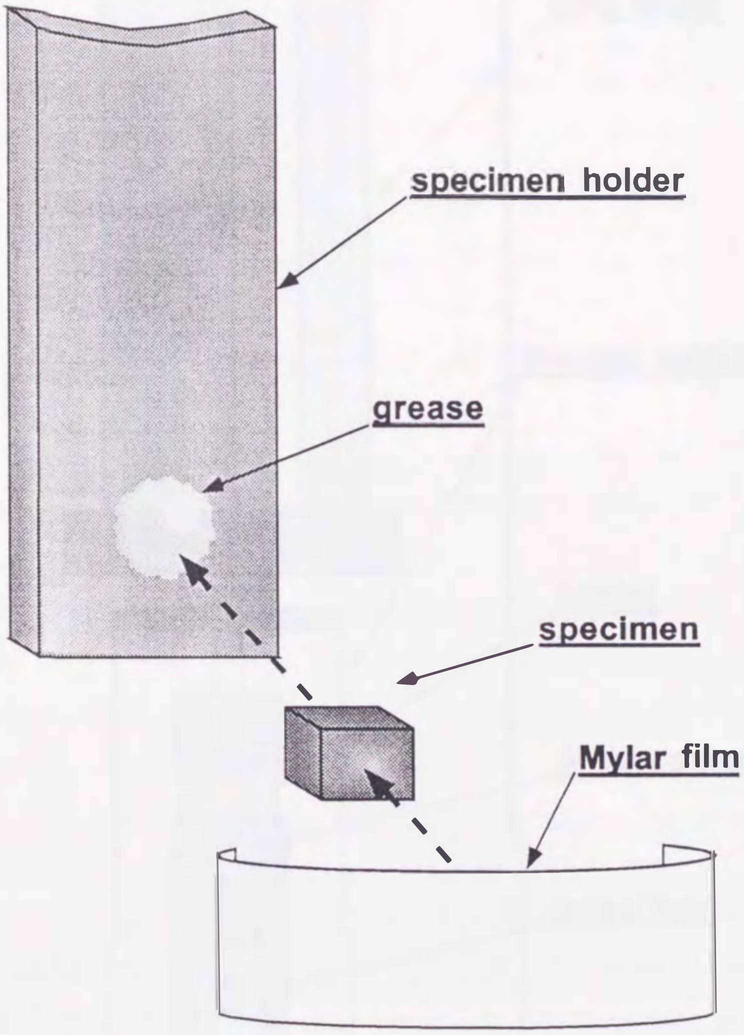

Figure 9. The arrangement of specimen to the specimen holder.

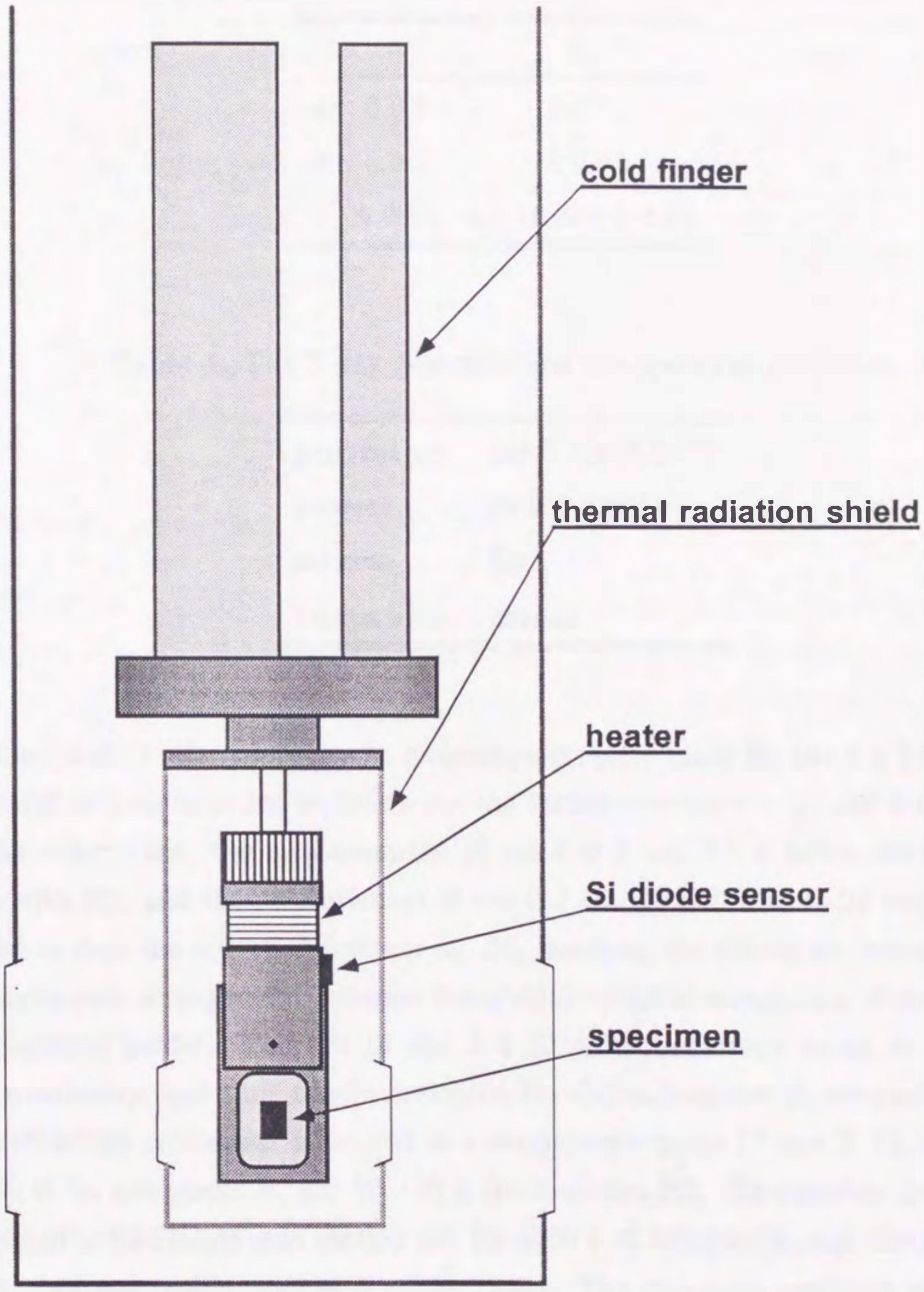

Figure 10. The specimen holder and the surroundings.

Table 3: The relations between the indices and the lattice constants for specimen A and B.

	A	B
a	6 0 0	6 0 0
b	0 6 0	0 6 0
c	0 0 14	4 0 10 and 0 4 10

Table 4. The X–ray generator and the operating condition.

generator:	MAC M03XHF^{2}2
power:	60 kV 30mA
target:	Cu
forcus size:	normal

listed in Table 3. For specimen A, measurements were made for the 0 0 14, 6 0 0 and 0 6 0 diffractions in order to determine the lattice constants c, a, and b respectively. On the other hand, the measurements of the 6 0 0 and 0 6 0 diffractions have been made with B1, and the measurement of the 2 2 10 diffraction with B2 respectively; it is tried to find the 0 0 14 diffraction for B2, however, the diffraction cannot be found for inadequate arrangement between the crystallographic orientation of specimen and the specimen holder. The 4 0 10 and 0 4 10 diffractions were found in a relatively strong intensity, and thus finally measured the diffractions for th determination of c. The diffraction profile was measured in a temperature range 17–300 K for specimen A, 18–300 K for specimens B, and 20–120 K for specimen B2. The intensity integration in a mode of ω oscillation was carried out for 1000 s of integration, and the peak height of the observed profile reached 2×10^4 counts. The operating condition of the X–ray generator is summarized in Table 4.

For the 0 0 14 diffraction of specimen A, and for the 6 0 0 and 0 6 0 diffractions of specimen B1, measurements on both cooling and heating were made; the reproduction of the temperature dependence of the lattice constants was thus confirmed. Therefore, we made measurements for only heating processes for the other diffraction.

Table 5. The analytical method and parameters to be refined.

Sr concentration x	0.110		0.143	
Diffraction indices	6 0 0 0 6 0	4 0 10 0 4 10	6 0 0 0 6 0	0 0 14
Algorithm for NLSM	Marquardt			
Profile function	Split Pearson7	Pseudo-Voigt		
Peak number ($T > T_s$)	2	—	1	2
($T < T_s$)	4	2	2	2
Refiment parameters	X_0, Y_0, H	X_0, Y_0, H, n		

3.2 Data analysis and results

The PEAK and FIT programs in the Visual X^{pow} software pakage supplied for STOE Inc. was used for the data analysis. The PEAK program is for searching the peak in the raw data, and then determines the position of the peak maximum that is used for the initial parameters of the FIT. The FIT program is for fitting a profile function to the observed peak profile and for decomposing the peak profile. Parameters of the profile function are optimized by the non–linear least squares method (NLSM). The infomation of the fitting is shown in Table 5.

The Pseudo–Voigt function was used as the fitting function, but, for the 6 0 0 and 0 6 0 diffractions in specimen B, the Split Pearson 7(SP7) was used. Because the peak profile of this diffraction is remarkably asymmetric. Owing to the strong correlation among the parameters for the SP7 function, exponents m_l、m_r and halfwidth ratio H_l/H_r were fixed in the values determined at the room temperature.

In Fig. 11, examples of the observed diffraction profile of specimen A are shown: (a) for the 0 0 14 diffraction at 16 K, and (b) for the 6 0 0 and 0 6 0 diffractions at 27 K. The 0 0 14 diffraction consist of the components of Cu Kα_1 and Kα_2. On the other hand, in the case of the 6 0 0 and 0 6 0 diffractions, the profile consists of a single peak because of the elimination of the Kα_2 component by a careful adjustment of the Ge monochromator and slits. The completely separated two peaks are assigned to the 6 0 0 and 0 6 0 diffractions:i.e. the peaks positions correspond to the lattice constants a and b in the LTO phase. The seperation of the peaks increases with decreasing temperature;

Split Pearson 7:

$$Y = Y_0 \cdot \left[1 + C_{PSl} \cdot \left(\frac{X - X_0}{H_l}\right)^2\right]^{-m_l} \qquad (X < X_0)$$

$$Y = Y_0 \cdot \left[1 + C_{PSr} \cdot \left(\frac{X - X_0}{H_r}\right)^2\right]^{-m_r} \qquad (X > X_0)$$

Pesudo-Voigt:

$$Y = Y_0 \cdot (1 - n) \cdot \left[1 + C_{LI}\left(\frac{X - X_0}{H}\right)^2\right]^{-1} + Y_0 \cdot n \cdot exp\left[-C_{GS}\left(\frac{X - X_0}{H}\right)^2\right]$$

X_0: Peak position
Y_0: Maximum counting rate (at X_0)
H: Full width at half maximum(FWHM)
n: Gauss component of Pseudo–Voigt profile
H_l/H_r: Halfwidth ratio for Split Pearson 7 profiles
H_l+H_r: Overall halfwidth for Split Pearson 7 profiles

this indicates the increments of lattice distortion b/a.

In Figs. 12 (a) and (b), examples of the observed profiles of specimen B are shown for the 4 0 10 and 0 4 10 diffractions at 24 K, and for the 6 0 0 and 0 6 0 diffractions at 18 K respectively. Two peaks are due to structural phase transition like as the case of Fig. 11 (b). The 6 0 0 and 0 6 0 diffractions contain minor subpeak due to Kα_2 component. In the fitting process, we consider that each diffraction includes one or two peaks as shown in Table 5. The results of the fitting are also shown in Figs. 11 and Figures 12 in a solid line, and, below the line, the differences of the fitting results from the raw data are also indicated. It found that the fitting results indicate a good agreement with the data and a residuary component is not almost included. This means that a new phase like LTT phase doesn't appears in low temperature.

From the determined 2θ angle position to Cu Kα_1 component, the lattice constants were obtained by obeying equations (2).

$$2d_{hkl}\sin\theta = \lambda, \tag{2}$$

and

$$d_{hkl} = 1/\left(\frac{h^2}{a^2} + \frac{k^2}{b^2} + \frac{l^2}{c^2}\right)^{1/2}, \qquad (3)$$

where λ is the wavelength of Cu Kα_1 (1.54051 Å). Since the lattice spacing with Miller indices h k l in orthorhombic phase is expressed by equation (3), lattice constants a, b and c are determined by 2θ positions of the 6 0 0, 0 6 0 and 0 0 14 diffractions, respectively. The lattice constant c of the specimen B2 is obtained from the 2θ position of the 4 0 10 diffractions using the determined value of the 6 0 0 diffractions in specimen B1.

The peak profiles of each diffraction are shown as function of temperature in Figs. 13, 14 and 15 respectively. In Fig. 13, the form of the profile for the 0 0 14 diffraction in specimen A is almost same form from room to low temperature, and the peak position moves to high angle with decreasing temperature. On the other hand, in Fig. 14, that for the 6 0 0 diffraction in specimen A splits into two peaks 6 0 0 and 0 6 0 below 180 K, and the distance between two peaks increases monotonously with decreasing temperature. In specimen B, the temperature dependence of a peak profile for the 6 0 0 diffraction is in qualitative agreement with that in specimen A, but, for a peak profile above 200 K, it is very difficult to decompose the profile into two peaks because the peak profile include a peak of Cu Kα_2. The temperature dependence of the peak profiles is consistent with that of the lattice constants. Furthermore, the emergence of a new peak cannot be observed in all temperature dependence of profiles, and therefore, it is concluded that the appearance of a new phase like LTT phase is not observed in this measurements.

The temperature dependence of the lattice constant c, of those a and b, and of the unit-cell volume of sepcimen A are shown in Figs. 16, 17 and 18 respectively. Temperature of the HTT–to–LTO phase transition and that of superconducting phase transition are indicated by respectively the broken and the dotted lines in the figures. The lattice constants linearly decrease with decreasing temperature in HTT phase and the effect of the HTT–to–LTO structural phase transition is clearly observed in all lattice constants. For the lattice constant c, additional contraction of the lattice is observed below T_s. On the other hand, the temperature dependence of in–plane lattice constant, i.e. a of HTT phase, splits into orthorhombic a– and b–axis below T_s, and then the split is monotonously increasing with decreasing temperature. The orhorhombic distortion b/a is 1.0045 at 27 K, and this is consistent with the value given in literature [25]. In Fig. 17, the mean constant $(a+b)/2$ of the in–plane lattice constant a and b is also given for the comparison with thermal expansivity by the capacitance dilatometer [4]; i.e., specimen using the measurement have twin structure, and therefore, the result is an average value

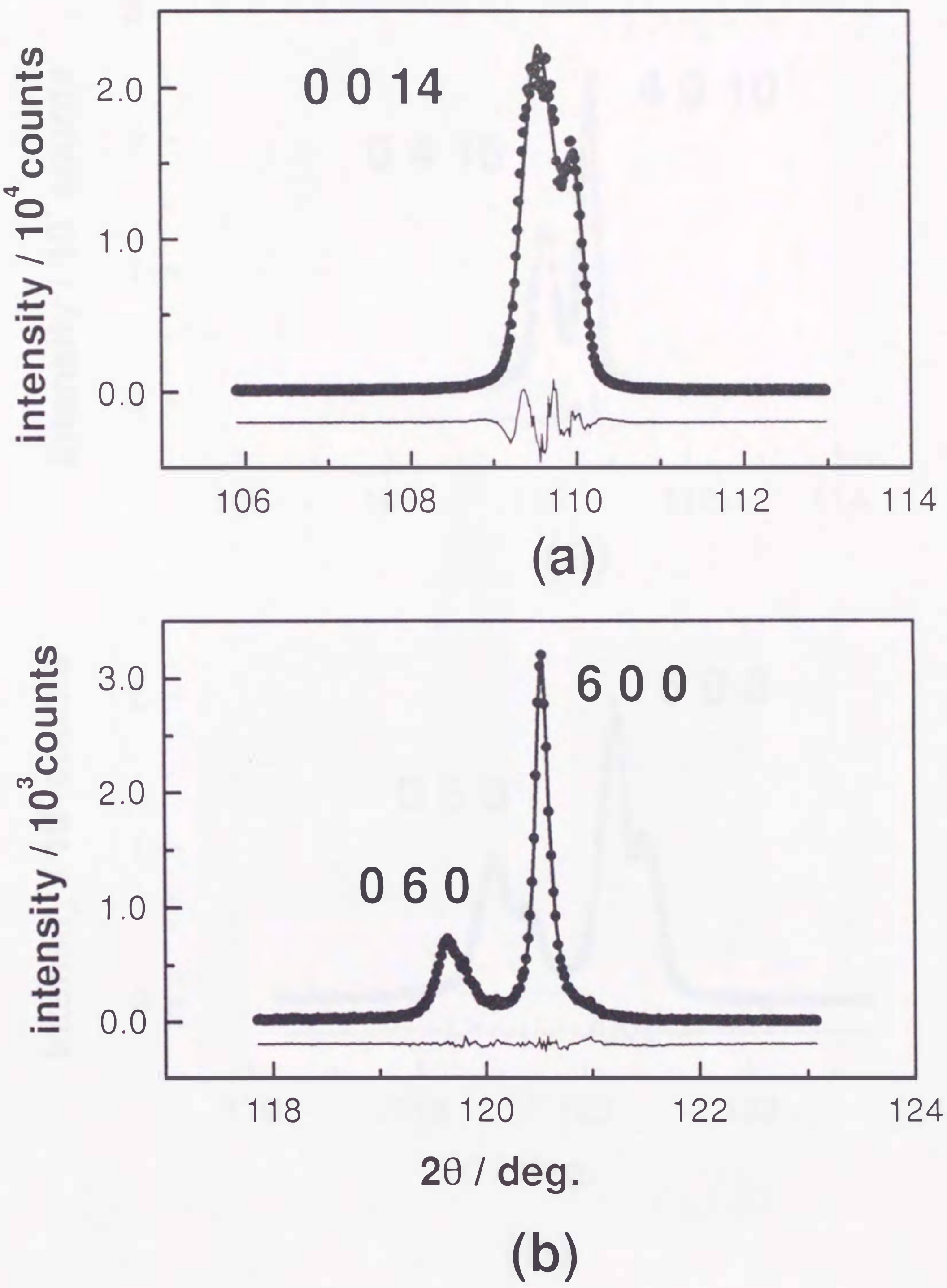

Figure 11: Examples of the observed peak profile of specimen A: (a) for the 0 0 14 diffraction at 16 K, and (b) for the 6 0 0 and 0 6 0 diffrations at 27 K. The curve is the least–squares fit of the profile function to the experiment.

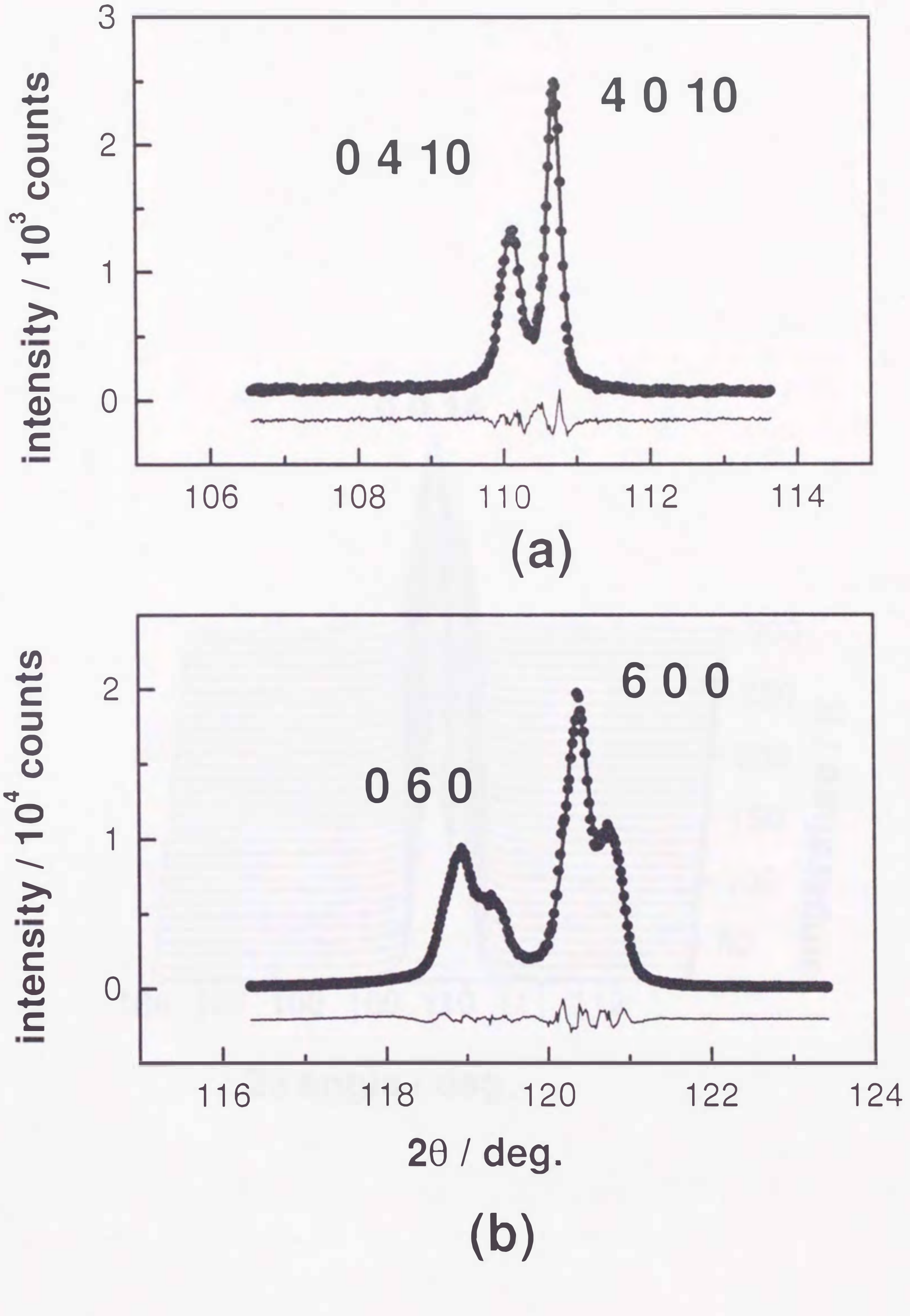

Figure 12: Examples of the observed peak profile of specimen B: (a) for the 4 0 10 and 0 4 10 diffractions at 24 K, and (b) for the 6 0 0 and 0 6 0 diffrations at 18 K. The curve as in Fig.7.

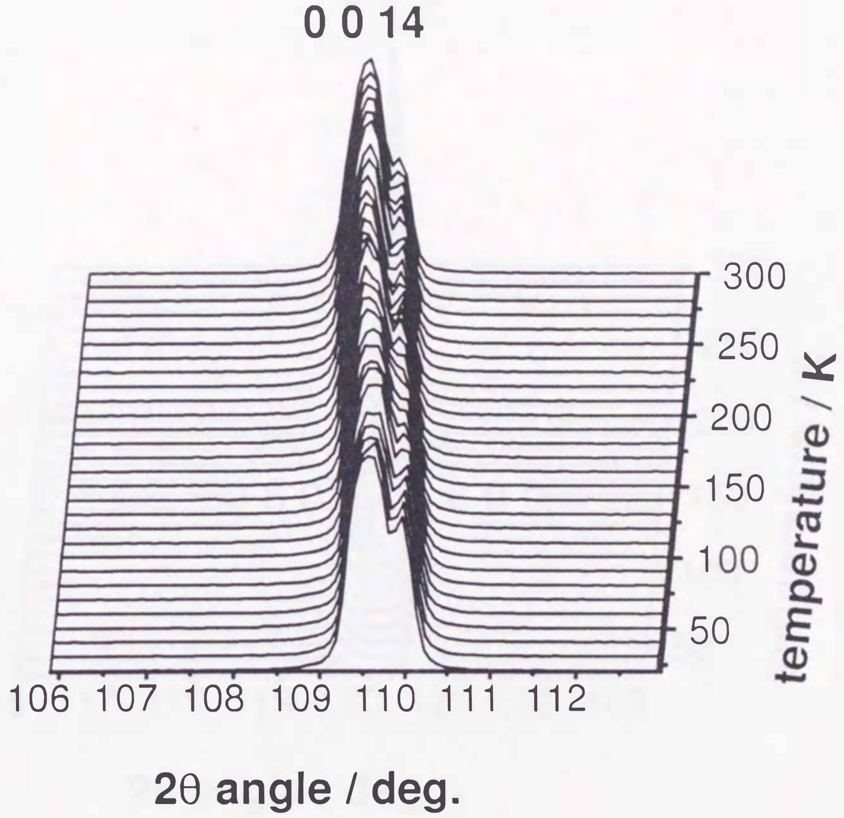

Figure 13: Peak profiles of the 0 0 14 diffraction in specimen A as function of temperature.

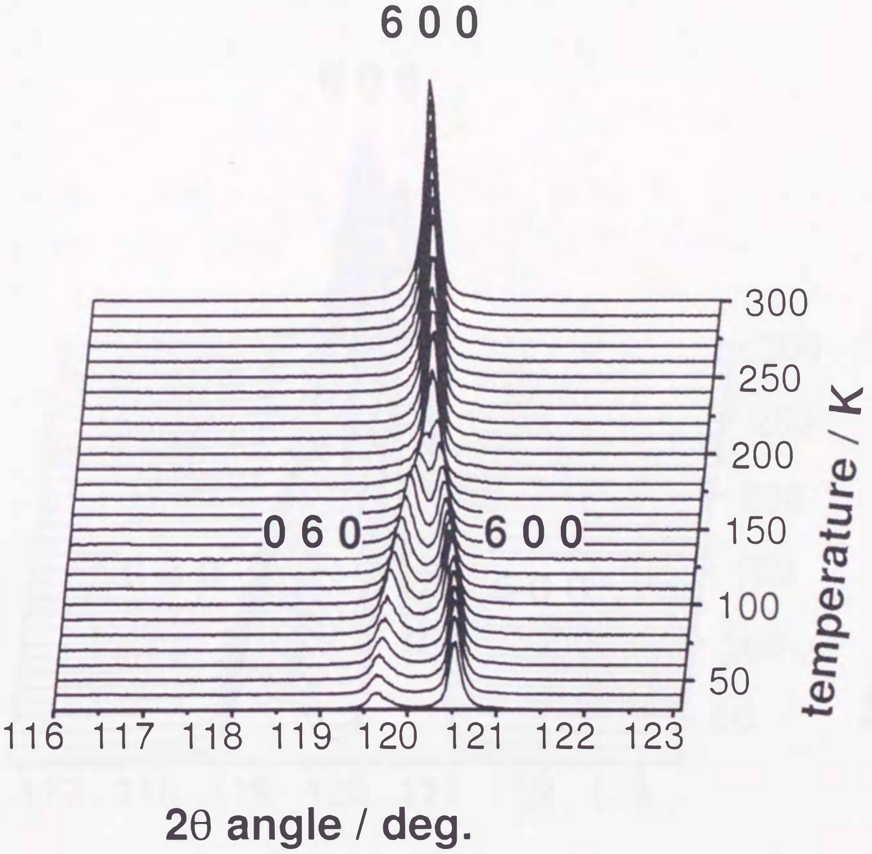

Figure 14: Peak profiles of the 6 0 0 diffraction in specimen A as function of temperature.

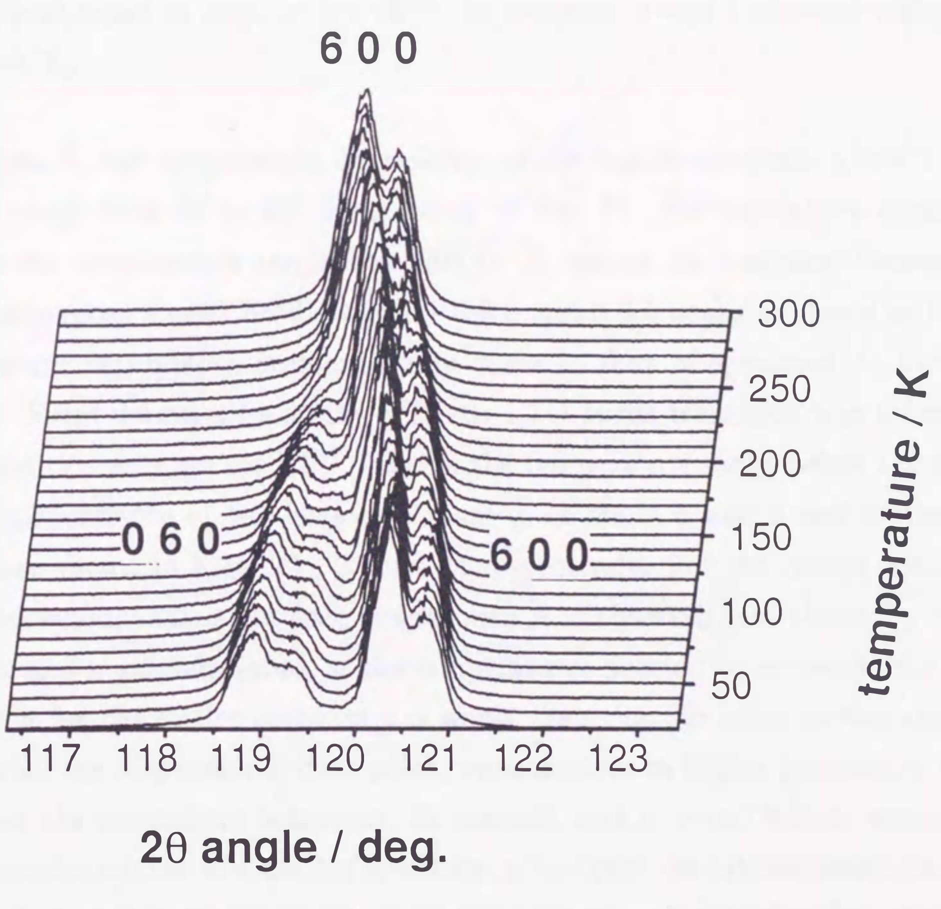

Figure 15: Peak profiles of the 6 0 0 diffraction in specimen B as function of temperature.

of in–plane. The thermal expansivity abruptly decreases from 10 to 2 $\times 10^6$ at T_s and keep constant to low temperature. The result is qualitatively consistent with the present result of $(a+b)/2$. The temperature dependence of the cell volume calculated lattice constants a, b and c are given in Fig. 18. The volume shows a subtle change of the temperature dependence at T_s. This results in cancellation of slope change in c and $(a+b)/2$ below T_s. In order to clarify the effect of superconducting phase transition on the lattice constants, the lattice constants around T_c are shown in Figs. 19 and 20 in an expanded scale. The lattice constant c reachs to the minimum at T_c and then seems to increase with decreasing temperature. This behaviour was consistent with the result of Maeta *et al.* [17]: the relative change $\Delta c/c$ between 20 and 33 K was reported as 1×10^{-5}, while the present result is $\Delta c/c = 3 \times 10^{-5}$. In contrast, a and b show no remarkable change around T_c.

For specimen B, the temperature dependence of the lattice constants a and b in the temperature range from 18 to 300 K is shown in Fig. 21. For the lattice constant b, the result in the temperature range from 200 to T_s cannot be indicated because it is difficult to decompose a peak profile into the 6 0 0 and 0 6 0 peaks as shown in Fig. 15. The temperature dependence is qualitatively same as that of specimen A, but T_s is much higher. Since information on the HTT–to–LTO phase transition was obtained in detail, the results are shown for LTO phase in the temperature range below 120 K. The temperature dependence of the lattice constant c, of those a and b and of the unit–cell volume are shown in Figs. 22 , 23 and 24 respectively. For the lattice constant c, anomalous behaviour that is not seen in specimen A is observed just above T_c; it takes the minimum and maximum values at the temperatures pointed by arrows in the figure. Since precision for the lattice constant c is worse than that for other lattice constants as be clear from the dispersion of data point, measurement in higher precision is needed for being clear the anomalous behaviour. In contrast with c, a and b show temperature dependence similar to that of a and b of specimen A; however, the orthorhombic distortion b/a is larger than that in specimen A because T_s in specimen B is higher than that of the specimen A. The value of b/a of specimen B is 1.0075 at 18 K, being in agreement with the value 1.0072 given by Radaelli *et al.* [25]. Furthermore, the temperature dependence of the unit–cell volume has been calculated; as shown in Fig. 24, a plateau is observed in the range 40 – 60 K. As mentioned above, the lattice constant c takes the minimum and maximum values, and therefore, this results in the plateau. It should be noted that the only lattice constant b shows continuous increase even at low temperatures both for

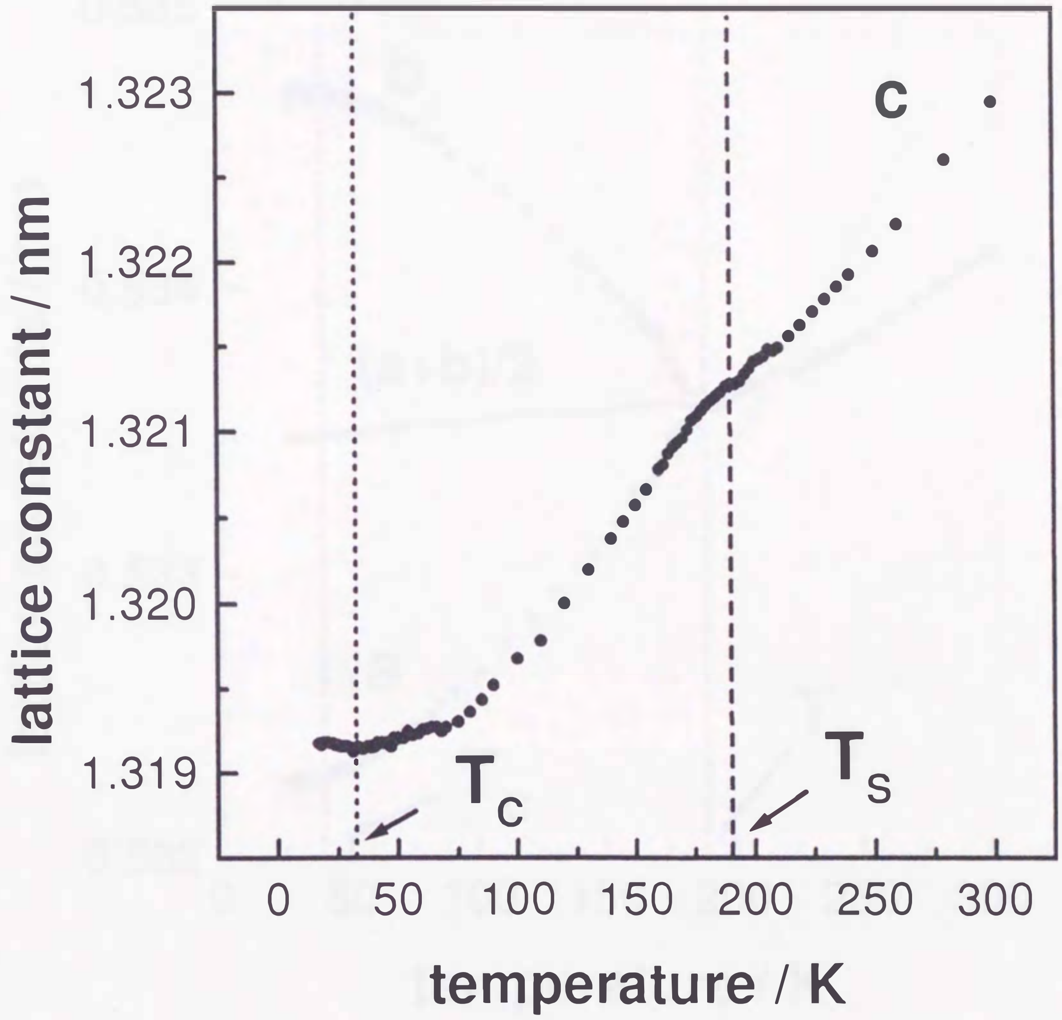

Figure 16: The temperature dependence of the lattice constant c for specimen A; T_s and T_c are the temperature of the HTT–to–LTO phase transition, and that of the superconducting transition, respectively.

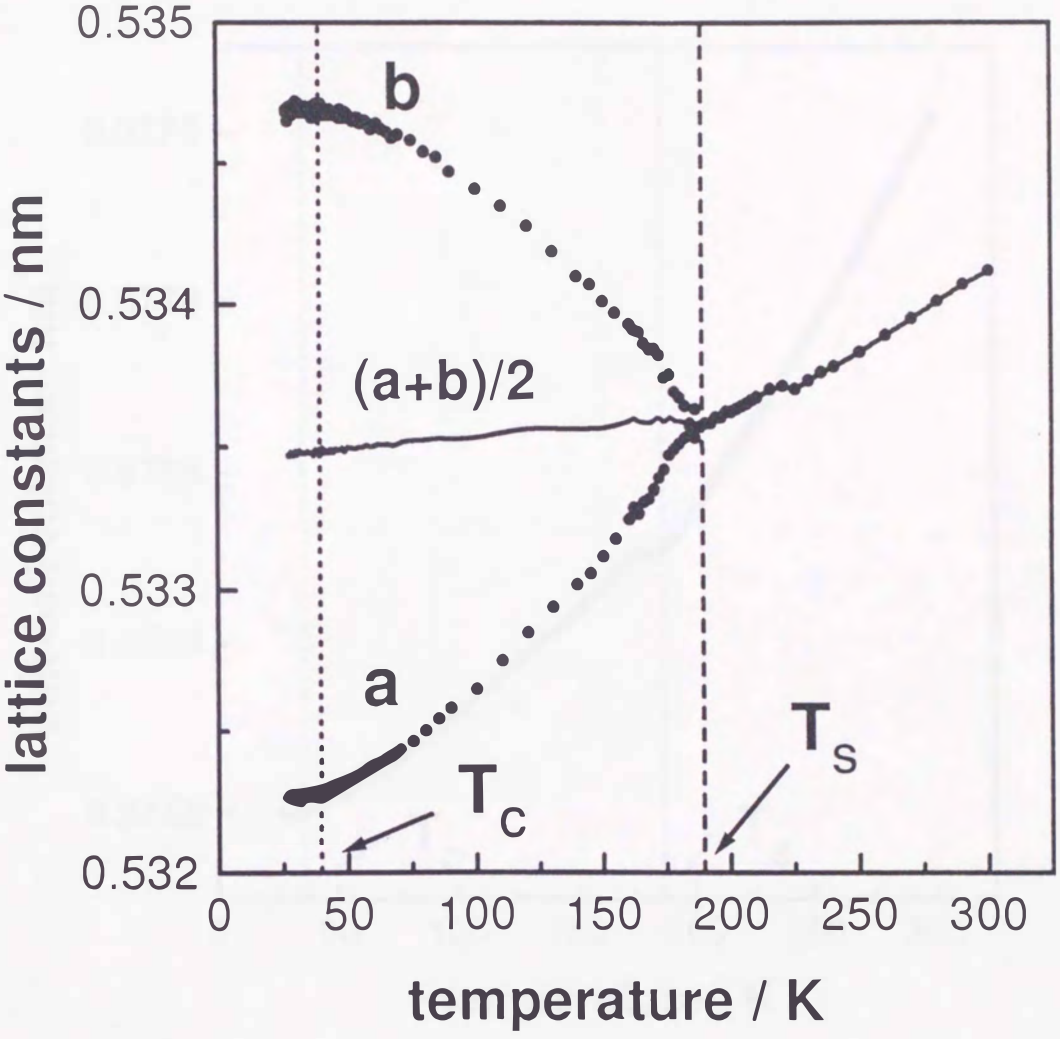

Figure 17: The temperature dependence of the lattice constants a and b of specimen A; T_s and T_c as in Fig. 9. The curve below T_s is the mean value of a and b:i.e. $(a+b)/2$.

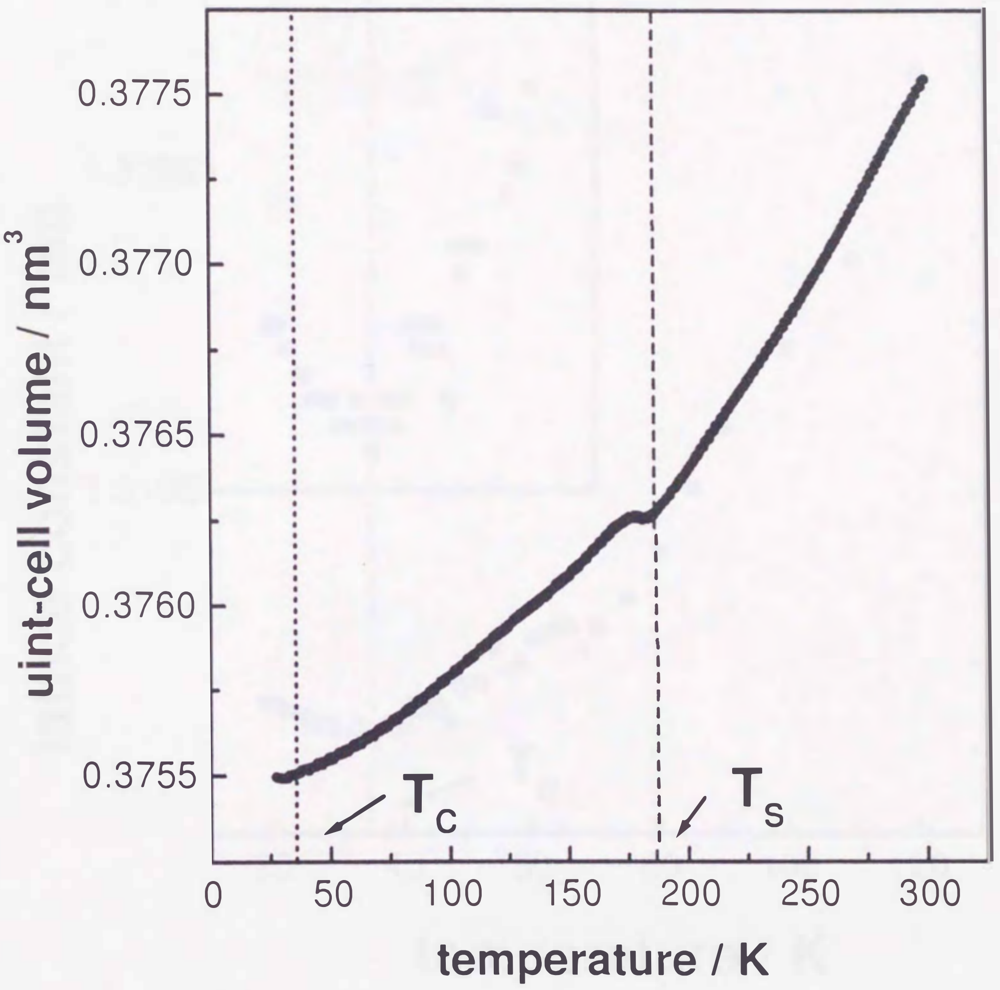

Figure 18. The unit–cell volume of specimen A as a function of temperature.

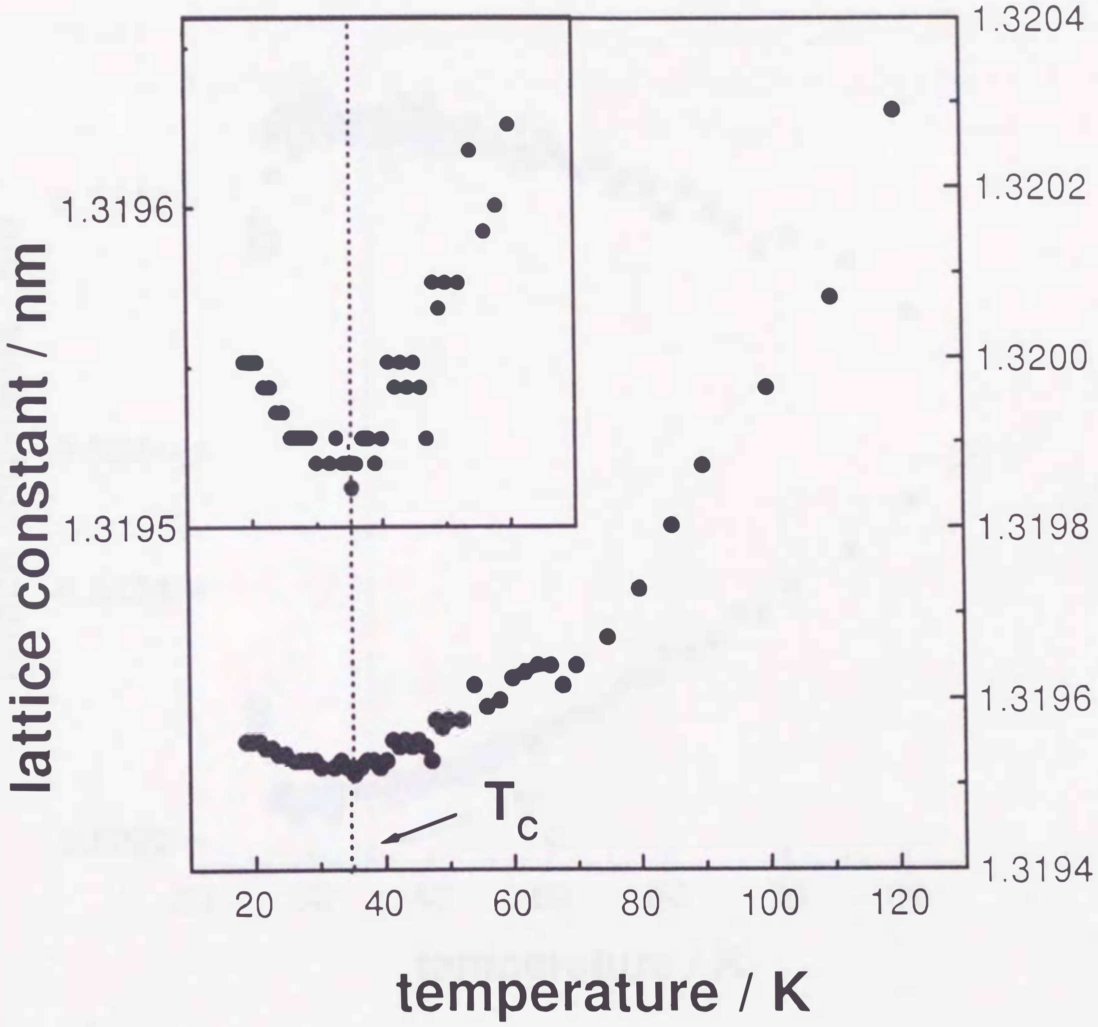

Figure 19: The lattice constant c of specimen A in an expanded scale at low temperatures. In the inset, the ordinate is further expanded by a factor of four.

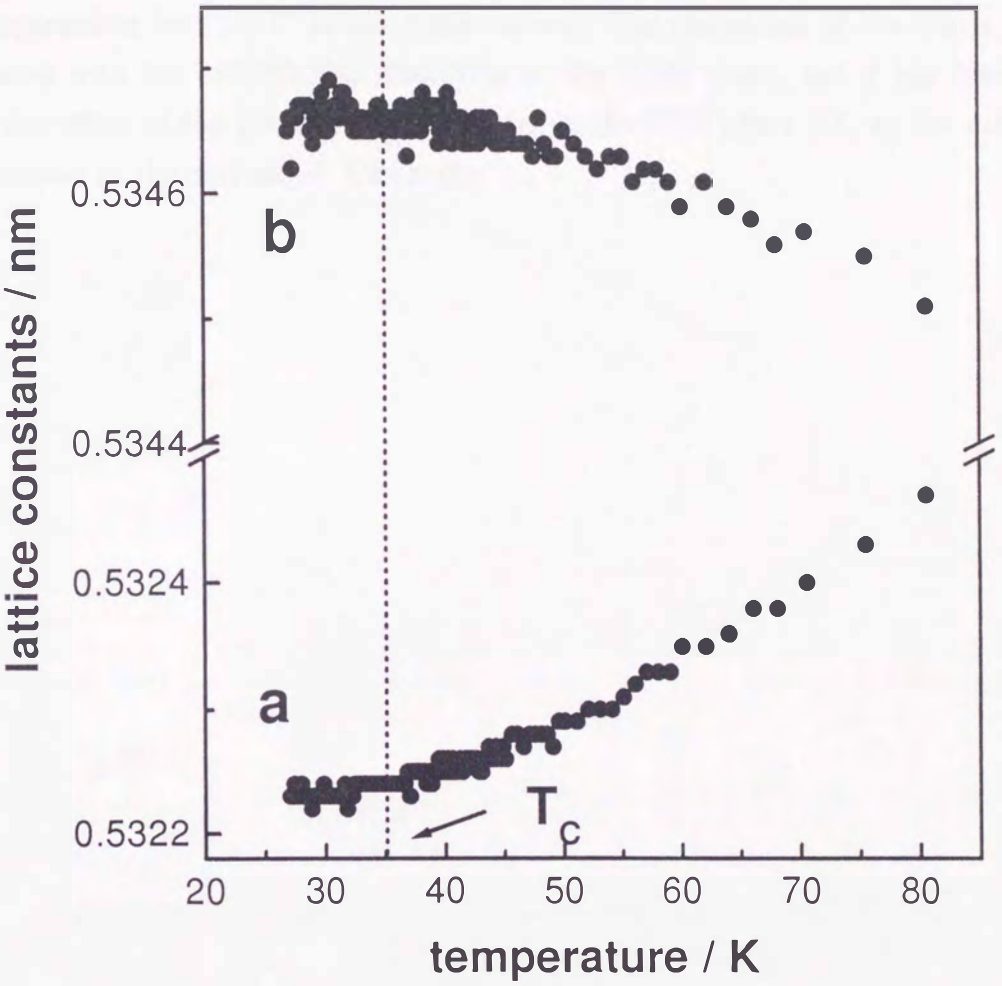

Figure 20: The lattice constants a and b of specimen A in an expanded scale low temperatures.

specimens A and B in contrast with the result for $YBa_2Cu_3O_{6+\delta}$(YBCO); i.e., YBCO has the HTT–to–LTO phase transition similar to LSCO, but all lattice constants decrease with decreasing temperature. In general, thermal expansion is caused by anharmonic term of the interatomic potential. It is well known that the lattice constants and the unit–cell volume decrease with decreasing temperature, in proportion to T at the high temperatures, and to T^4 at low temperatures. The elongation of the b axis is therefore related with the orthrohmbic distortion in the CuO_2 plane, and it has been explained by the effect of the tilt of CuO_6 octahedra in the LTO phase [10, 4]; the details will be discussed in the section of "Discussion".

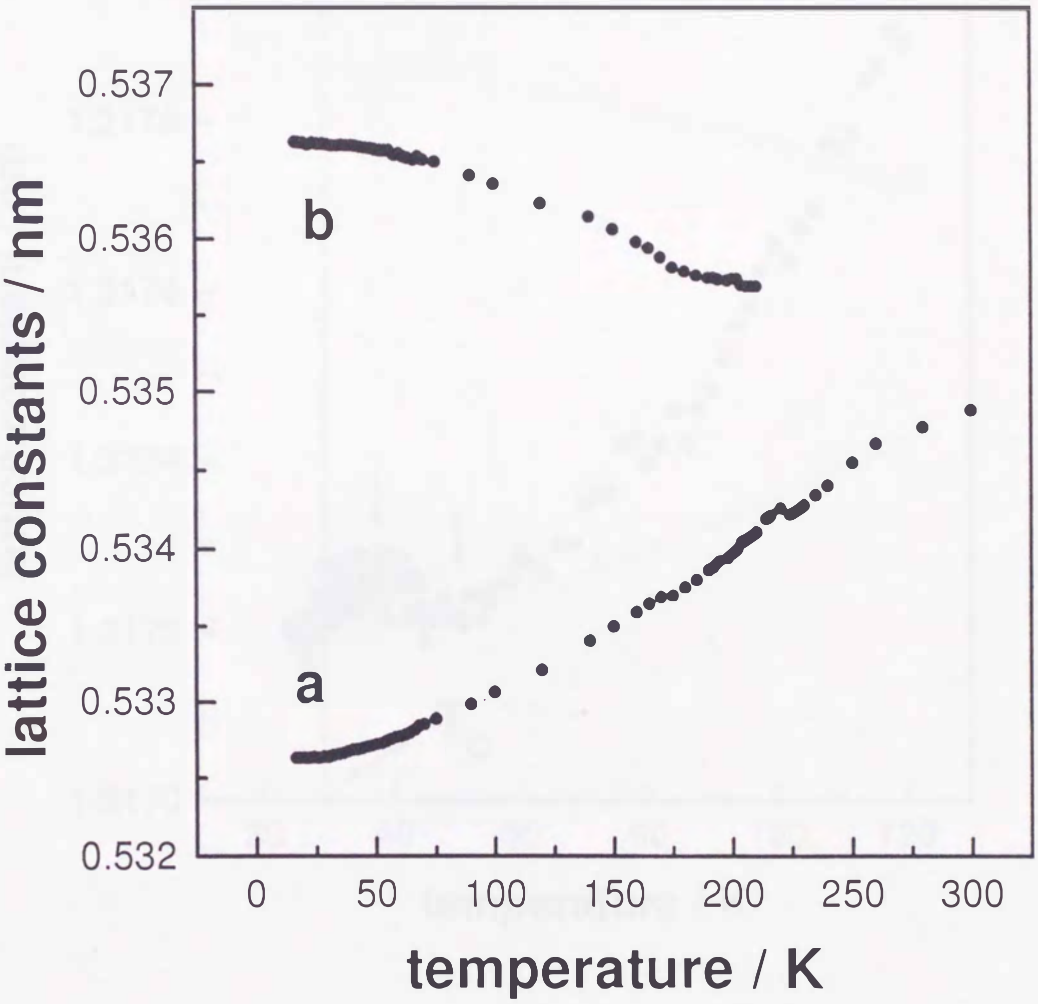

Figure 21: The temperature dependence of the lattice constant c for specimen B in the temperature range from 18 to 300 K.

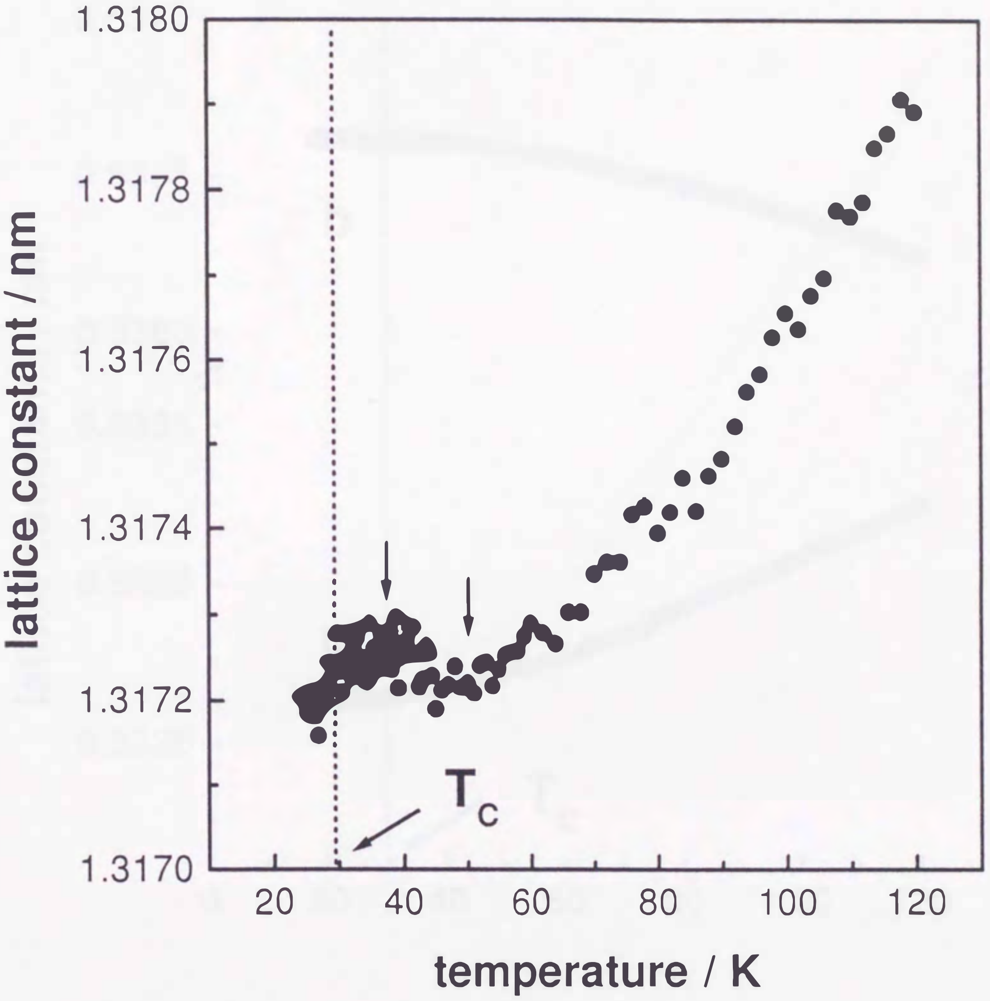

Figure 22: The temperature dependence of the lattice constants c of specimen B below 120 K.

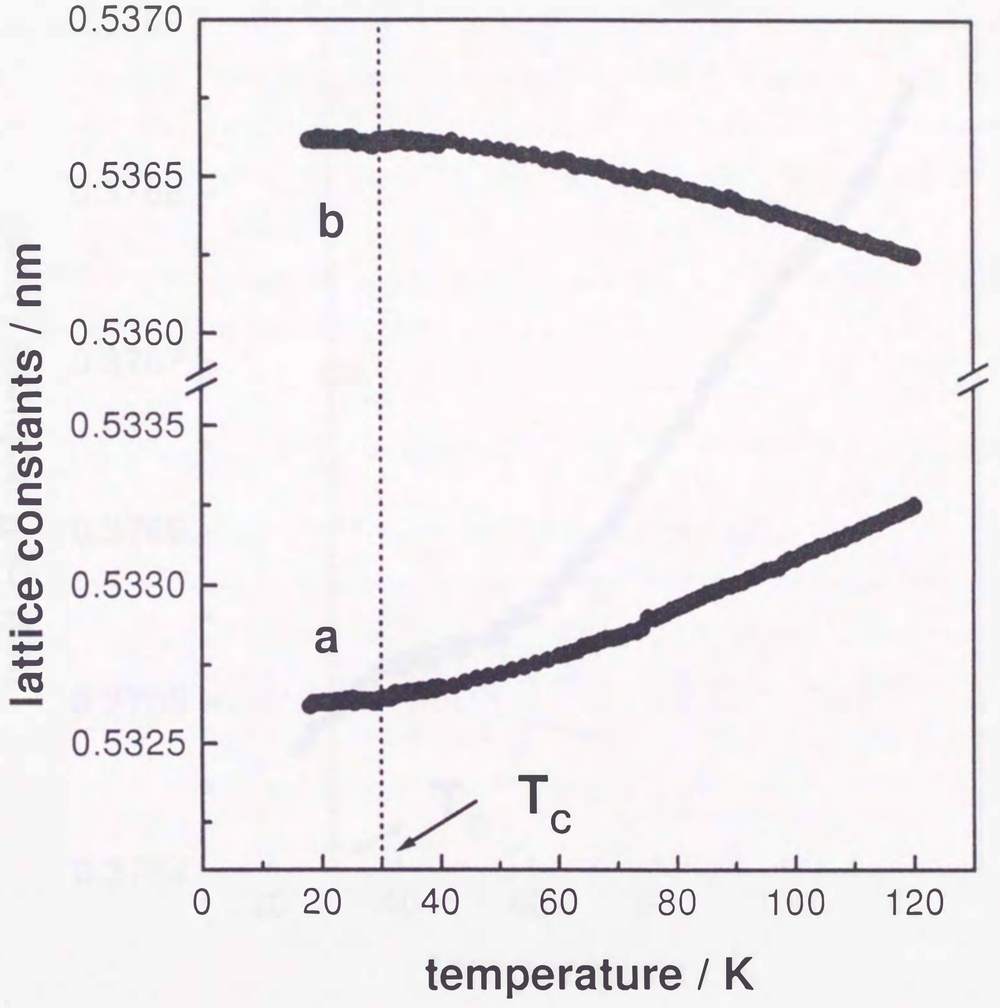

Figure 23: The temperature dependence of the lattice constants a and b of specimen B below 120 K.

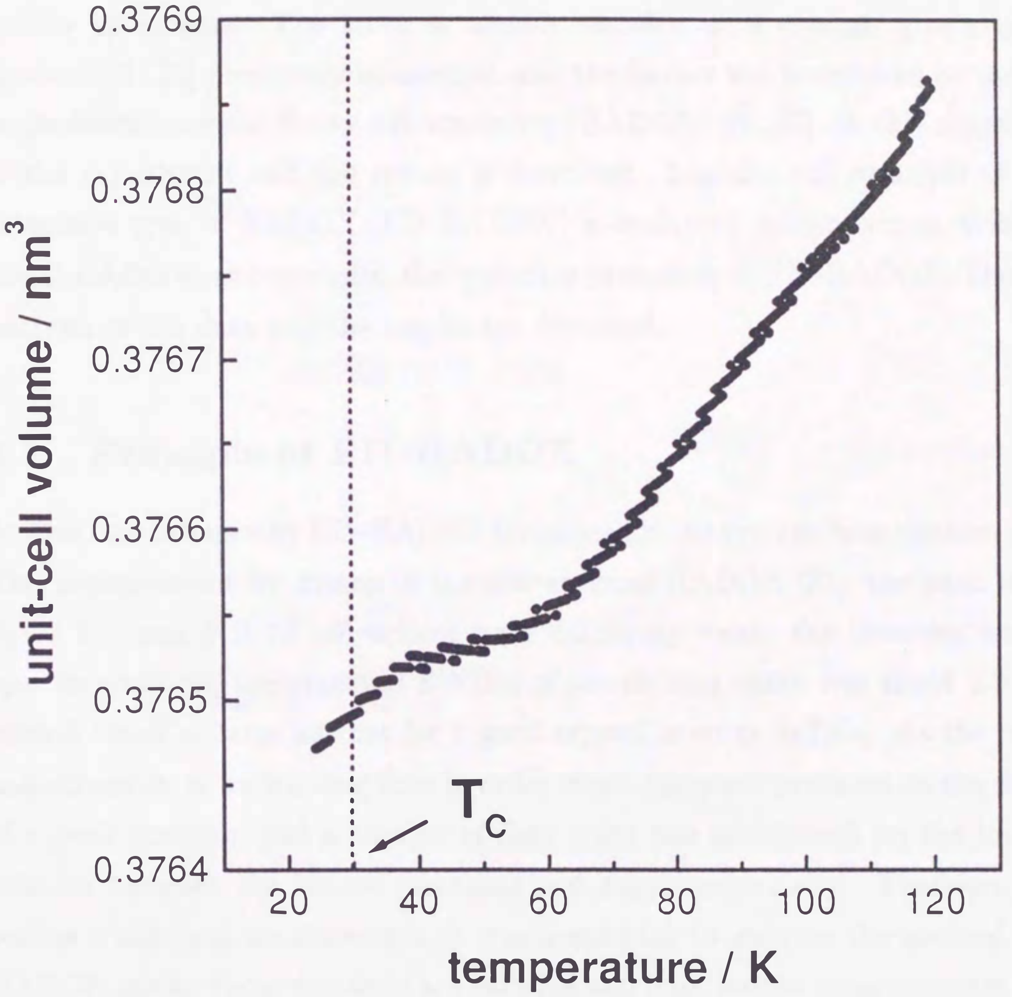

Figure 24: The unit–cell volume of specimen B as a function of temperature below 120 K.

4 ED–HADOX experiments

For a further discussion of the relation between the lattice strain and the appearance of superconductivity, the pricise information on the temperature dependence of lattice constants is required. For this, we need the high–resolution measurement and high–quality specimens. The latter is already satisfied with crystals grown by the TSFZ method [21, 22] previously mentioned, and the former will be achived by means of high–angle double–crystal X–ray diffractometry (HADOX) [26, 27]. In this chapter, the detail of the experiment and the results is described. Initially, the principle of the energy–dispersive type of HADOX (ED–HADOX) is explained in comparison with the conventional HADOX, and secondly, the operation procedure of ED–HADOX. Then finally, the analysis of the data and the results are discussed.

4.1 Principle of ED–HADOX

At first, the reason why ED–HADOX is required in the present investigation is mentioned. The measurement by means of the conventional HADOX [23], the peak intensities for the 2 2 0 and 0 0 14 diffractions were extremely weak; the intensity was about 300 cps. In addition, the observed FWHM of the rocking curve was about 2.9 mrad and is several times as large as that for a good crystal, such as $SrTiO_3$. As the result, for the measurement, it took a long time in order to get adequate precision on the determination of a peak position, and a number of data point was not enough for the investigation of relation between the lattice constants and superconductivity. Therefore, in order to realize a practical measurement, it was neccessary to improve the method. In the ED–HADOX mode, these demands are satisfied and high precise measurements can be made in the limit of an utilizable machine time.

The experimental arrangement of ED–HADOX is shown in Fig. 25. In common with the conventional HADOX, ED–HADOX requires the following conditions for high accuracy and precision: Firstly, two crystals must be arranged in the so-called $(+,-)$ parallel arrangement, and secondly, the Bragg angle (θ) of two diffractions must be high enough ($\theta > 70°$). The former condition makes FWHM of the observed rocking curve narrower than that observed by other methods using a single diffraction process, since a double–crystal $(+,-)$ arrangement results in non–dispersive diffraction. This brings about the precise determination of Bragg peak positions. On the other hand, the latter condition results in the increment of sensitivity to a change in the lattice constant. This situation

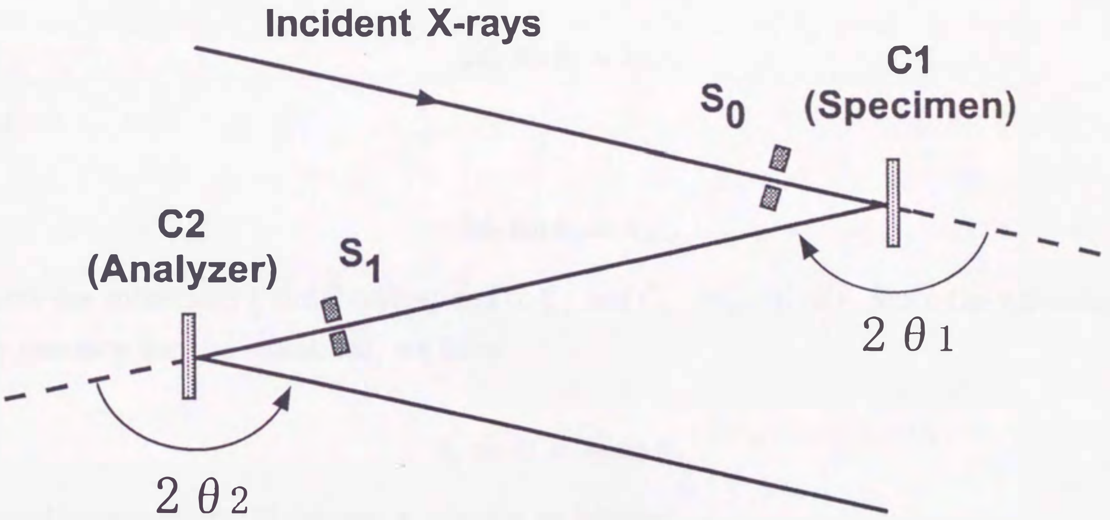

Figure 25. A schematic layout of ED–HADOX.

can be explained by diffrentiating the Bragg equation: $\Delta d/d = -\cot\theta\Delta\theta$. In order to discuss the sensitivity of HADOX, the formula will be transformed as follows:

$$\frac{\Delta\theta}{\Delta d} = -\frac{\tan\theta}{d}, \tag{4}$$

where θ and d denote the Bragg angle and the lattice spacing respectively. Equation (4) shows that the sensitivity is proportional to $\tan\theta$; diffractions at higher angles therefore give the higher sensitivity of $\Delta\theta$ to Δd. A detailed discussion is given by Okazaki and Ohama [26].

For ED–HADOX, the specimen crystal is the first crystal C_1, and coupled with the analyzer crystal C_2. The incident beams to C_1 are white X–rays, and therefore, the Bragg equations at C_1 and C_2 are expressed as follows:

$$2d_1\sin\theta_1 = \lambda_1, \tag{5}$$

and

$$2d_2\sin\theta_2 = \lambda_2, \tag{6}$$

where the subscripts 1 and 2 correspond to C_1 and C_2, respectively. Since the wavelengths are common for the equations, we have

$$d_1\sin\theta_1 = d_2\sin\theta_2. \tag{7}$$

Rewriting equation (7), we get a relation as follows:

$$d_1 = \frac{d_2}{\sin\theta_1}\sin\theta_2 = A\sin\theta_2, \tag{8}$$

where A is constant because θ_1 is fixed and d_2 is kept constant. It is clear that a change in the Bragg angle of the analyzer crystal θ_2 corresponds to a change in the lattice spacing of the specimen crystal d_1: i.e., the change in the X–ray wavelength diffracted at the specimen crystal is caused by the change in d_1, and then that is analyzed by the second crystal. This diffractometry is therefore named ED–HADOX. In the ED–HADOX, the two slits S_0 and S_1 are introduced, and placed in front of C_1 and C_2 respectively as shown in Fig. 25. They limit the angular divergence of incident X–rays to C_1 and the energy divergence of diffracted beams from C_1, respectively. Therefore, the resolution of the system for the lattice constant measurements is determined with the sizes of the slits. The detailed discussion of the resolution of the ED–HADOX is given by Fujii [28].

4.2 Operation mode of ED–HADOX measurements

In the following, a practical way of assemble apparatus of ED–HADOX and adjust the aligment of crystals will be explained. The ED–HADOX measurements has been improved from the conventional HADOX diffractometer settled at the Centre of Advanced Instrumental Analysis, Kyushu University. In Fig. 26, the configuration of ED–HADOX and the electoronic controller systems are shown. Two goniometers are placed on the diffractometer table installed in X–ray generator. The first and second goniometer are respectively for ω rotation of C_1 and C_2, and produced by HUBER Inc. (Model400) and KOHZU Inc. (KT10G2). The specimen and analyzer crystals are mounted on the closed cycle type of cryostat and the conventional type of thermostat respectively. The slits S_0 and S_1 are set for the aim mentioned in Sec. 4.1; the shape of S_0 is a hole of which size is changeable from 0.1 to 2.0 mm, and that of S_1 is rectangle of which the size is variable from 10 to zero mm in both perpendicular and horizontal directions. S_0 is set at the end edge of the first beam pass toward the specimen, and S_1 is mounted on the X–Y–Z table so that the position of the slit can be precisely adjustable to the position. The beam passes are evacuated in order to reduce the intensity loss by air absorption or scattering. The detector, for which NaI scintillation counter (SC) made in Bicron co. was used, is fixed on the 2θ arm installed in the second goniometer.

In Fig. 27, the deatail description around the sample holder for specimen crystal is shown. The specimen was glued by Si grease on the specimen holder made in copper,and is binded by Maylar film. The specimen holder was mounted on the end of the cold head of cryostat; indium foil is seated between them for well heat propagation. Si diode temperature senser is used for monitoring the temperature of specimen, and used for the temperature control by PID type of temperature controller (Lakeshore DRC–91CA). Manganin wires are winded around the end of the cold head for heating supply. The stability and the homogenity of the temperature on specimen was assured within ±0.02°. The temperature of the analyzer crystal is controlled by the PID controller made by Ohkura; the copper–constantan thermocouple thermometers and manganin wire were supplied for the temperature sensor and the heater, respectively. The temperature of the analyzer crystal was fixed at 310 K, and the stability of the temperature in the analyzer crystal is within ±0.05 K.

As shown in Fig. 26, three electronic devices are fully controlled by a personal computer through GP–IB interface; they are the temperature controller (DRC–91CA), pulse motor controller (DN–2000) connected with two motor drivers (SD–2000), and counter (C–

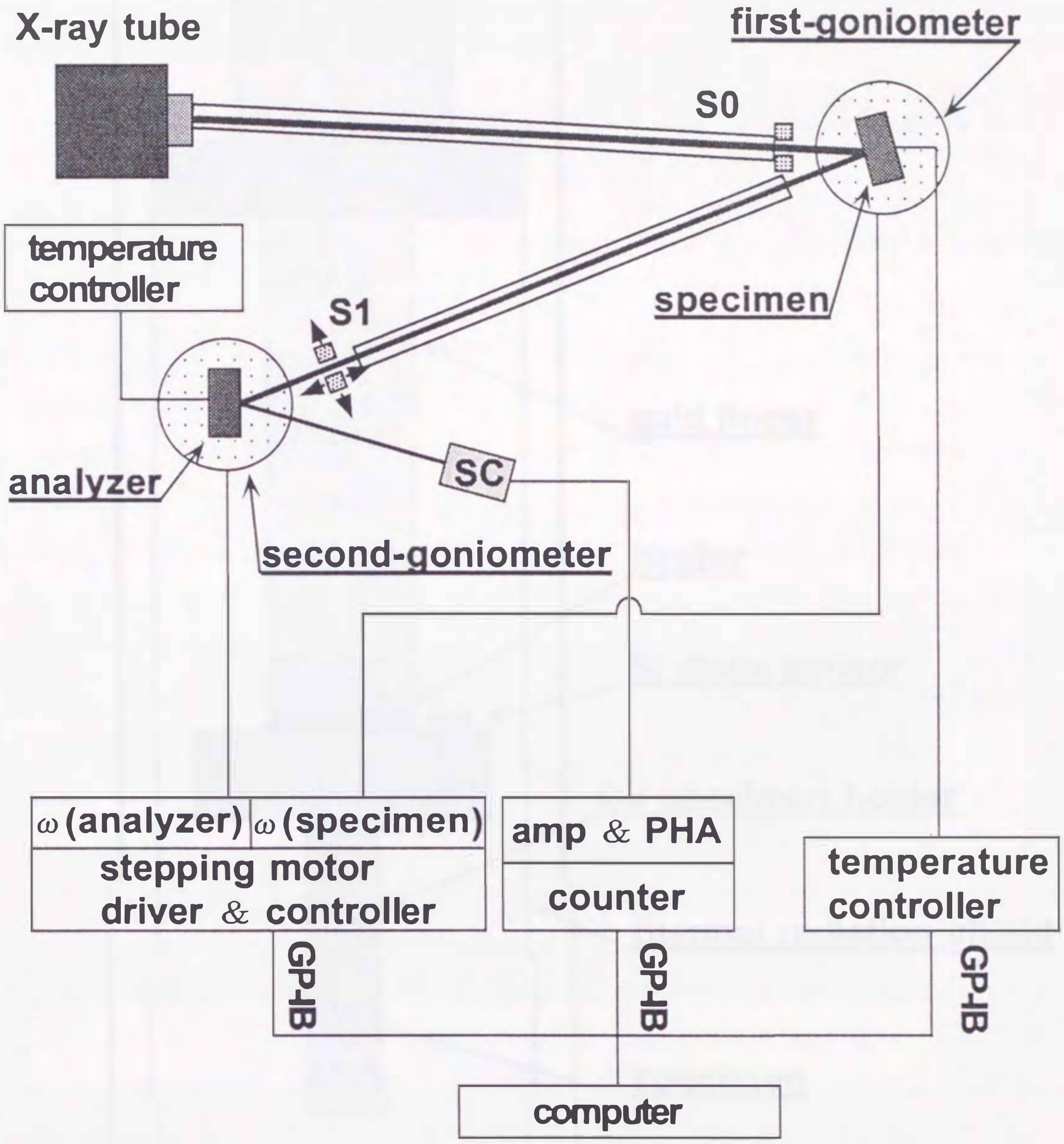

Figure 26. The control system of ED–HADOX.

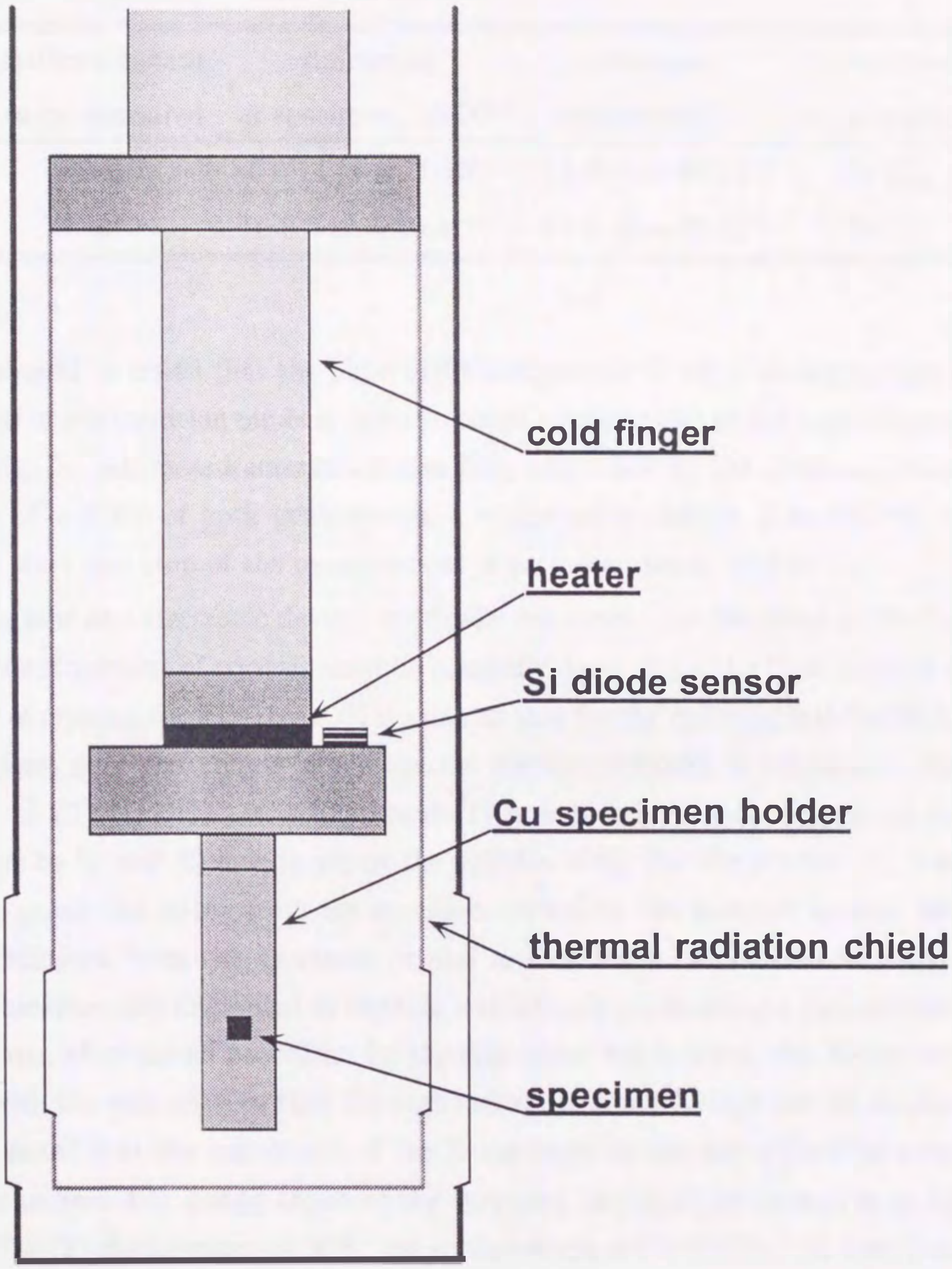

Figure 27. The specimen crystal and the surroundings.

Table 6: The condition for aligning the specimen and analyzer crystals. Conditions are labeled by H1 and H2, respectively.

label	lattice constant to be measured	diffraction at specimen (LSCO)	diffraction at analyzer(Si)	X–rays used for alignment
H1	c	0 0 14 ($\theta = 71.56°$)	4 4 0 ($\theta = 68.70°$)	Co $K_{\alpha 1}$
H2	a	6 0 0 ($\theta = 80.41°$)	4 4 0 ($\theta = 66.22°$)	Fe K_β

2000). It should be noted that the pulse hight analyzer for X–ray counting system must be operated in a integration mode in order to count whole signals of the higher harmonics of $\lambda/2$, $\lambda/3, \cdots$. All measurements are also fully controlled by the personal computer; a rotation of ω circle of both goniometers, a temperature change, a continuous count, automatic start and stop of the measurement of each scan mode, and so on.

All apparatus and electronic devices are finally constructed as discribed in the Fig. 26, however, the alignment of crystals must be manually done. Since the basic method of the alignment of crystals for ED–HADOX is same as that for the conventional HADOX [27], and therefore, only the unique procedure for the ED–HADOX is explained. For the alignment of ED–HADOX, it is important (1) how to adjust each crystals to limited Bragg angle by S_1 and (2) how to adjust the position of S_1. For the process (1), it is very difficult to guide the X–ray from the specimen crystal to the analyzer crystal, because Bragg diffractions from the specimen crystal are caused in all directions with white X-rays. Therefore, the alignment of crystals was initially made using a characteristic X–ray, and then, after the all procedure for the alignment was finished, the X–ray target is replaced with the gold (Au) so that the high briliant of white X–rays can be obtained. It should be noted that the wavelength of the X–ray must be selected within the condition mentioned in Sec. 4.1: Bragg angles of the specimen and analyzer crystal is as high as possible. For (2) the adjustment of S_1, use of topograph is convenient. At first, standing a pin at the centre of the second goniometer, the topograph of specimen is taken. Since the shadow of the pin is observed on the topograph of specimen, the position of S_1 is adjusted so that the shadow corresponds with the centre of the topograph. By this procedure, the position of S_1 can be accurately determined. The condition for alignment is listed in Table. 6. The condition for alignment is different in each diffraction, and therefore, the alignment were made at the first stage of each measurement.

Table 7. The experimental condition for determination of size of S_1.

Power	50 kV, 150 mA
monitoring time	100 s
ω step	10 sec.
range of ω scan	600 sec.
S_0 size	5.0 mm
S_1 size	3.0, 2.0, 1.0, 0.5, 0.2, 0.1 mm
specimen temperature	14 K

4.3 Preliminary experiment

In order to examine the performance of the diffractometer, a preliminary experiment has been carried out and the optimization of the condition has been made. Initially, the resolution of the system is examined as the function of the size of S_1. Secondly, the two–dimensional intensity distribution in reciprocal space is determined by the fω–ω two–dimensional scan mode, and the quality of specimen is characterized. Finally, the energy spectroscopy is made for the investigation of energy content in the diffracted X–rays.

4.3.1 Two–dimensional measurements

The size of S_1 is an imprtant factor for the determination of resolution, and thus, ω–scan is carried out as a function of the slit size under the optical system H1 given in Table 6. The conditions for the measurement are listed in Table 7.

Examples of the observed rocking curve are shown in Fig. 28. The ratio of signal to noise (S/N) decreases with decreasing size of S_1. All the rocking curves are defined by the Lorenz function and a non–linear least squares ayalysis has been made for the determination of integrated intensity and FWHM. The results are shown in Fig. 29. Both integrated intensity and FWHM decrease with decreasing slit size; FWHM is nearly constant for S_1=0.5 mm. Therefore, as an optimum condition in connection with the intensity and FWHM, the size of S_1 was set for finally 1.0 mm.

The two–dimensional scan mode is used for measuring the intensity distribution of reciprocal lattice point in the diffraction plane. The intensity distribution contains in-

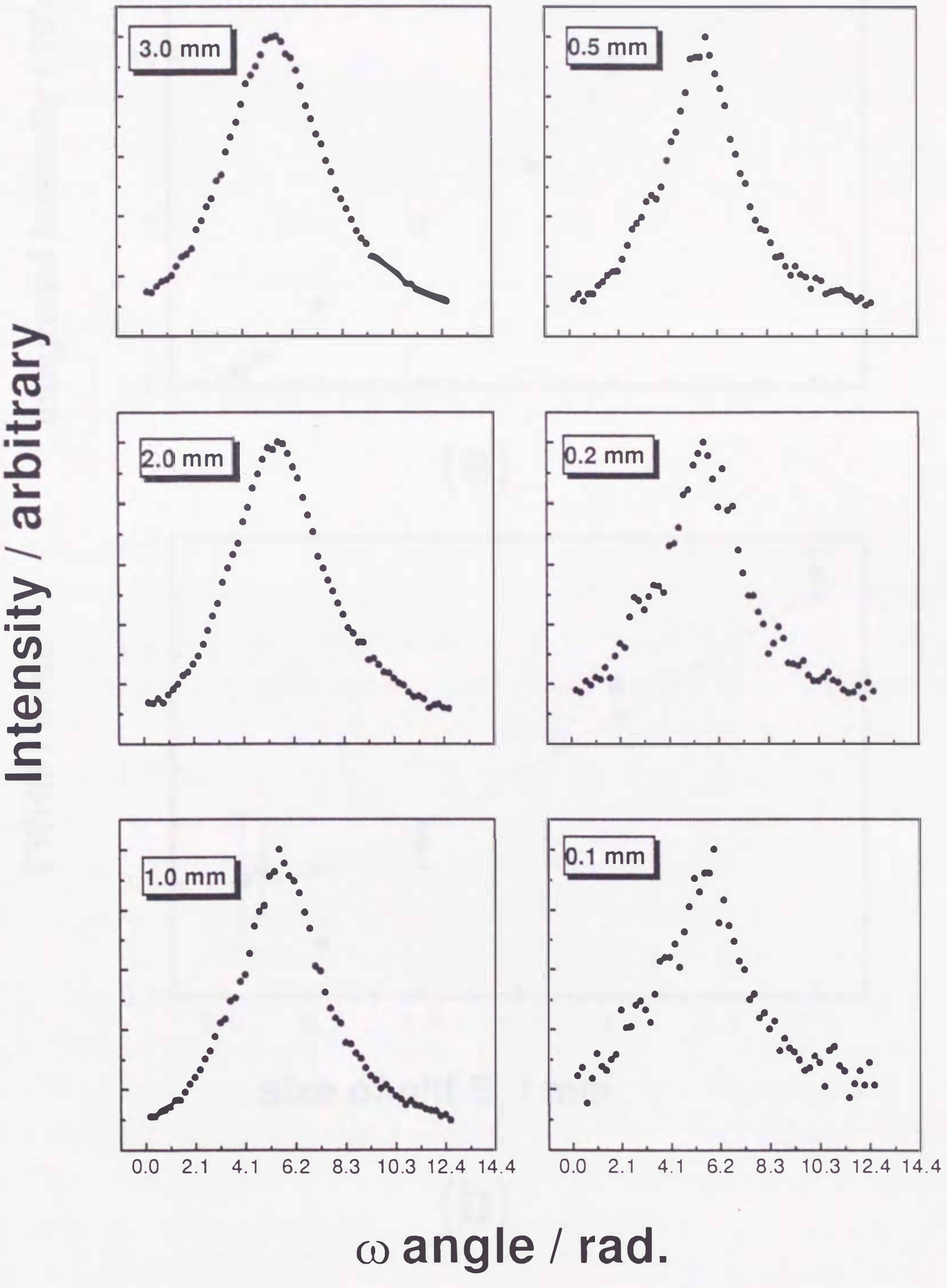

Figure 28: Examples of the rocking curve of the analyzer crystal for various size of slit S_1.

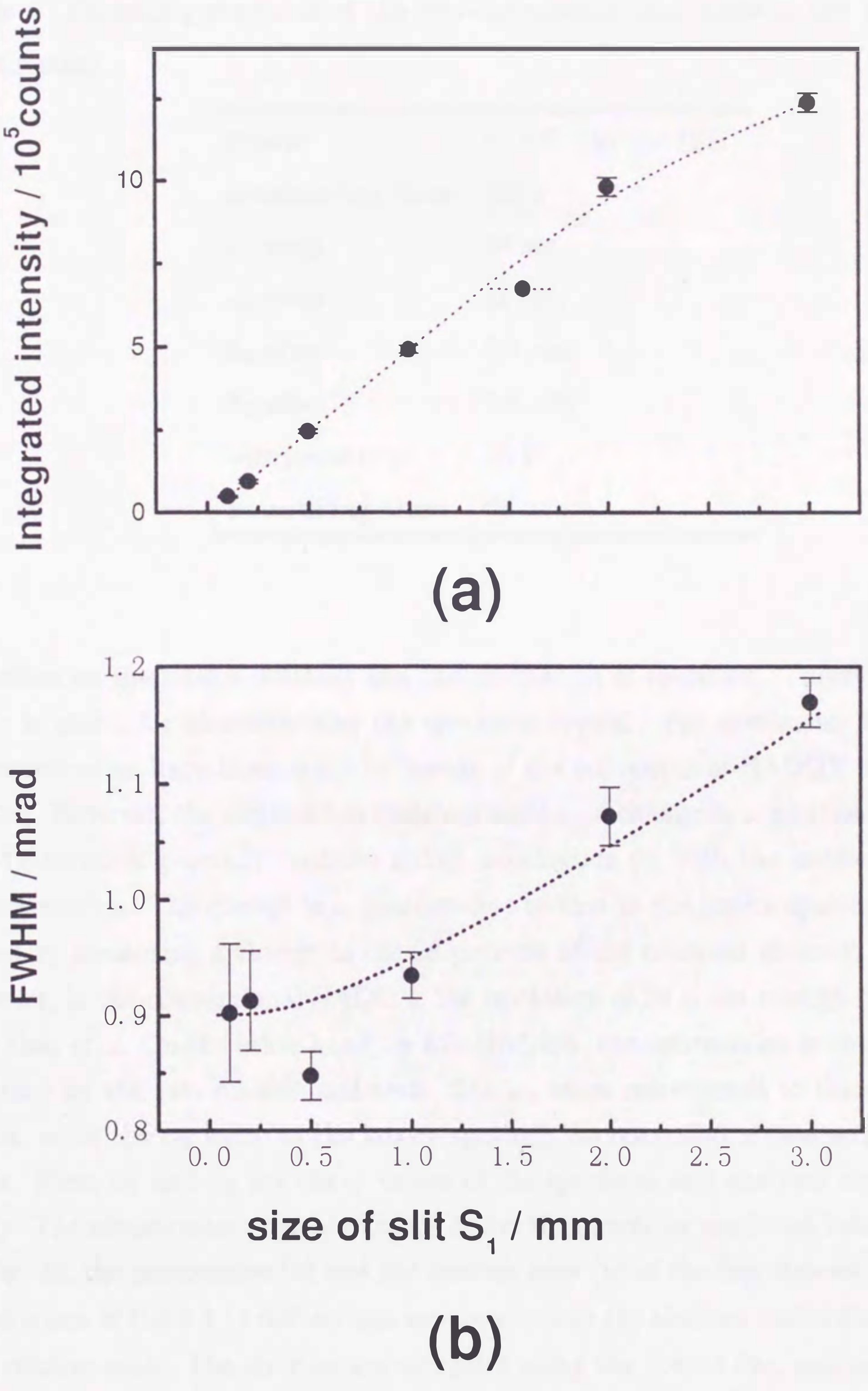

Figure 29: (a) Integrated intensity and (b) FWHM of the rocking cureve vs. the size of slit S_1.

Table 8: Operating condition of the two–dimensional scan mode in the ED–HADOX measurement.

Power	50 kV, 150 mA (Cu)
monitoring time	100 s
ω_1 **step**	36 sec.
ω_2 **step**	15 sec.
S_0 **size**	5.0 mm
S_1 **size**	1.0 mm
temperature	14 K
measuring time	28 hours

formation on the lattice constant and the orientation of specimen. Therefore, this scan mode is useful for characterizing the specimen crystal. For specimens A and B, the characterization have been made by means of the conventional HADOX in 2θ–ω scans [23, 24]. However, the method has disadvantage:i.e., a change in ω position of the intensity distribution generally contains mixed information on both the lattice spacing and the orientation. The change in ω position due to that in the lattice spacing can be separated by measuring a change in the 2θ position of the observed intensity distribution. However, in the conventional HADOX, the resolution of 2θ is not enough in comparison with that of ω. On the other hand, in ED–HADOX, the information is obtained in high accuracy by the two–dimensional scan. The ω_1 value corresponds to the crystal orientation, while the ω_2 value to the lattice spacing; the resolution is comparable for these scans. Here, ω_1 and ω_2 are the ω values of the specimen and analyzer crystals respectively. The measurement has been made under the operating condition listed in Table 8. In Fig. 30, the perspective (a) and the contour map (b) of the two dimensional intensity distribution of the 0 0 14 diffractions are shown; both the abscissa and ordinate are given in a relative scale. The distribution elongates along the dotted line, and consists of two peaks as pointed with arrows. The peaks are separated by about 1.2 mrad along the ω_1– and ω_2– axes. Since the intensity distribution in ω_2 indicates the variation of the lattice spacing, the values of the lattice constant c corresponding to these peaks are determined to be 1.3194 and 1.3199 Årespectively. It is to be noted that the difference between these values cannot be not attributed to inhomogeneity of temperatue in specimen, because the lattice constant at 14 K is non–sensitive for temperature. The difference must therefore be attributed to inhomogeneity of Sr concentration x. The situation is similar to the case of the 2θ–resolved HADOX experiment [23]. According to the relation between the lattice constant and Sr concentration given by Radaelli *et al.* [25], we find that the separation of 0.005 Åbetween the two peaks corresponds to the difference 0.01 in x: the results are consistent with those of the 2θ–resolved HADOX [23]. Furthermore, the ω_1 values of the peaks are also different. This means that the orientation of the fractions corresponding to the two peaks is different to each other; these results are not consistent with the results of the 2θ–resolved HADOX experiment [23]. This is probably due to inadequate accuracy and precision of the 2θ–scan. These results suggest that the characterization of a crystal by ED-HADOX is superior to that by the conventional HADOX. In the measurement of temperature dependence of the lattice constant c, the ω_1 position is fixed at $\omega_1 = 0$. For that of the lattice constant a, a similar optimization is attained.

4.3.2 Energy–dispersive measurements

Since white X–rays are used as the incident beam, diffractions from the analyzer crystal contain the harmonics of λ, $2\lambda/3$, $\lambda/2$, and $\lambda/3$ corresponding to the 0 0 14, 0 0 21, 0 0 28 and 0 0 42 diffractions respectively. The proprotion of the intensity for the harmonics give information on the size of the portion in specimen attributed to the diffraction. The energy spectra of the diffractions have been examined with a solid state detector (SSD); ω_1 and ω_2 are fixed at a position of the maximum of two–dimensional intensity distribution. The signal from SSD are analyzed by multichannel analyzer (MCA). The results of the 0 0 l and h 0 0 diffractions are respectively shown in Figs. 31 and 32 in the semi–logarithmic scale. Peaks is assigned as shown in the figures. In both figures, the peaks of Cu K_α and Zn K_α is observed. These are due to the materials used in experimental apparatus. Furthermore, the 0 0 l diffractions contain four peaks attributed by the harmonic waves λ, $2\lambda/3$, $\lambda/2$, $\lambda/3$ and the h00 diffractions three peaks attributed by those λ, $\lambda/2$,$\lambda/3$: λs for the 0 0 l and h 0 0 diffractions correspond to the wavelength of Co $K\alpha_1$ and Fe $K\beta$ respectively. For both diffractions, the main contributions for diffractions are primitive indices 0 0 14 and 6 0 0. The penetration depth ξ for X–ray of λ is defined by

$$\xi = \frac{\log 2}{\mu\rho} = \frac{0.69315}{\mu\rho}, \tag{9}$$

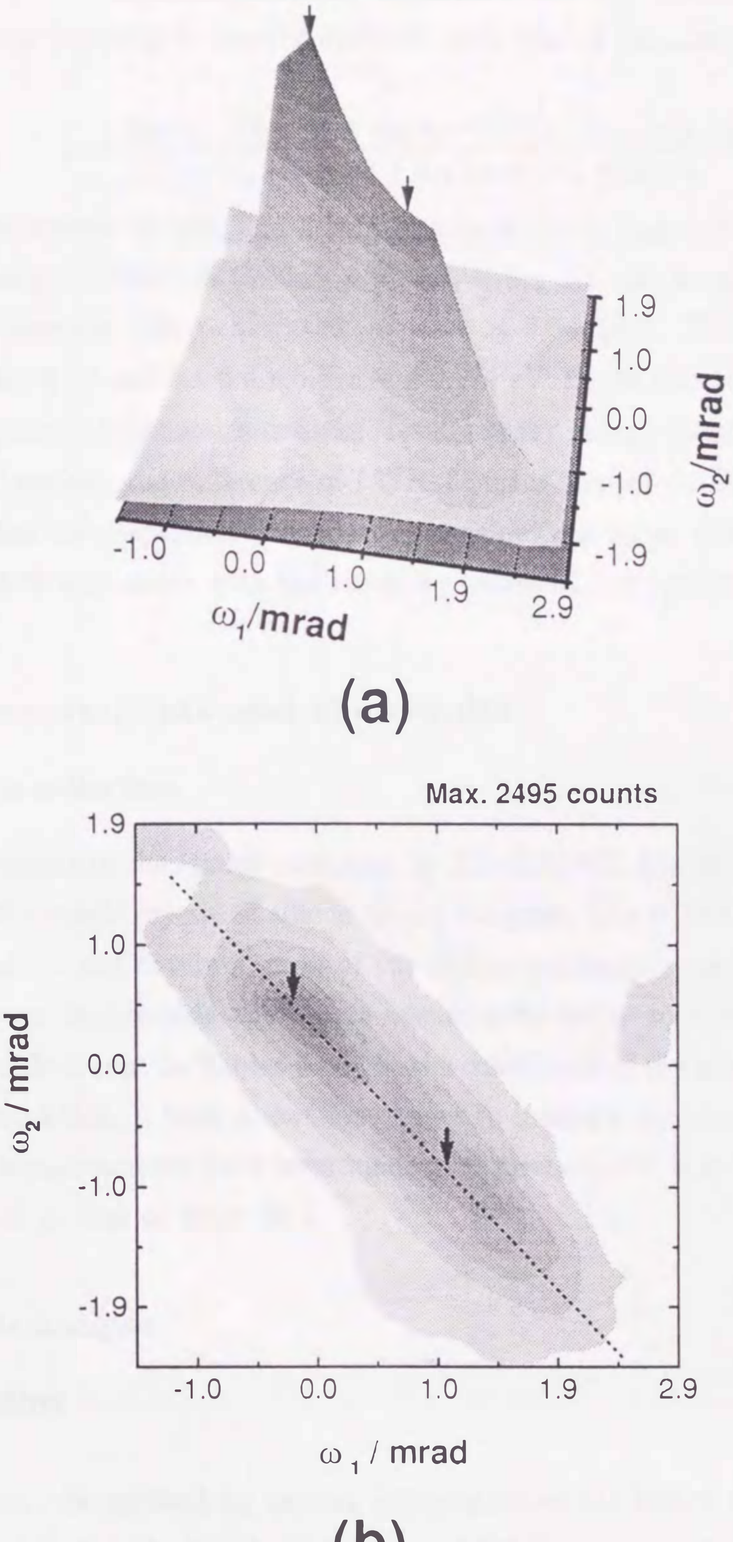

Figure 30: (a) The perspective and (b) contour map of two–dimensional intensity distribution of the 0 0 14 diffraction. The two peaks are pointed with arrows.

where μ and ρ are the mass absorption coefficience and the mass density respectively. μ depends on the wavelength and the material, and, that of $La_{2-x}Sr_xCuO_4$ is expressed by

$$\mu = \frac{\mu_{La} a_{La} \cdot (2-x) + \mu_{Sr} a_{Sr} \cdot x + \mu_{Cu} a_{Cu} + \mu_O a_O \cdot 4}{a_{La} \cdot (2-x) + a_{Sr} \cdot x + a_{Cu} + a_O \cdot 4}, \qquad (10)$$

where a is an atomic weight, and a subscript indicates μ and a of each atom. Using μs of the wavelength 1.78892 Å(CoKα), μ for $La_{1.857}Sr_{0.143}CuO_4$ is calculated as 3.52×10^5 $[1/m]$, and therefore, the penetration depth ξ is 5.64 $[\mu m]$. Furthermore, FWHM of main peaks for 0 0 l and h 0 0 are 0.513 and 0.277 eV. In the ED–HADOX configuration, the inhomogenity of the lattice constant results in the energy inhomogenity of diffracted beam, and therefore, the difference of FWHM means that of the lattice constant. Thus, it is found that the dispersion of the lattice constant c is larger than that of a. This fact is in qualitative agreement with the result by means of 2–θ resolved HADOX [23].

4.4 Measurements and the results

4.4.1 Data collection

The measurement of the lattice constants by ED–HADOX has been made only on specimen A, with a single crystal of silicon as the analyzer. The 0 0 14 and 6 0 0 diffractions are measured for the determination of the lattice constants c and a, respectively. The measurement of lattice constant b were unsuccessful owing to extremely weak intensity of the 0 6 0 diffraction. In Tables 6 and 9, the conditions of the measurements are listed. Under the condition, it took about four hours to measure a rocking curve at a temperature. The measurements have been made at a interval of 1 K in the range of 10 to 60 K, and of 2 K in that of 60 to 76 K.

4.4.2 Data analysis

Pattern fitting

In this section, the method for getting information on the lattice constant from the raw data will be mentioned. For the 0 0 14 and 6 0 0 diffractions, both rocking curves can be approximated by the function of Lorentze–type, as seen in Figs. 33. Therefore, the non–linear least square fitting (NLSF) with Lorentzian function has been applied to data analysis. The Lorentzian function are expressed as follows:

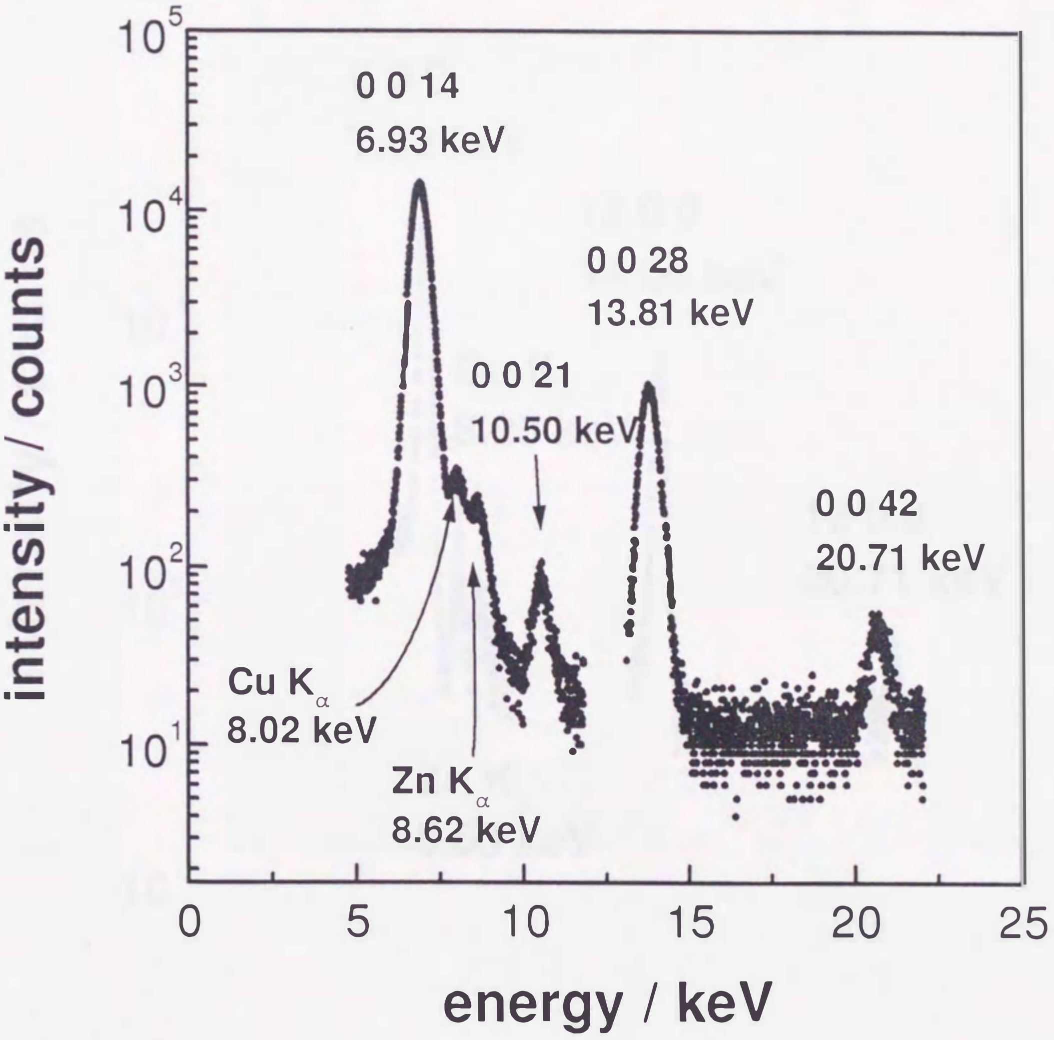

Figure 31: The energy spectra of the 0 0 l diffractions of LSCO emitted from analyzer crystal. Peaks are assigned in the figure.

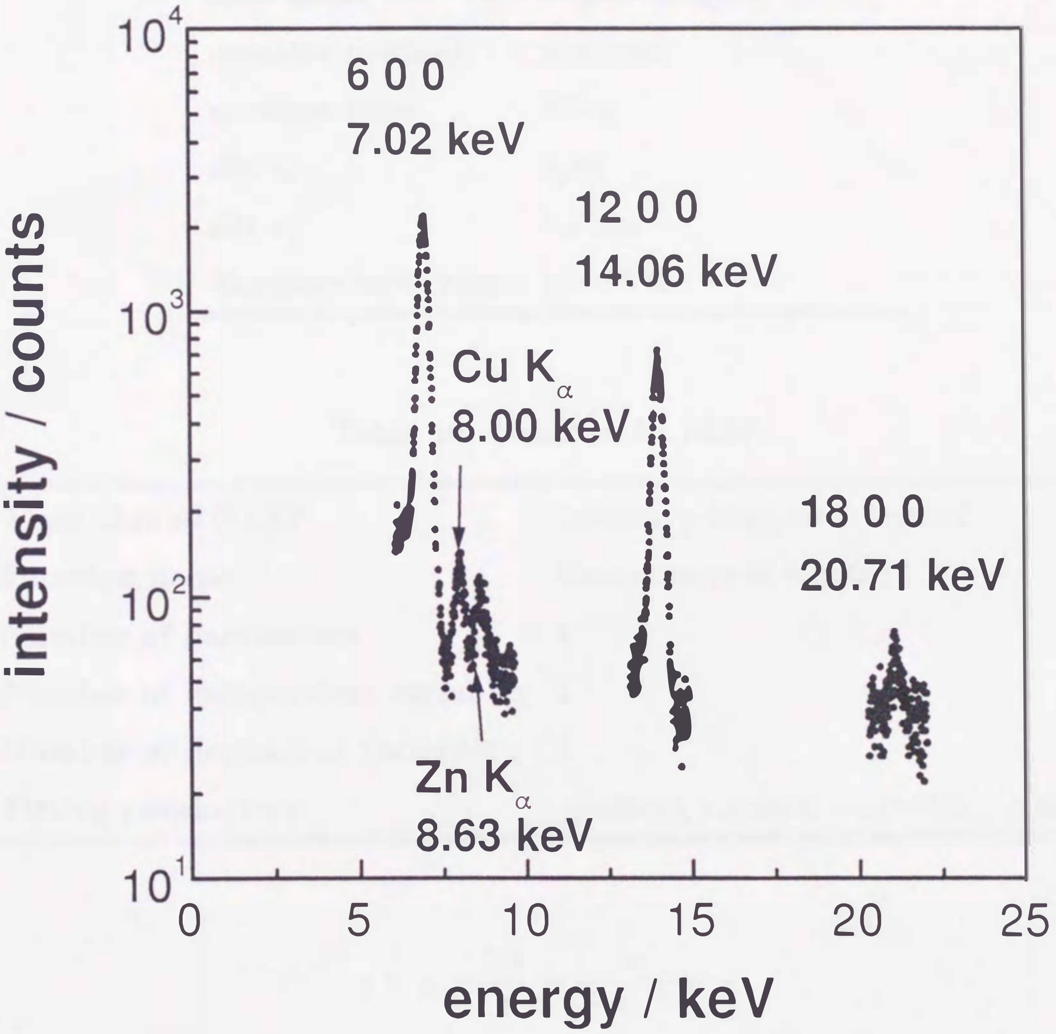

Figure 32: The energy spectrum of the h 0 0 diffractions of LSCO emitted from analyzer crystal. Peaks are assigned in the figure.

Table 9. The experimantal conditions of ED–HADOX measurements.

generator	50kV 150mA
target	Au
forcus size	0.5 × 1.0 mm (normal)
scan mode	ω–scan (analyzer crystal)
monitor method	step scan
monitor time	300 s
slit s_0	open
slit s_1	1.0 mm
Temperature range	10—76 K

Table 10. Condition for NLSF.

Algorithm of NLSF	Levenberg–Marquardt method
Function name	Lorentzian peak function
Number of parameters	4
Number of independent variables	1
Number of dependent variables	1
Fitting parameters	y_0(offset), x_c(center), w(width), A(area)

$$y = y_0 + \frac{2A}{\pi}\frac{w}{4(x - x_c)^2 + w^2}. \tag{11}$$

The detail description for NLSF is listed in Table 10.

In the figures, the results of NLSF were described as a solid line together with a measuring data, which was shown by a solid circle. Standard deviations of the fitting are analyzed as a error of ω position, and is shown for the all observed rocking curves in Fig. 34; errors are constant for all the fitting, and therefore, precision of the determination of peak position is same for all the measurements.

Calculation of the lattice constant

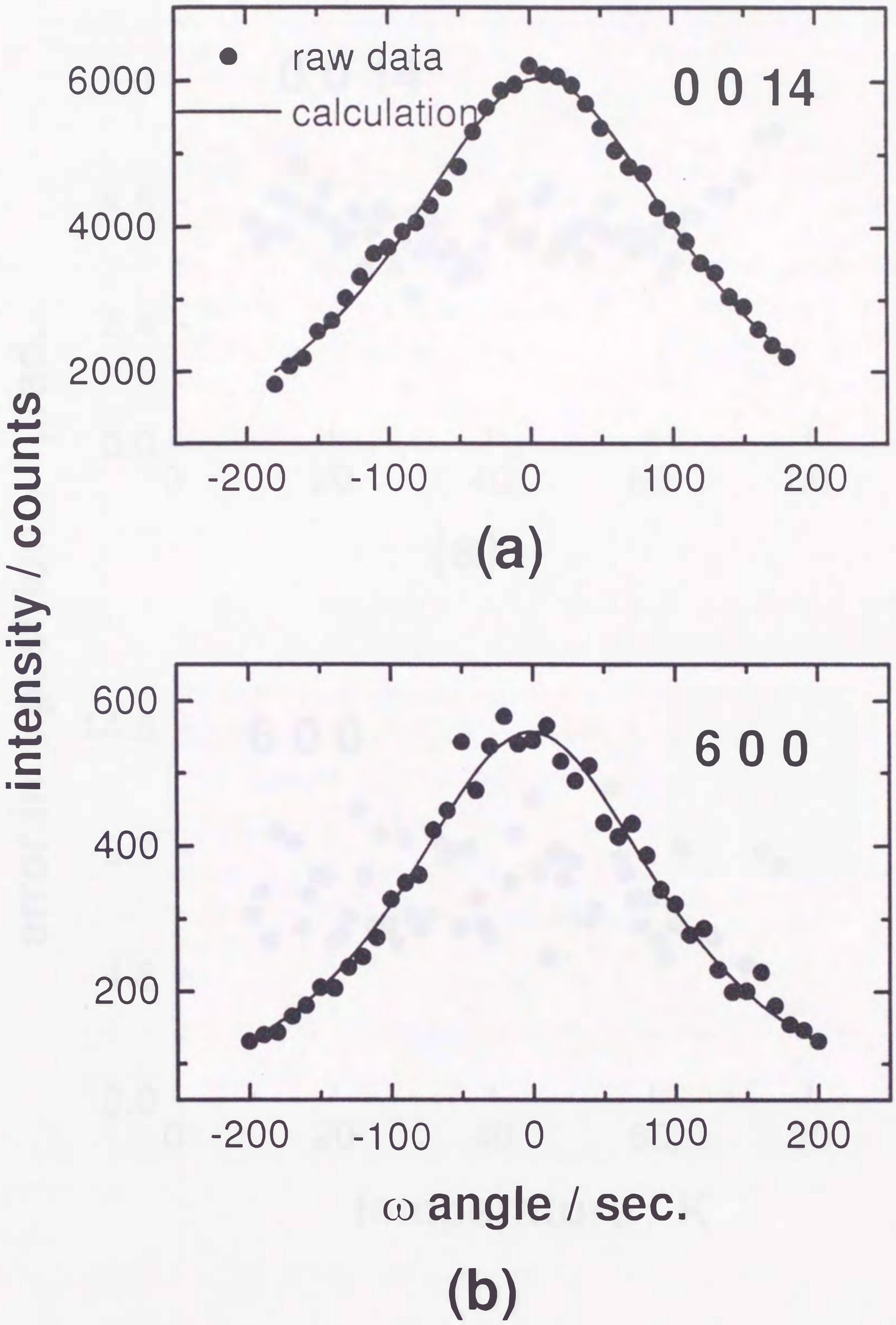

Figure 33: Examples of the observed rocking curve for (a) the 0 0 14 and (b) the 6 0 0 diffractions at 10 K. The solid lines indicate the results of non–linear least square fitting.

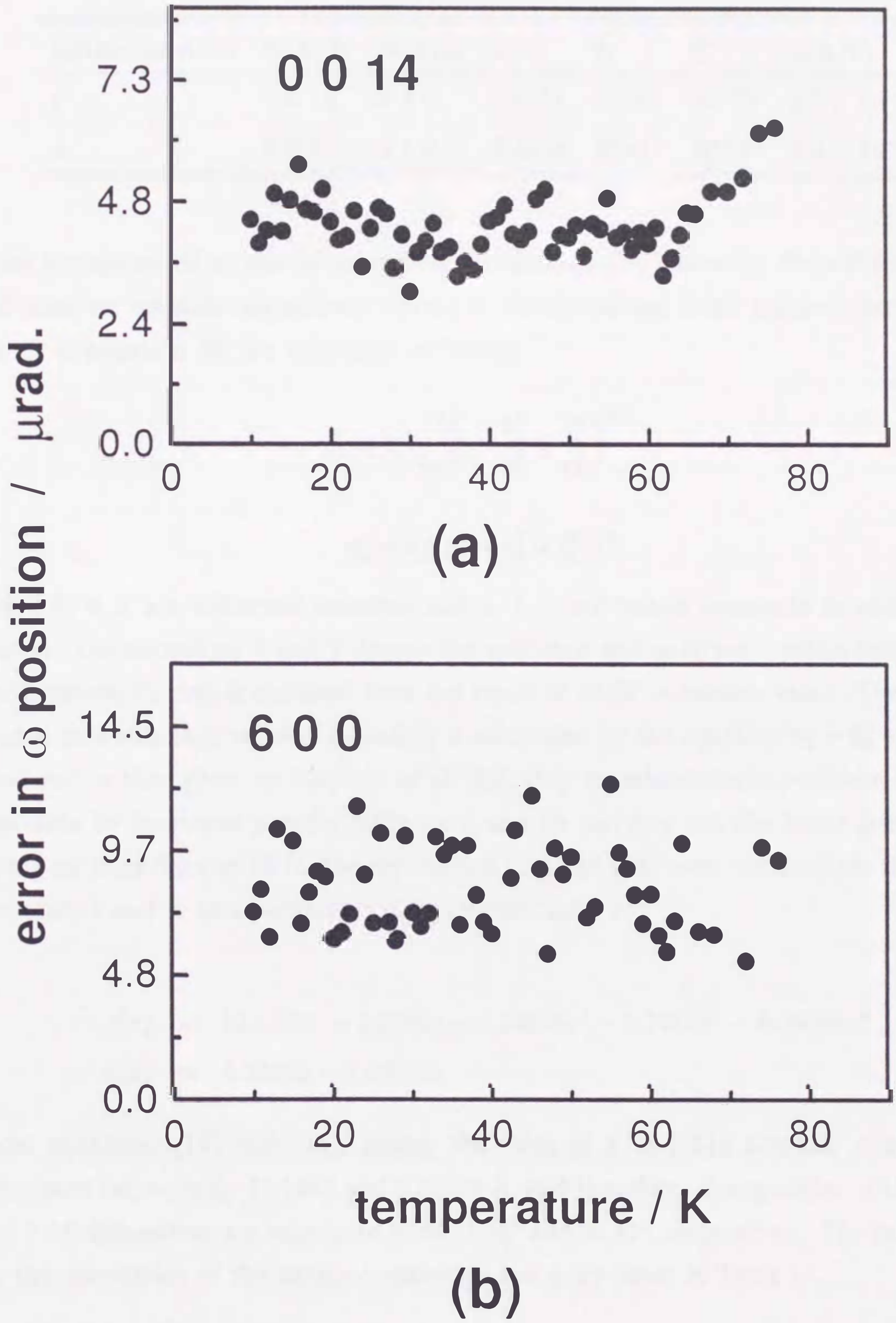

Figure 34: Errors in the peak position estimated from NLSF (a) for the 0 0 14 and (b) for the 6 0 0 diffractions.

Table 11. Various parameters used for calculating the lattice constant.

lattice constant	h_1 k$_1$ l$_1$	h_2 k_2 l_2	a_2	θ_1	θ_2^*	$\Delta d_1/d_1$
c	0 0 14	4 4 0	5.4308	71.56°	68.70°	1.7×10^{-6}
a	6 0 0	4 4 0	5.4308	80.41°	66.22°	3.9×10^{-6}

Using the optimized x_c, the lattice constant is calculated by following. Since the specimen and analyzer crystals respectively belong to tetragonal and cubic phases, therefore, d_1 and d_2 of equation (8) are expressed as follows,

$$d_1 = 1/\left(\frac{h_1^2}{a_1^2} + \frac{k_1^2}{b_1^2} + \frac{l_1^2}{c_1^2}\right)^{1/2}, \tag{12}$$

$$d_2 = a/(h_2^2 + k_2^2 + l_2^2)^{1/2}, \tag{13}$$

where h, k, l are diffracted indecies, and a, b, c are lattice constants in each crystal system. The subscripts 1 and 2 denote the specimen and analyzer crystals respectively. Furthermore, θ_2 that is obtained from the result of NLSF is relative value. Therefore,θ_2^* is used as a standard value of θ_2 and θ_2 is calculated by the equation $\theta_2 = \theta_2^* + \Delta x_c$. θ_1 is refered to that given by Radaelli *et al.* [25]; they examined the dependence of lattice constants by Neutoron powder diffraction, and by carrying out the linear least square fitting on their data at 10 K, the expressions (14) and (15) were obtained for the lattice constants c and a, as a parameter of Sr concentration x:

$$\begin{aligned} c(x) &= 13.11741 + 0.5786x + 0.33816x^2 - 5.2742x^3 + 6.05584x^4 && (14) \\ a(x) &= 5.33269 - 0.06064x && (15) \end{aligned}$$

From equations (14) and (15), taking the value of x as 0.143 account, c and a are calculated respectively 13.1942 and 5.32402 Å, and therefore, Bragg angles of the 0 0 14 and 6 0 0 diffractions are calculated to be 71.56° and 80.41°, respectively. The parameters for the calculation of the lattice constants c and a are listed in Table 11.

4.4.3 Results

Lattice constant

In Figs. 35 and 36, the determined lattice constants c and a are respectively shown as a function of temperature. In comparison with the results of the measurements by means of STOE diffractometer, it is clearly seen that the precision of ED–HADOX measurements is much higher; deviation of data points is much less than that in STOE measurements. For the temperature dependence of the lattice constant c, an strange behaviour is observed in the range of 10 K below T_c; c reaches the minimum at T_c and then shows a subtle increment. This is steeply decreasing again below around 30 to 20 K and remains below 20 K. Furthermore, some discontinuous behavior of lattice constant is observed in range of 60 K to T_c: the temperatures are indicated by arrows in the figures. According to the results of capacitance dilatometer given by Gugenberger *et al.* [5], the thermal expansivity of the crystal of twin structure shows discontinuous change in the same temperature range, while that of monodomain crystal shows no such behavior. Therefore, the observed disconinuities are probably attributed to the existence of twin structure in the specimen crystal. On the other hand, the lattice constant a is decreasing to low temperature region and only a subtle change of slope at T_c is observed. The discontinuity same as observed in c is also observed in a.

Integrated intensity

In Figs. 37 and 38, the temperature dependences of the integrated intensity for the 0 0 14 and 6 0 0 diffractions are shown respectively. In general, integrated intensity of Bragg diffraction increases with decreasing temperature according to Debye–Waller factor. However, that of the 0 0 14 diffraction reaches maximum at 60 K and is decreasing with decreasing temperature. The integrated intensity at 60 K increases about 20 % of that at 10 K. On the other hand, that of the 6 0 0 diffraction is almost independent on temperature. It is worth mentioning that the various anomaly on LSCO have been observed around 60 K [6, 14, 15, 18, 33], and furthermore, EXAFS and PDF measurements indicate that the local atomic structure deviates from the average crystallographic structure in low temperature range. These results imply that the dynamical and statistical instabilities on the crystal structure occure in low temperature range. Thus, the present results is probably related to the appearance of these structural anomaly;i.e, incoherent area for X-rays that corresponds to the deviation from the average structure may be increasing below 60 K. It is also noted that the observed behavior in the 0 0 14 diffraction is not observed in the 6 0 0 diffraction. This means that the structural instability is related with change of atomic position to c–axis direction.

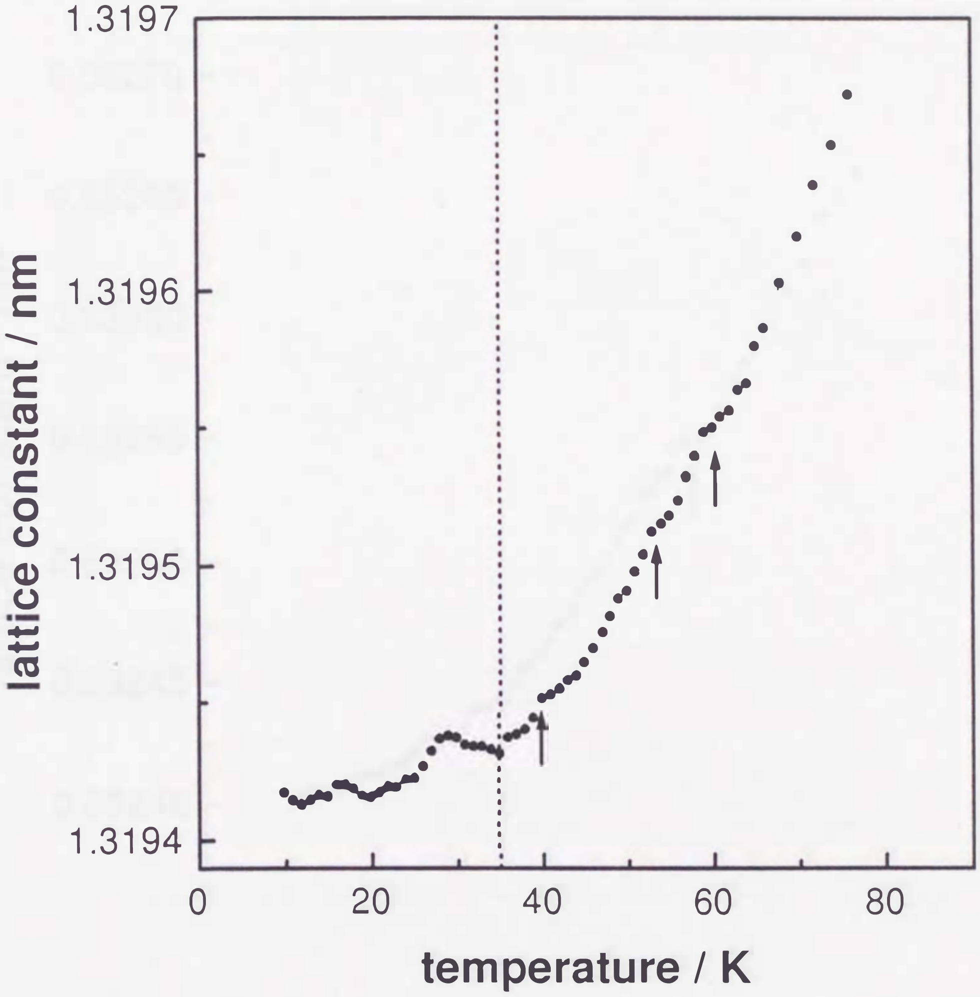

Figure 35: The temperature dependence of the lattice constant c. Dotted line and the arrows indicate $T_c (= 35K)$ and discontinuous behavior of the lattice constant, respectively.

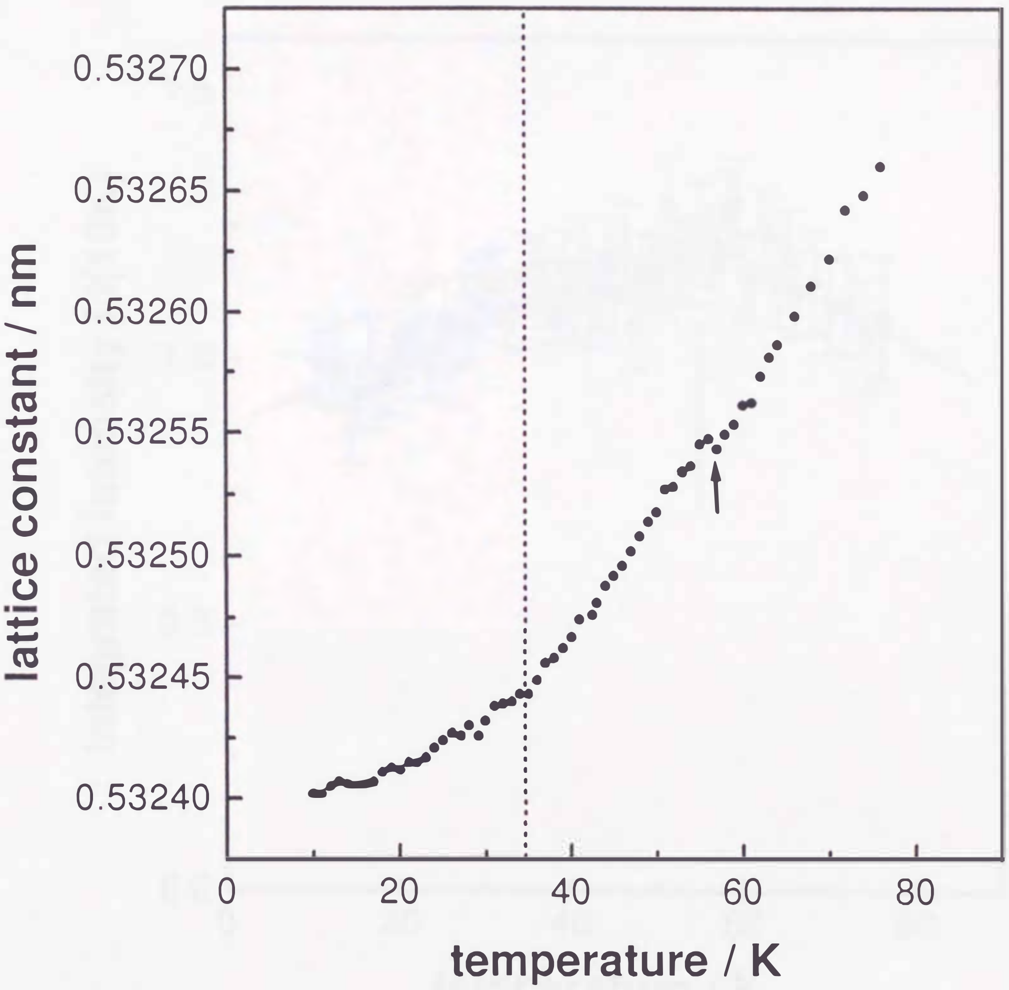

Figure 36: The temperature dependence of the lattice constant a. The Dotted line and the arrow indicate T_c(=35 K) and discontinuous behavior of the lattice constant, respectively.

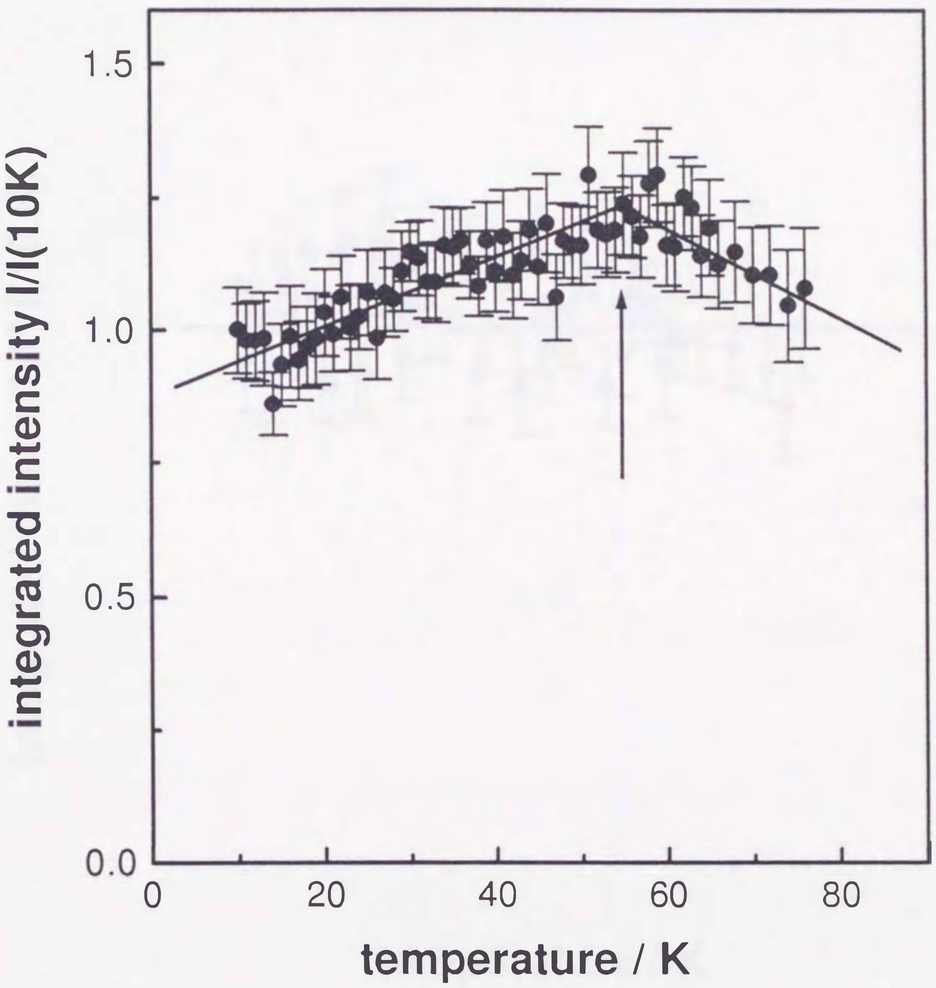

Figure 37: Integrated intensity of the 0 0 14 diffraction as a function of temperature. The lines are guides for the eye. Arrow indicates the temperature at the maximum value.

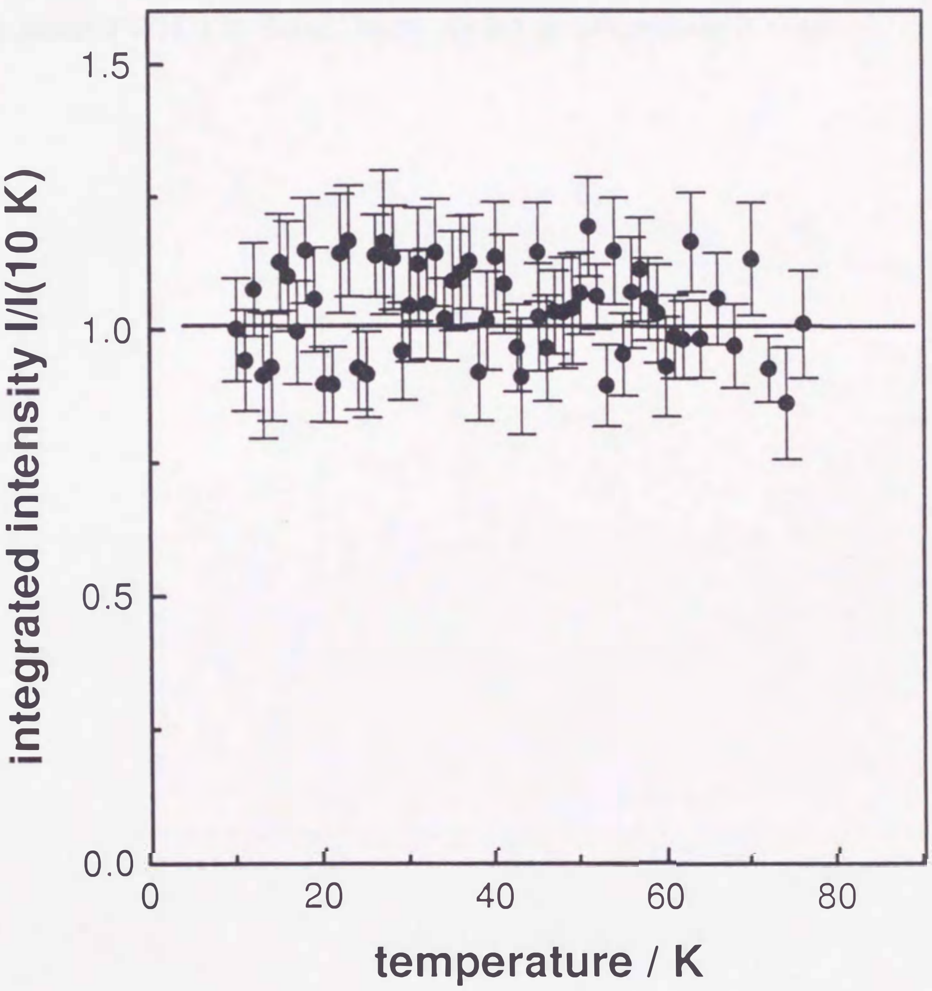

Figure 38: Integrated intensity of the 6 0 0 diffraction is shown as a function of temperature. The line is a guide for the eye.

FWHM

The temperature dependences of FWHM observed in the present measurements are shown in Figs. 39 and 40. The width of the rocking curve indicates the deviation of lattice cnstants in specimen. FWHM of the 0 0 14 diffraction tends to increase below T$_c$, while that of the 6 0 0 diffraction is not dependence of temperatureor. In order to discuss about FWHM in detail, more precise measurements is required.

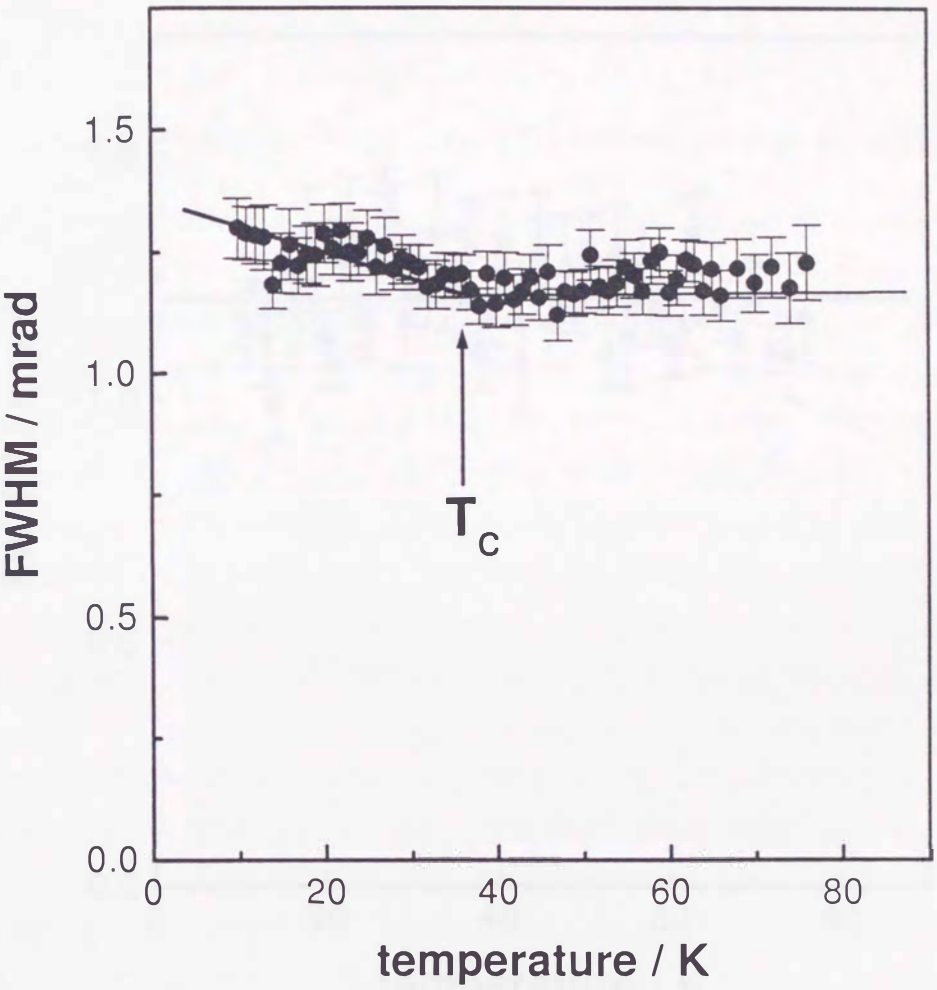

Figure 39: FWHM of the 0 0 14 diffraction as a function of temperature. The lines are guides for the eye, and the arrow indicates the temperature where the behaviour of FWHM changes.

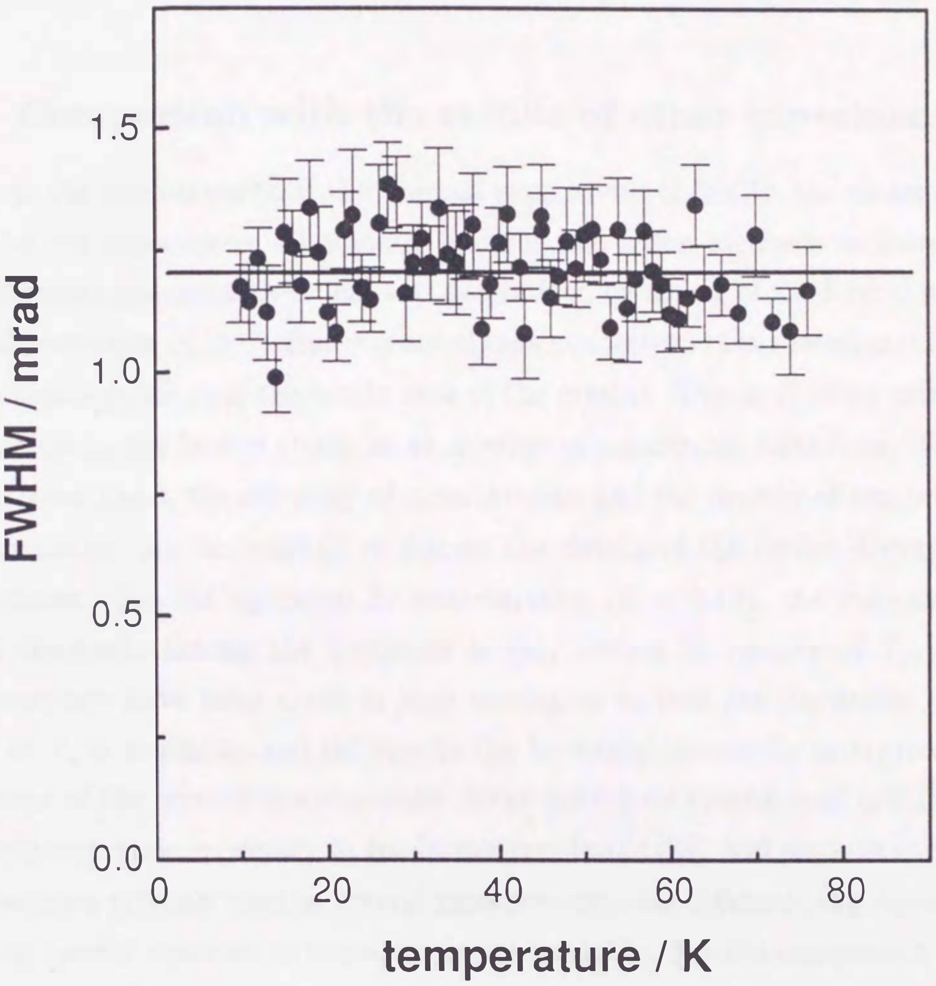

Figure 40: FWHM of the 6 0 0 diffraction as a function of temperature. The line is a guide for the eye.

5 Discussion

In this section, we discuss the lattice distortion observed in the present investigation comparing with that reported in literature. Then the characters of HTT-to-LTO phase transition and the superconducting transition will be discussed in terms of the lattcie distortion.

5.1 Comparison with the results of other experiments

So far as the measurement of the thermal expansivity of LSCO, the measurements were made by the capscitance dilatometer and the diffraction methods as listed in Table 1. The thermal expansion coefficient was determined by means of the former method in the relative resolution of 10^{-9}. But it is not always guaranteed that specimen is single crystal, and is mono–pahse over the whole area of the crystal. This may bring underestimation of a change in the lattice strain as an average of anisotropic behaviour. For the latter, on the ohter hand, the accuracy of measurement and the density of temperature points of examination are not enough to discuss the details of the lattice distortion. In fact, in specimen with the optimum Sr concentration ($x = 0.15$), the inconsistency of the lattice constants among the literature is very serious in vicinity of T_c. The present measurements have been made in high resolution so that the discussion on the lattice strain at T_c is available, and the results can be straightforwardly interpreted as the real behaviour of the crystallographic state. Since the lattice constants of LSCO are sensitive to Sr concentration,especially in the lattice constant c [25], and since Sr concentration of the specimen crystals used in several measurements are different, the direct comparison with the results reported in literature is not available. For the comparison of the lattice strains, a use of relative change in the lattice constant from that at 10 K, i.e. $[X(T) - X(10K)]/X(10K)$ for X= a ,b and c, is practical. The temperature dependences of the lattice strains of c and a obtained in the present experiment are shown in Figs. 41 and 42, together with those calculated from other measurements listed in Table 1. The results reported by Ono and Narita [16] are entirely different from the present results on both c and a. The reason for the inconsistency may be attributed to the use of the powder measurement in the reference: in general, in powder specimens, homogenity of temperature, internal and external stresses, the quality of crystal particles and so on, is less than that in a single crystal. Though they suggest that the anomaly of the lattice constants in vicinity of T_c is attributed to the structural phase transition preceding the

Table 12. Critical exponent β determined by various measurements and theory.

sample	item	β	ref.
$La_{1.97}Sr_{0.03}Cu_{0.95}Li_{0.05}O_{4-\delta}$	superlattice peak	0.29 ± 0.04	[36]
$La_2Cu_{0.95}Li_{0.05}O_{4-\delta}$	superlattice peak	0.275 ± 0.04	[36]
$La_{1.906}Ba_{0.047}CuO_{4-\delta}$	spontaneous strain	0.33	[5]
$La_{1.89}Sr_{0.110}CuO_4$	spontaneous strain	0.35	present work
$La_{1.857}Sr_{0.143}CuO_4$	spontaneous strain	0.37	present work
3-D XY model	—	0.351 ± 0.002	[37]

appearance of superconductivity, it seems to be physically unreasonable since the lattice constants is quite sensiteive to the temperature even below 30 K: the relative change of the lattice strains below T_c are 1.00×10^{-4} in c and 1.35×10^{-4} in a respectively. Such large change expected to be observed by the present STOE measurement, however, there is no remarkable change in both c and a. On the other hand, Maeta *et al.* [17] had made the measurement of c with a single crystal by means of X-ray Bond method in a relative accuracy of 2×10^{-6}. A subtle difference from the present result is observed aroud T_c, but the qualitative behaviour above T_c is almost consistent with the present results.

The anomalous behaviour of c around T_c such as the present study, has also been observed in other high-T_c superconductors, for example, $YBa_2Cu_3O_{7-\delta}$ (YBCO) [29] and $Bi_2Sr_2Ca_2Cu_2O_8$ (BSCCO) [30]: the origin of the anomaly is considered as two kinds of effect: a structural phase transition accompanying the onset of superconductivity and the lattice fluctuation expressed by coupling the order parameter with the lattice strains.

5.2 HTT-to-LTO phase transition

The structural phase transition from the HTT-to-LTO phases is caused by a softening of a transverse-optic-phonon mode at the X point in Brillouin zone [38] and is characterized by the freezing of rotation mode of the CuO_6 octahedra around the [0 1 0] direction. In addition, there is a deformation of the base of octahedron being due to the occurence of the orthorhombic distortion $b > a$ [20]. According to Cava *et al.* [39], the deformation is attributed to the distortion of CuO_2 square lattice into the rectangular lattice. The pattern of the distortion of CuO_2 plane in the LTO phase is shown in Fig. 43(b). In the figure, ψ_1 and ψ_2 denote the rotation angle of the octahedron and the

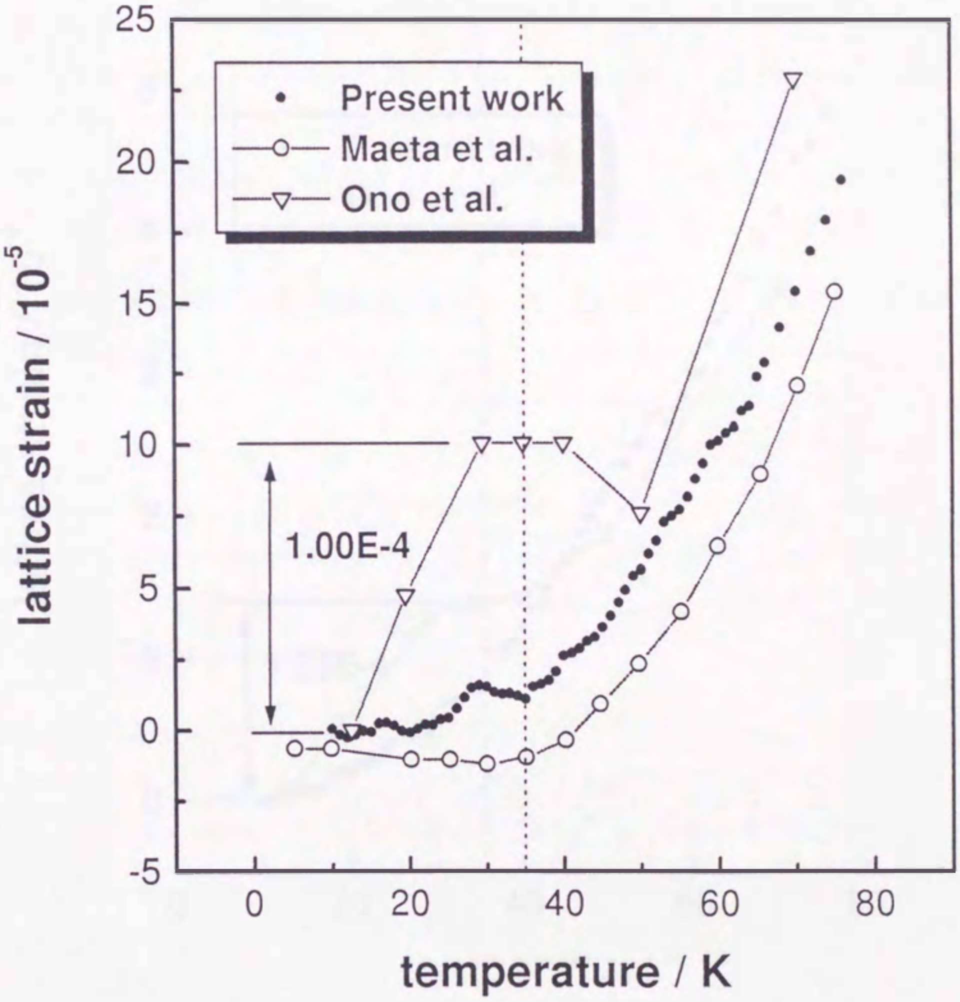

Figure 41. The comparison of the temperature dependence of the lattice strain c.

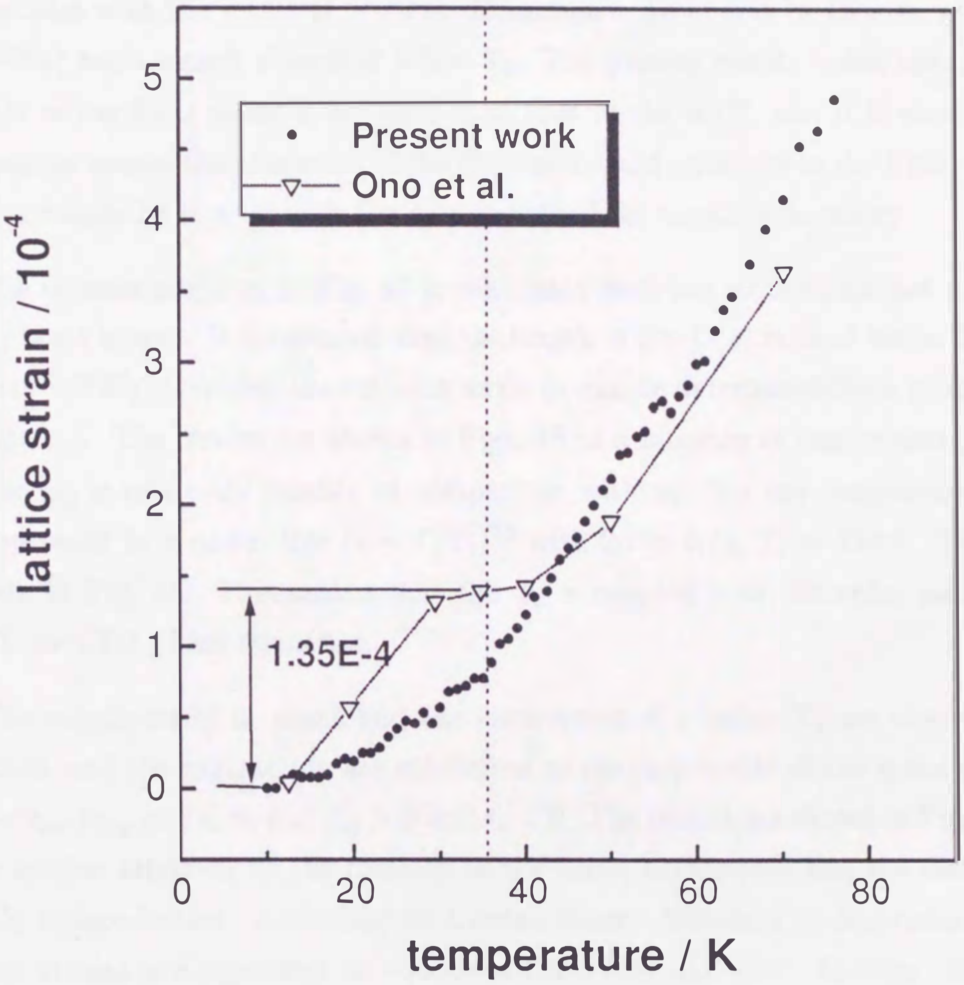

Figure 42. The comparison of the temperature dependence of the lattice strain of a.

scissors angle between O(1)–Cu–O(1)' bonds respectively. Since \$$\psi_1$ is very small, the Cu–O(1) bond length is calculated from the lattice constants a and b as $\sqrt{a^2+b^2}/4$ in good approximation, and is shown in Fig. 44 as a function of temperature. The results of the structural analysis by Braden *et al.* [20] and Cava *et al.* [39] are also shown in the figure. The bond length is linearly decreasing with decreasing temperature in the HTT phase, and shows a smaller temperature depndence in the LTO phase. This does not contradict with the result of neutron–diffraction experiments by Braden *et al.* [20]: The Cu–O(1) bond length elongates below T_c. The present results mean that the Cu–O(1) bonds in the LTO phase is stronger than that in the HTT, and it is expected that the transition causes the alteration of the electronic band structure in the CuO_2 planes which may strongly be related with the appearance of the superconductivity.

The scissors angle ψ_2 in Fig. 43 is calculated with the lattice constant a and the Cu–O(1) bond length. It is assumed that the length of Cu–O(1) is fixed below T_s such in the case of $SrTiO_3$, therefore the rotation angle ψ_1 can be determined from ψ_2 and the lattice constant b. The results are shown in Figs. 45 as a function of temperature. The change in the ψ_2 is relatively smaller in comparison with ψ_1, but the temprature dependence is expressed in a power low $(1-T/T_s)^{2\beta}$ with $2\beta = 0.78$, $T_s = 184.8$. The results are shown in Fig. 46. This means that the ψ_2 is coupled with the order parameter ψ_1 of HTT–to–LTO phase transition.

The expansion of in–plane and the contraction of c below T_s are observed. The expansion and the contraction are attributed to the increments of the spontaneous strains $\epsilon_{ab} = \epsilon_{xx} + \epsilon_{yy}$ and $\epsilon_c = \epsilon_{zz}$: $\epsilon_{ab} > 0$ and $\epsilon_c < 0$. The results are shown in Fig. refatrainA2. The strains attribute to the rotation of the CuO_6 octahedron and the distortion of the CuO_2 square lattice. According to Landau theory described in Appendix, the spontaneous strains are expressed as equations (22), (23) and (24). In Figs. 48 and 49, the spontaneous strains ϵ_{xy} of specimen A and B are shown as a function of reduced temperature $(1-T/T_s)$. Where the $\epsilon_{xy} = 2(b-a)/(a+b)$ is considered as the order parameter as mentioned by Böni *et al.* [38]. The spontaneous strain of both specimens can well be described by a power law $(1-T/T_s)^{2\beta}$ with $\beta = 0.37$ and 0.35(see Table 12), the transition temperature $T_s = 185.4(5)$ and 273.6(7) K, respectively. The determined β value is in good agreement with the theoritical one of $\beta = 0.351 \pm 0.002$ for the three–dimensional XY model with cubic anisotropy [40], and therefore, the HTT–to–LTO structural phase transition shows three–dimensional feature . The present values are consistent with that of LBCO with the optimum barium content, while is inconsistent with the β of the

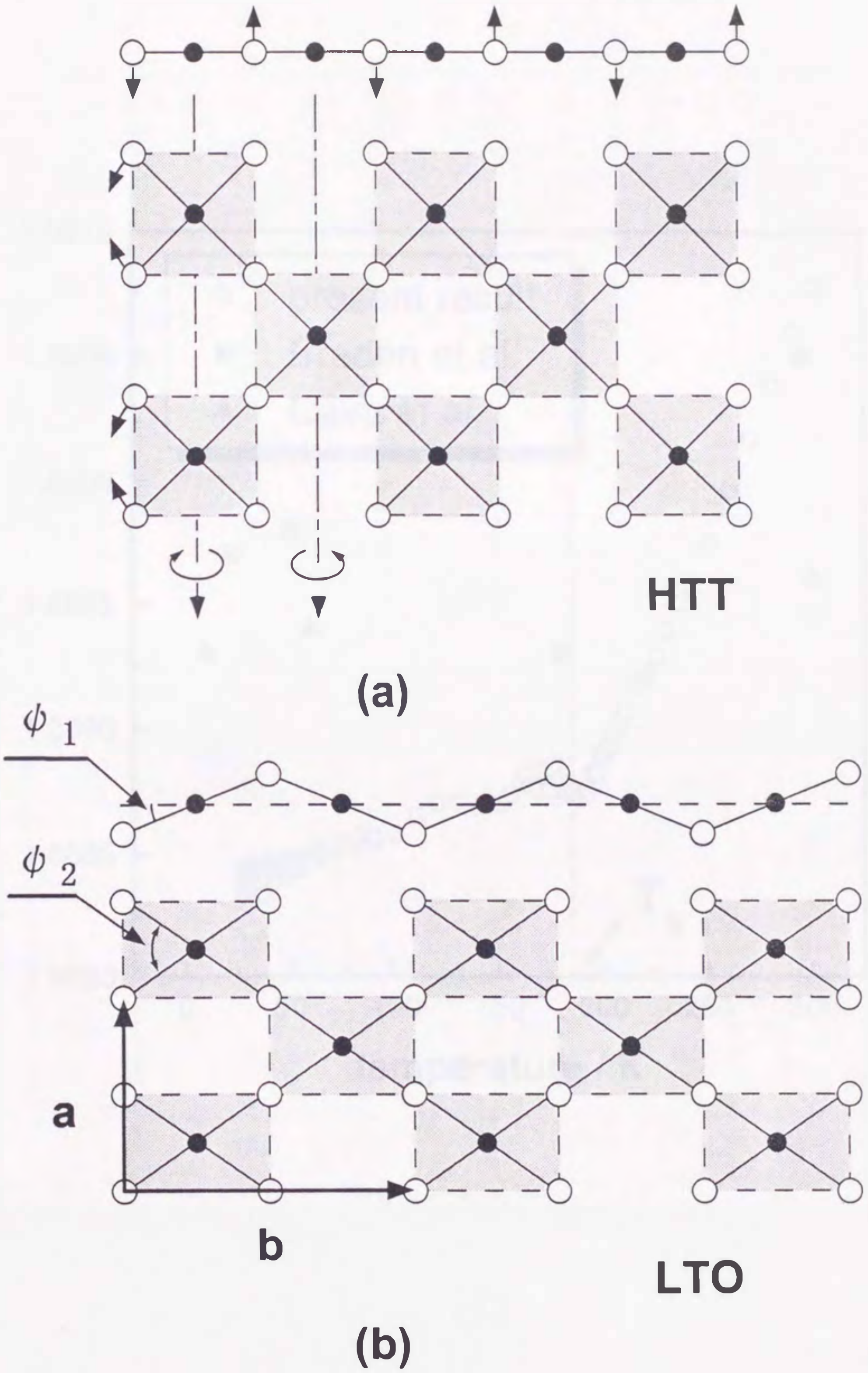

Figure 43: Projection on *ac* and *ab* planes of CuO_6 octahedron. (a) in HTT and (b) in LTO phases. ψ_1 and ψ_2 denote the rotation angle of the octahedoron and the scissors angle between O(1)–Cu–O(1)' bonds.

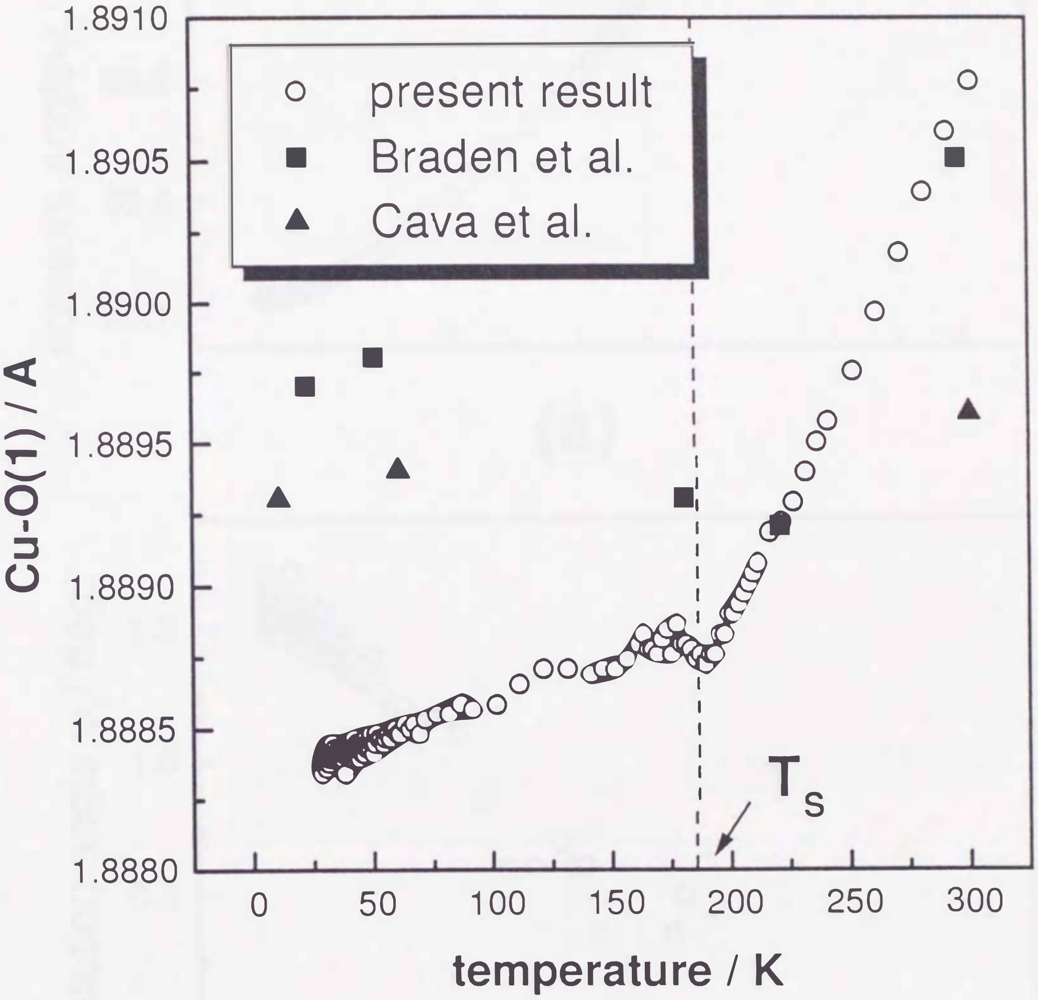

Figure 44. The temperature dependence of the Cu–O(1) bond length.

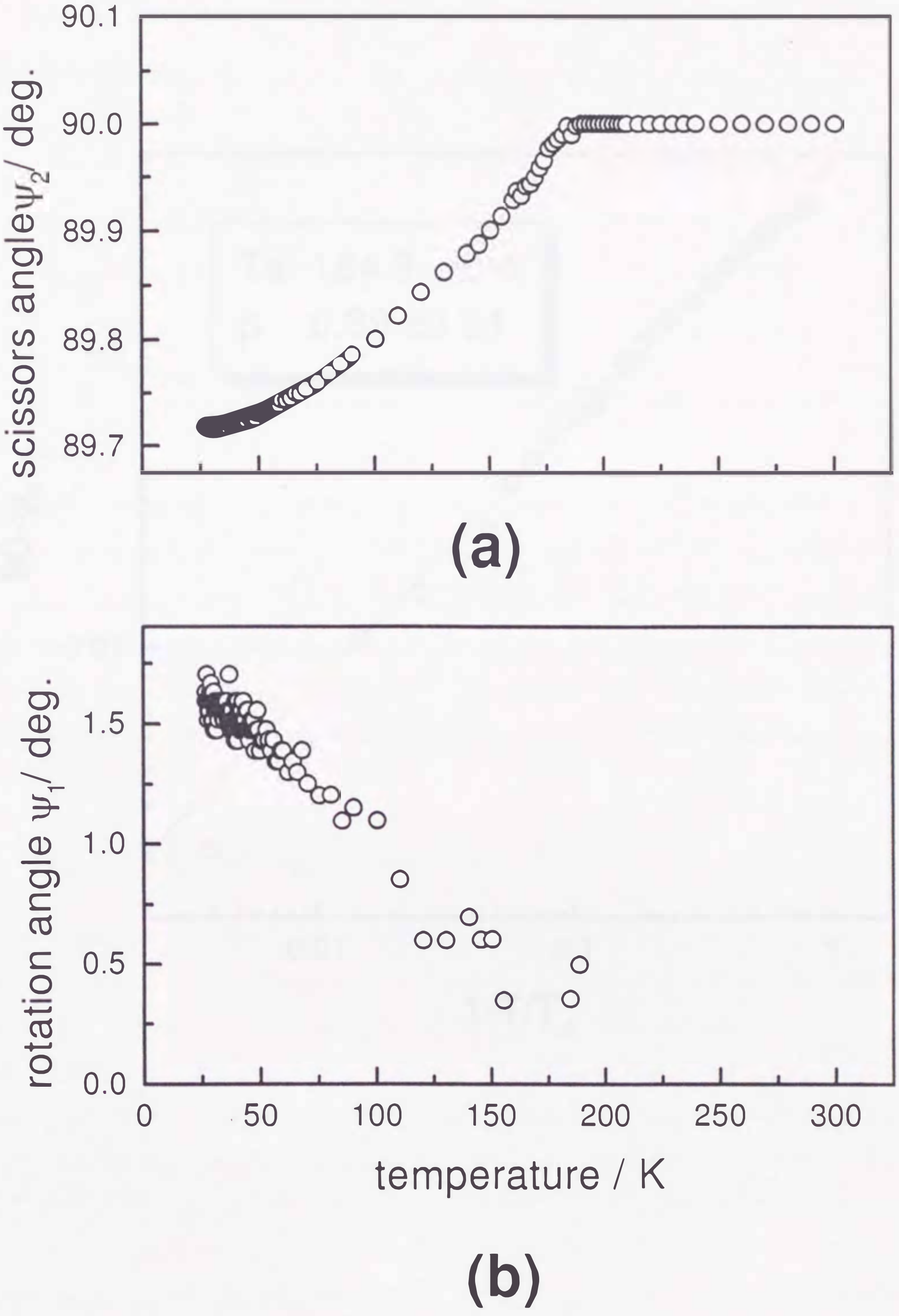

Figure 45: The temperature dependence (a) of the scissors angle ψ_2 and (b) of the rotation angle ψ_1.

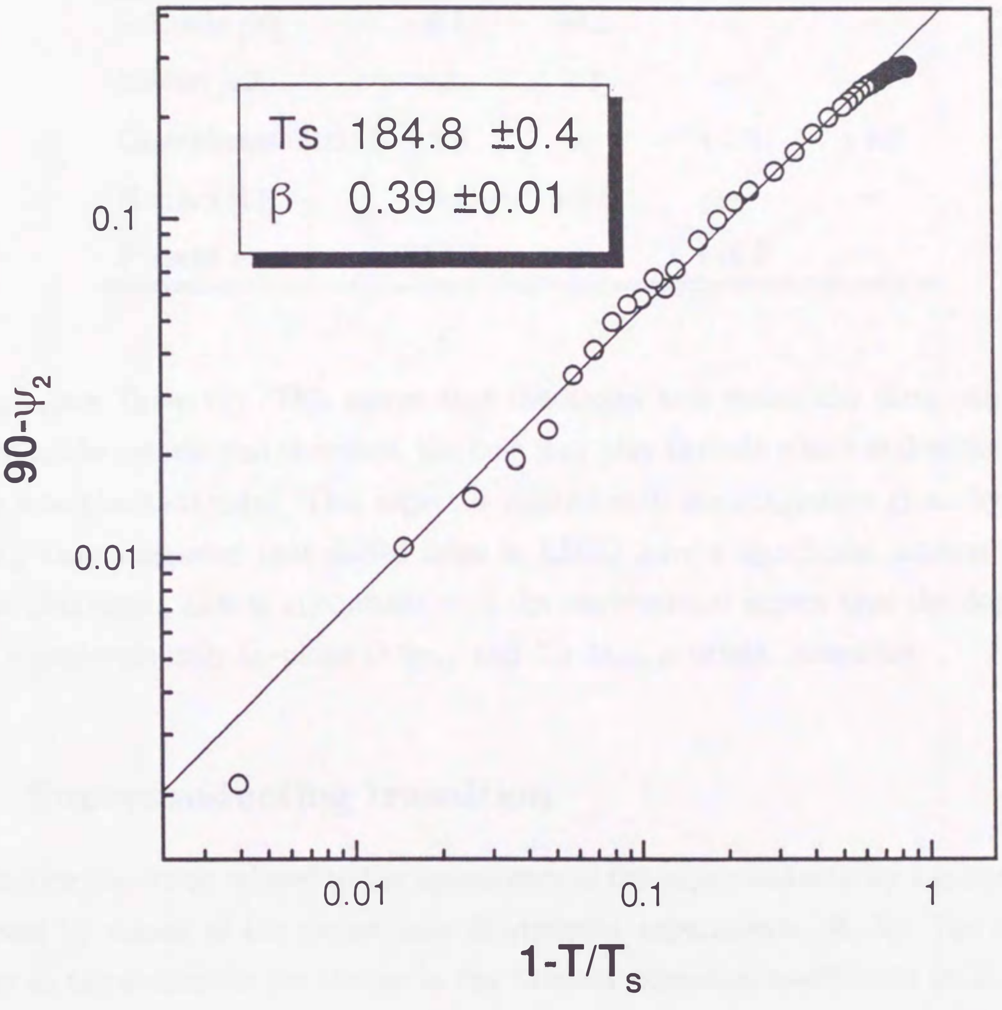

Figure 46: Scissors angle 90-ψ_2 as a function of reduced temperature in full logarithmic scale.

Table 13: The comparison of calculated the uniaxial stress dependences of T$_c$ with other result. The unit is K/GPa. dT_c/dP_{ab} is the calculated results of [100] direction in the twinning crystal.

Authers	dT_c/dP_c	dT_c/dP_{ab}	dT_c/dT_a	dT_c/dP_b
Schnelle [39]	-6.7	$+6.2$	—	—
Maeno [40]	-2	$+3$	—	—
Gugenberger [16]	-6.8	—	$+2.5$	$+4.9$
Nohara [11]	-6.5	$+3.8$	—	—
Present work	-10.8	—	$+18.9$	—

La_2CuO_4(see Table 12). This means that the doped hole makes the three-dimensional feature in the system and therefore, the hole may play the role which makes the bonding of the interplane stronger. This aspect is related with the suggestion given by Chen *et al.* [41]; they suggested that doped holes in LSCO have a significant amount of O $2p_z$ orbital character. This is in contrast with the conventional aspect that the doped holes show a predominantly in-plane O $2p_{x,y}$ and Cu $3d_{x^2-y^2}$ orbital character.

5.3 Superconducting transition

The lattice distortion related to the appearance of the superconductivity has been clearly observed by means of the capacitance dilatometer experiments [4, 5]. The distortion apears as the discontinuous change in the thermal expansion coefficients at T$_c$, and the uniaxial stress dependences of T$_c$ calculated from these values on the basis of Ehrenfest relation quantitatively agree with the results of direct measurement of dT_c/dp [36]. This suggests the strong coupling between the electron state and the lattice system. The linear thermal expansion coefficients calculated from the present results are shown in Fig. 50; the coefficients are calculated by differeciating the measured lattice constants after smoothed by the B-spline function. In the figure, the dotted lines indicates base line which is extrapolated from the normal state. Subtracting the base line from the obtained thermal expansion coefficients, $\Delta\alpha$ of the superconducting state below T$_c$ is given as shown in Fig. 51. In the figures, it is evident that $\Delta\alpha_a$ exhbits a broaden positive peak at T$_c$. On the other hand, α_c shows positive and negative peaks in vicinity of T$_c$. In

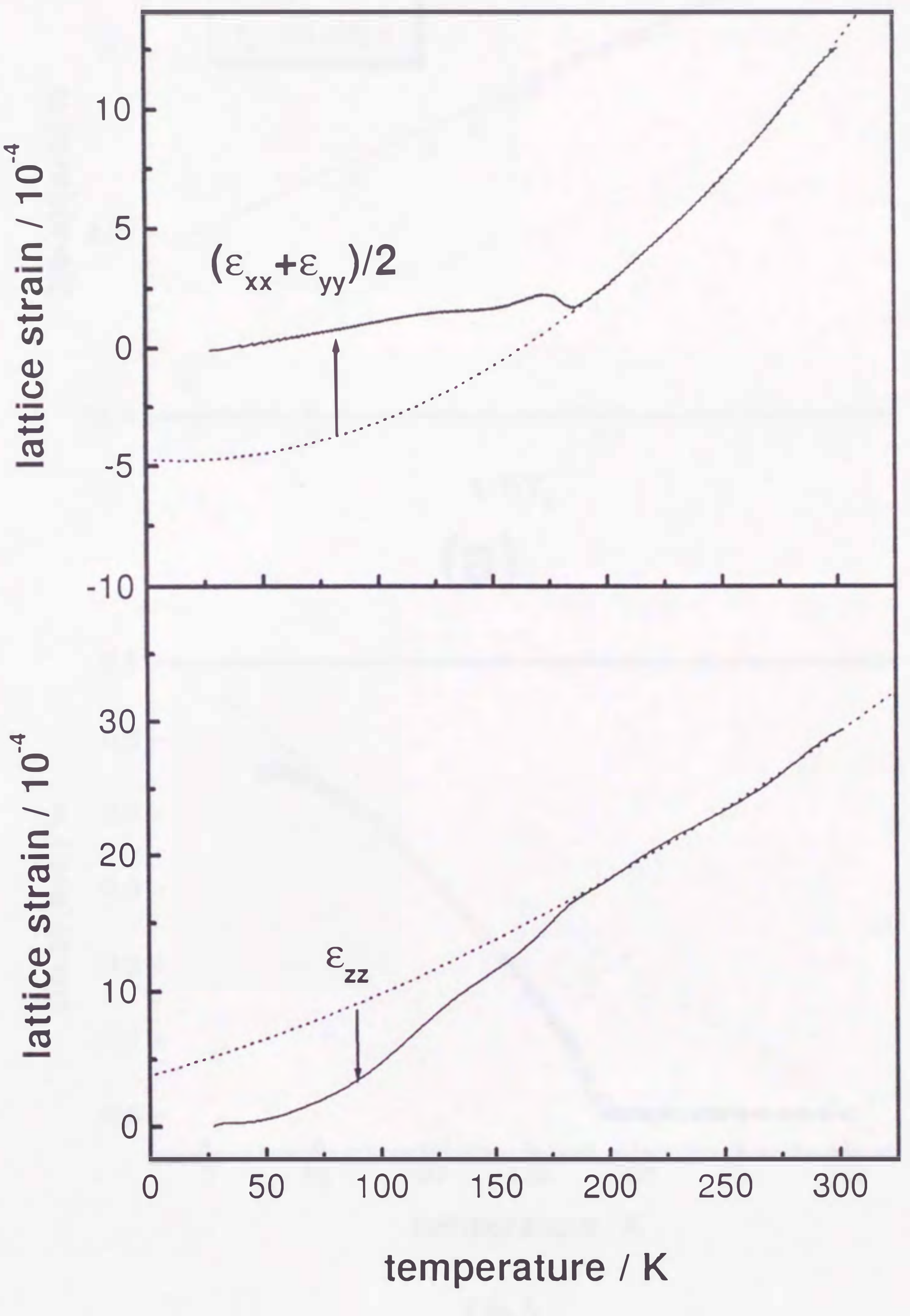

Figure 47: The definition of the lattice straines ϵ_{ij}. The dotted line is the calulation by linear least–squares fitting of the two–dimensional function with data above T_s.

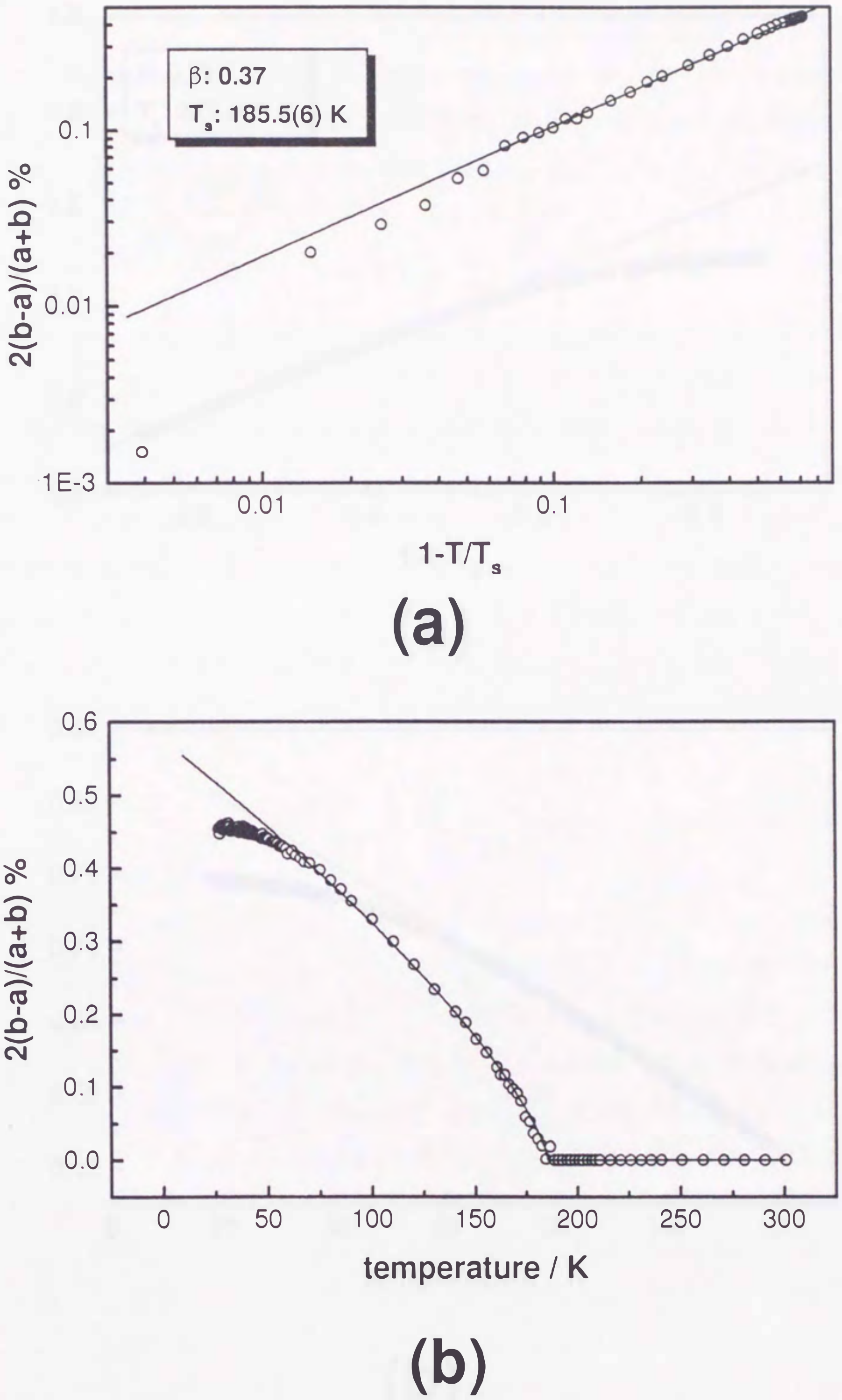

Figure 48: Spontaneous orthorhombic strain $2(b-a)/(a+b)$ due to the HTT–LTO structural phase transition (a) as a function of $(1-T/T_s)$ in full logarithmic scale and (b) as a function of T in normal scale in the specimen A.

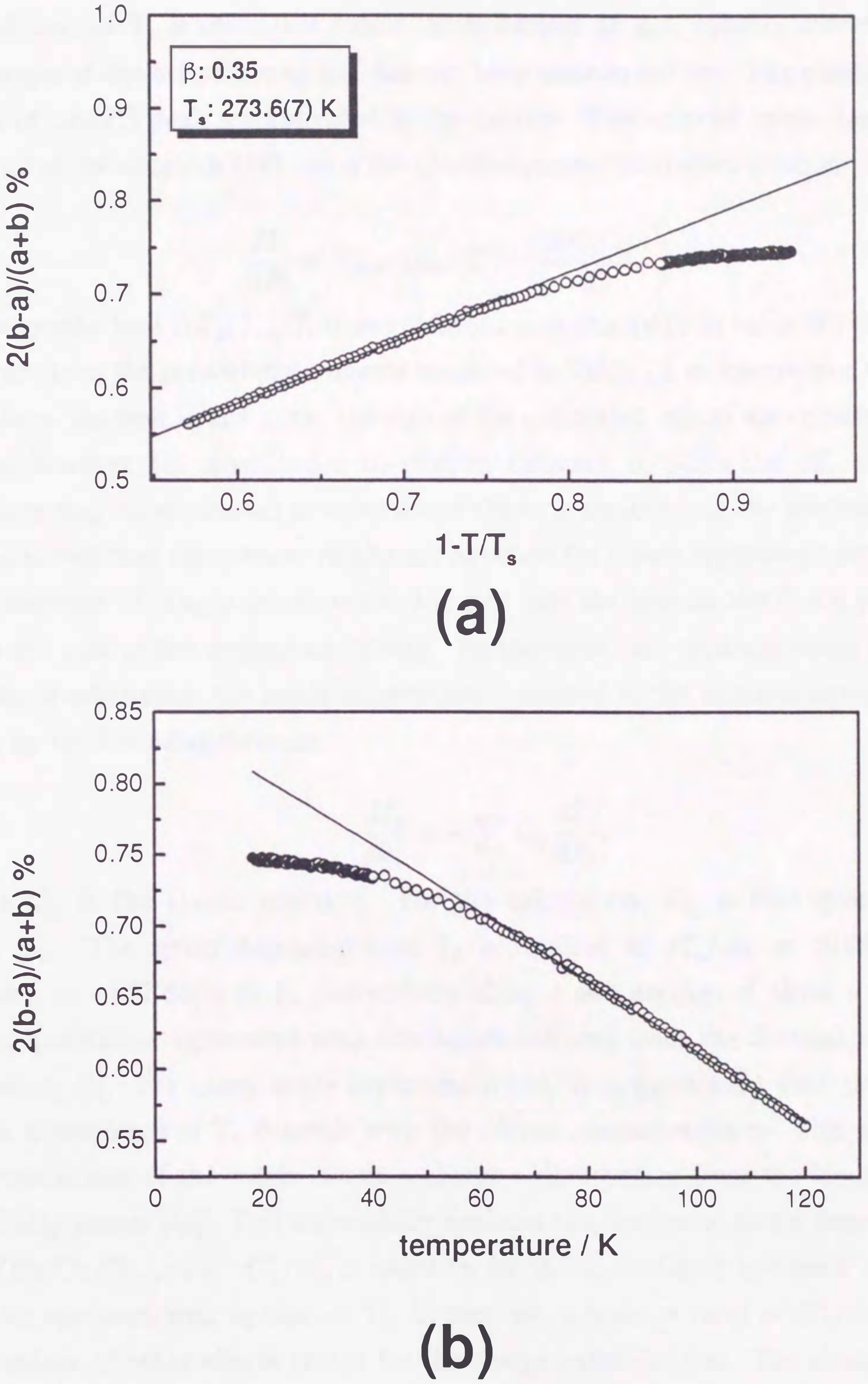

Figure 49: Spontaneous strain $2(b-a)/(a+b)$ as a function of (a) $(1-T/T_s)$ and (b) T in the specimen B.

comparison with repoted $\Delta\alpha$ given by the capacitance dilatometer experiments [5], the sign of $\Delta\alpha_a$ at T_c is consistent, while the behaviour of $\Delta\alpha_c$ entirely differs from them. The origin of the behaviour of $\Delta\alpha_c$ has not been understood yet. The magnitudes of the depth of $\Delta\alpha(T_c)$ peak are indicated in the figurers. The uniaxial stress dependences on T_c is given by equation (16) using the thermodynamic Ehrenfest relation:

$$\frac{dT_c}{dP_i} = V_{mol} \cdot \Delta\alpha_i(T_c) \cdot \left(\frac{\Delta C_p(T_c)}{T_c}\right)^{-1}, \tag{16}$$

where specific heat $\Delta C_p(T_c)/T_c$ shows discontinuous change in its value of 9.6 $(mJ/K^2 mol)$ [6]. The results in the present experiments are listed in Table 13, in comparison with those in literature. As seen in the table, the sign of the calculated values are consistent with the others, however, the magnitudes are entirely different, in particular dT_c/dP_a. The discrepancy may be attributed to existence of the twin structure in the specimen crystal: it is guaranteed that the present results are obtained for *a* pure crystallographic state. The large decrease of $\Delta\alpha_a$ is attributed to the fact that the hole on the CuO_2 planes mainly plays the role of the superconductivity. Furthermore, the uniaxial strain dependences $dT_c/d\epsilon_i$ is calculated: the strain dependence is related to the uniaxial stress dependence of T_c by the following formula:

$$\frac{dT_c}{d\epsilon_i} = -\sum_j C_{ij}\frac{dT_c}{dP_j}, \tag{17}$$

where C_{ij} is the elastic constant. For the calculation, C_{ij} is that given by Nohara *et.al.* [6]. The strain dependence of T_c is resulted in $dT_c/d\epsilon_c = 2160.8(>0)$ and $dT_c/d\epsilon_{ab} = -537.64(<0)$ K, respectively along c and average of along a and b: these are in qualitative agreement with the values deduced from the thermal expansion experiments [5]. For many oxide superconductors, it is mentioned that the sign of the strain dependence of T_c depends with the carrier concentration p. This is due to that the contraction of the c axis causes a charge redistribution from the blocking layers to the CuO_2 planes [44]. This successfully explains the feature of strain dependence of T_c for $YBa_2Cu_3O_{6+y}$; i.e. $dT_c/d\epsilon_c$ is negative for the underdoped specimen and is almost zero for specimen with optimized T_c. In contrast, a positive value of $dT_c/d\epsilon_c$ suggests an importance of other effects except for the charge redistribution. The strain dependence of T_c in LSCO is probably related with a coupling of deformation and tilt of the CuO_6 octahedra. According to the thermal expansion experiments under hydrostatic pressure [45], T_c increases with incresing the pressure in the LTO phase, which is decreasing with increasing pressure and is constant in the HTT phase. This means that T_c incrases when the tilt of the CuO_6 octahedra is reduced. The reduction of the tilt accompanies a contraction of the ab plane ($\epsilon_{ab} < 0$) and an elongation of the c axis ($\epsilon_c > 0$). Therefore, the signs of $dT_c/d\epsilon_{ab} < 0$ and $dT_c/d\epsilon_c > 0$ are consistent with the result of the thermal expansion experiment. The correlation of the tilt of the CuO_6 octahedra with superconductivity is also found by neutron experiment [4] and ultrasonic experiment [6]. By considered the property of Cu–O(1) bond length at the HTT–to–LTO phase transition, it is concluded that the tilt and the deformation of the CuO_2 plane causes the electronic correlations and changes T_c.

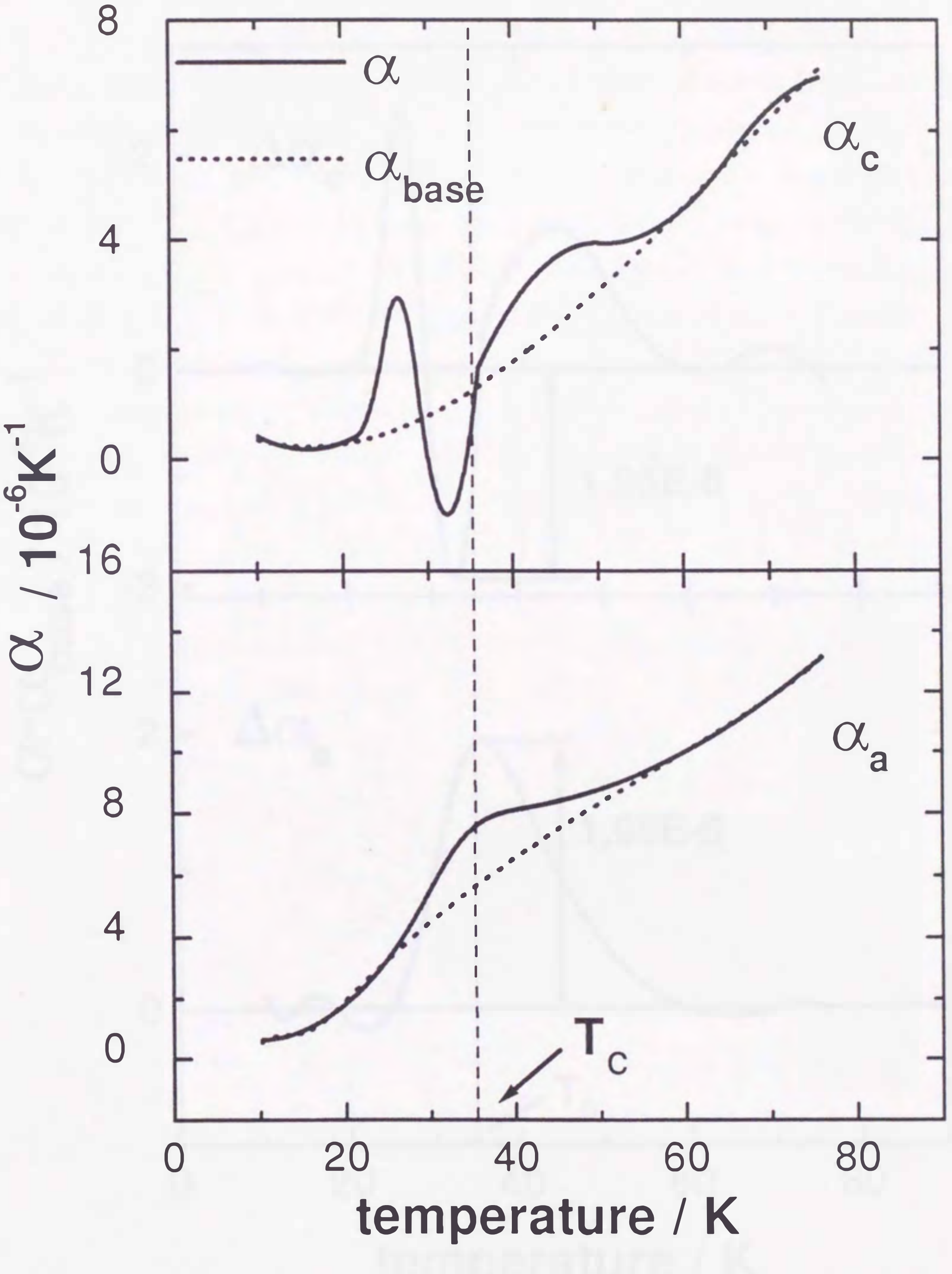

Figure 50: Linear thermal expansion coefficience in a and c. The dotted lines are the base line, explained in the text.

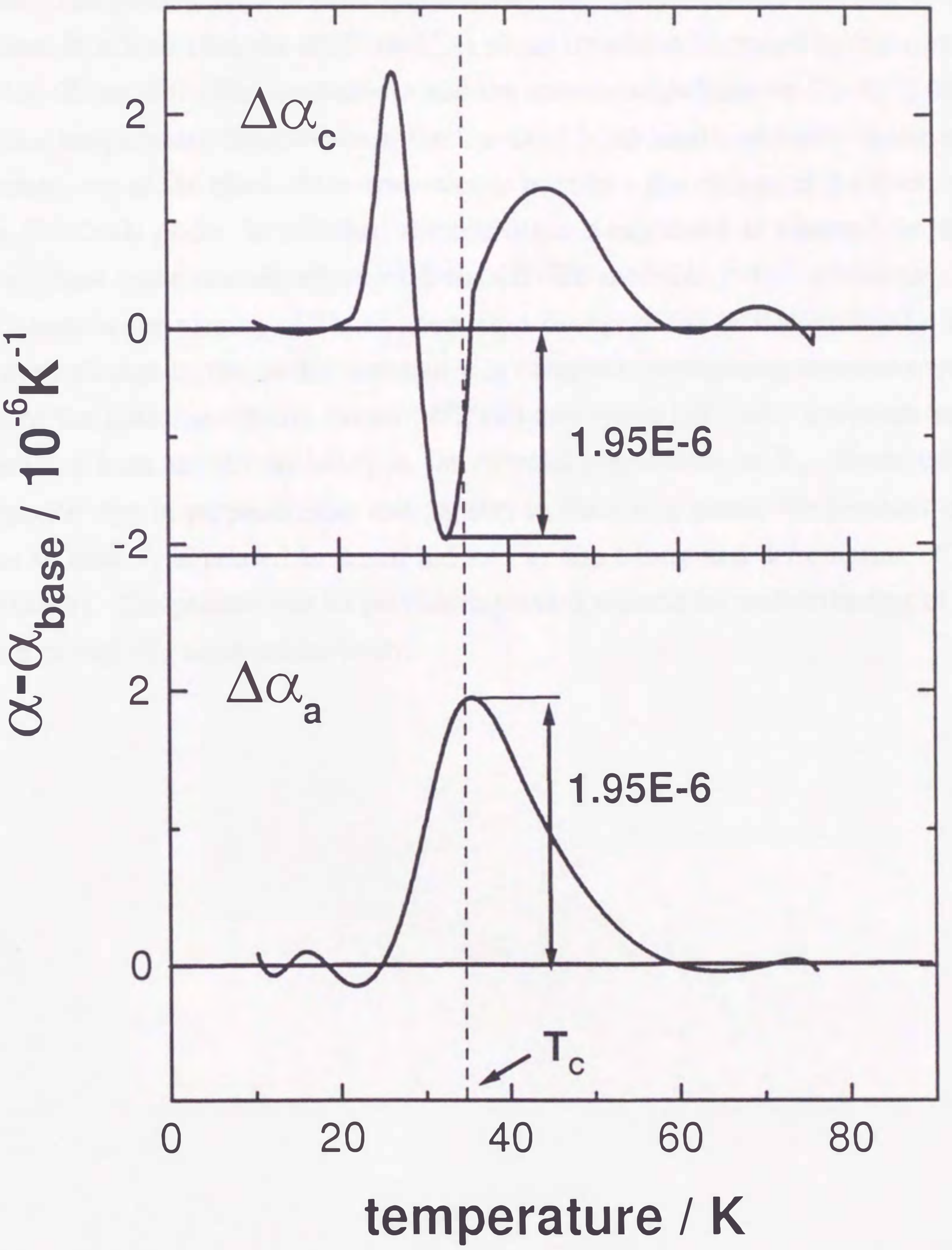

Figure 51. The behaviour of the anomaly of thermal expansion coefficient, $\Delta\alpha(\mathrm{T}_c)$.

6 Conclusion

The high–resolution X–ray diffraction measurements of the temperature dependence of the lattice constants of high T$_c$ superconductor La$_{2-x}$Sr$_x$CuO$_4$ with single crystals have been made. The present data is both qualitatively and quantitatively superior to the previous one. It is fond that the HTT–to–LTO phase transition is caused by the combination of the tilting of the CuO$_6$ octahedra and the scissors angle between Cu–O(1) bond and that the temperature dependence of the Cu–O(1) bond length abruptly changes at T$_s$. Therefore, one of the effect of the transition is to induce the change of the electronic system on the CuO$_2$ plane. In addition, the transition is explained as a second–ordered ferroelastic phase transition described with the 3D–XY model in cubic anisotropy. On the other hand, in the vicinity of T$_c$, an anomalous change of the lattice constant c and a subtle slope change in the lattice constant a is observed. Estimating thermal expansivities from the lattice constants, strain ($dT_c/d\epsilon_i$) and stress (dT_c/dP_i) dependences of T$_c$ are deduced from the discontinuity in the thermal expansivity at T$_c$. These values take a opposite sign in perpendicular and parallel to the CuO$_2$ plane. We revealed that this is due to that T$_c$ is related to strain induced by the tilting and deformation of the CuO$_6$ octahedra. The present results provide important aspects for understanding of the mechanism of high–T$_c$ superconductivity.

Acknowledgements

The author is grateful to Assoc. Prof. Y. Soejima, the superoisor, and Professor Emeritus A. Okazaki for their guidance of the research and many suggestions for improving manuscript, and is indebted to Prof. H. Kojima and Dr. I. Tanaka for offering the crystal. A part of experiments was carried out at the Centre of Advanced Instrumental Analysis, Kyushu University; the author is grateful to Dr. H. Sakashita of the Centre, who assembled the HADOX diffractometer, for valuable comments and advise. Thanks are also due to Miss C.Konishi and Mr. M. Ohtsu for their collaboration and discussions, to Dr. T. Eto, Messrs. K. Munakata, Y. Fujii, K. Yamasaki and S. Kuwajima for their assistance and discussions, and to Drs. Z. Lu, A. Kohno, Messrs. S. Nagao, H. Naruoka, K. Hirakawa, T. Ninomiya, T. Toda, T. Kakinaga, T. Nogami, Y. Nakao, T. Itoh and M. Sakata for encouragements. The author also thanks to all at the administrative office of the Department of Physics for the supports and to all at the Workshop of the Faculty of Science for preparing devices. The present reseaches are collaborated with Proffessor K.-H. Ehses, University of Saarland, Germany.

Appendix

The discussion of the structural phase trainsition in LSMO (M=Sr, Ba, Ca) compounds on the basis of Landau–Ginzburg free energy has been made by many authors [10, 11, 37]. The free energy F consist of the summation of three components, $F = F_0 + F_S + F_C$: F_0 is a power series expansion of the order parameter, F_S the elastic energy due to strains, and F_C the coupling between the order parameter and the spontaneous strain. Using the results given in Ref. [37], the components are given as following:

$$F_0 = \frac{1}{2}a(T - T_s)(Q_1^2 + Q_2^2) + u(Q_1^2 + Q_2^2)^2 + v(Q_1^4 + Q_2)^4 + \dots, \tag{18}$$

and

$$F_E = \frac{1}{2}C_{11}(\epsilon_{xx}^2 + \epsilon_{yy}^2) + \frac{1}{2}C_{33}\epsilon_{zz} + C_{12}\epsilon_{xx}\epsilon_{yy} + C_{13}\epsilon_{zz}(\epsilon_{xx} + \epsilon_{yy}) + \frac{1}{2}C_{44}(\epsilon_{yz}^2 + \epsilon_{zx}^2) + \frac{1}{2}C_{66}\epsilon_{xy}^2, \tag{19}$$

and

$$F_C = \gamma_1(\epsilon_{xx} + \epsilon_{yy})(Q_1^2 + Q_2^2) + \gamma_2\epsilon_{zz}(Q_1^2 + Q_2^2) + \gamma_3\epsilon_x y(Q_1^2 - Q_2^2), \tag{20}$$

where Q_1 and Q_2 are the components of the order paremeter, γ_j the coupling energies, C_{ij} and ϵ_{ij} are the strain and the elastic moduli on the basis of the HTT notation (I4/mmm). This model is well known as the universality class with $d = 3$, XY model with cubic anisotropy [37, 38]. On cooling, the system becomes unstable for temperature $T - T_s \leq 0$. The HTT–LTO phase transition (SPT) is characterized by the order parameter change from $Q_1 = Q_2 = 0$ to either $Q_1 \neq 0$ and $Q_2 = 0$ or $Q_1 = 0$ and $Q_2 \neq 0$, corresponding to the tilting of CuO$_6$ octahedra around [1 0 0] or [0 1 0] respectively [11]. The spontaneous strains in LTO phase are calculated from two condition of the elastic equillibrium $\partial F/\partial\epsilon_i j$, and $Q_1 \neq 0$ and $Q_2 = 0$, and the simultaneous equations can be obtained as

$$\begin{pmatrix} C_{11} & C_{12} & C_{13} & 0 & 0 & 0 \\ C_{12} & C_{11} & C_{13} & 0 & 0 & 0 \\ C_{13} & C_{13} & C_{33} & 0 & 0 & 0 \\ 0 & 0 & 0 & 1 & 0 & 0 \\ 0 & 0 & 0 & 0 & 1 & 0 \\ 0 & 0 & 0 & 0 & 0 & C_{66} \end{pmatrix} \begin{pmatrix} \epsilon_{xx} \\ \epsilon_{yy} \\ \epsilon_{zz} \\ \epsilon_{yz} \\ \epsilon_{zx} \\ \epsilon_{xy} \end{pmatrix} = -Q_1^2 \begin{pmatrix} \gamma_1 \\ \gamma_1 \\ \gamma_2 \\ 0 \\ 0 \\ \gamma_3 \end{pmatrix}. \tag{21}$$

These equation is solved as

$$\begin{pmatrix} \epsilon_{xx} \\ \epsilon_{yy} \\ \epsilon_{zz} \\ \epsilon_{yz} \\ \epsilon_{zx} \\ \epsilon_{xy} \end{pmatrix} = -Q_1^2 \begin{pmatrix} \frac{C_{13}}{C_{11}C_{33}+C_{12}C_{13}-2C_{13}^2}(\gamma_1 - \gamma_2) \\ \frac{C_{13}}{C_{11}C_{33}+C_{12}C_{13}-2C_{13}^2}(\gamma_1 - \gamma_2) \\ \frac{\gamma_2(C_{11}+C_{12})-2\gamma_1 C_{13}}{C_{11}C_{33}+C_{12}C_{13}-2C_{13}^2} \\ 0 \\ 0 \\ \frac{\gamma_3}{C_{66}} \end{pmatrix}. \tag{22}$$

According to Braden *et al.* [4], the spontaneous strains ϵ_{ij} is related to the orthorhombic lattice constants and the magnitudes of quadratically on Q_i as follows:

$$\epsilon_{xx} + \epsilon_{yy} = \left[\frac{a+b}{2a_t} - 1\right] \propto Q_i^2. \tag{23}$$

$$\epsilon_{zz} = \left[\frac{c}{c_t} - 1\right] \propto Q_i^2, \tag{24}$$

$$\epsilon_{xy} = \left[\frac{a-b}{2a_t}\right] \propto Q_i^2, \tag{25}$$

where a_t and c_t are the tetragonal lattice constants.

References

References

[1] J. B. Bednortz, and K. A. Müller, Z. Phys. **B46**, 189 (1986).

[2] C. Meingast, B. Blank, H. Bürkle, B. Obst, T. Wolf, H. Wühl, V. Selvamanickam and K. Salama, Phys. Rev. **B41**, 11299 (1990).

[3] C. Meingast, O. Kraut, T. Wolf, H. Wühl, A. Erb and G. Müller-Vogt, Phys. Rev. Lett. **67**, 1634 (1991).

[4] M. Braden, O. Hoffels, W. Schnelle, B. Büchner, G. Heger, B. Hennion, I. Tanaka, and H. Kojima, Phys. Rev. **B 47**, 12288 (1993).

[5] F. Gugenberger, C. Meingast, G. Roth, K. Grube, V. Breit, T. Weber, H. Wühl, S. Uchida, and Y. Nakamura, Phys. Rev. **B49**, 13137 (1994).

[6] M. Nohara, T. Suzuki, Y. Maeno, T. Fujita, I. Tanaka, and H. Kojima, Phys. Rev. **B 52**, 570 (1995).

[7] R. A. Fisher, J. E. Gordon, and N. E. Phillips, Annu. Rev. Phys. Chem. **47**, 283 (1996).

[8] H. Takagi, T. Ido, S. Ishibashi, M. Uota, S. Uchida, and Y. Tokura, Phys. Rev. **B40**, 2254 (1989).

[9] A. R. Moodenbaugh, Y. Xu, M. Suenaga, T. J. Folkerts, and R. N. Shelton, Phys. Rev. **B38**, 4596 (1988).

[10] T. Suzuki and T. Fujita, Physica **C 159**, 111 (1989).

[11] J. D. Axe, A. H. Moudden, D. Hohlwein, D. E. Cox, K. M. Mohanty, A. R. Moodenbaugh, and Y. Xu, Phys. Rev. Lett. **B62**, 2751 (1989).

[12] J. C. Phillips and K. M. Rabe, Phys. Rev. **B44**, 2863 (1991).

[13] A. Bianconi, N. L. Saini, A. Lanzara, M. Missori, T. Rossetti, H. Oyanagi, H. Yamaguchi, K. Oka, and T. Ito, Phys. Rev. Lett. **76**, 3412 (1996).

[14] N. L. Saini, A. Lanzara, H. Oyanagi, H. Yamaguchi, K. Oka, T. Ito, and A. Bianconi, Phys. Rev. **B55**, 12759 (1997).

[15] M. Nohara, T. Suzuki, Y. Maeno, T. Fujita, I. Tanaka, and H. Kojima, Phys. Rev. Lett. **70**, 3447 (1993).

[16] Y. Ono, and S. Narita, Jpn. J. Appl. Phys. **31**, L224 (1992).

[17] H. Maeta, T. Kato, F. Ono, K. Haruna, I. Tanaka, and H. Kojima, Physica C **185–189**, 1383 (1991).

[18] Z. J. Yang, M. Yewondwossen, F. A. Dunlap, D. J. W. Geldart, S. L. Yuan, T. Kimura, K. Kishio, and K. Kitazawa, Phys. Lett. **A197**, 439 (1995).

[19] T. Kamiyama, F. Izumi, H. Asano, H. Takagi, S. Uchida, Y. Tokura, E. Takayama-Muromachi, M. Matsuda, K. Yamada, Y. Endoh, and Y. Hidaka Physica **C 172**, 120 (1990).

[20] M. Braden, P. Schweiss, G. Heger, W. Reichardt, Z. Fisk, K. Gamayunov, I. Tanaka, and H. Kojima, Physica **C223**, 396 (1994).

[21] I. Tanaka and H. Kojima, Nature (London) **337**, 21 (1989).

[22] I. Tanaka, K. Yamane, and H. Kojima, J. Cryst. Growth **96**, 711 (1989).

[23] N. Aomine, H. Yamada, Y. Soejima, A. Okazaki, I. Tanaka, and H. Kojima, Jpn. j. Appl. Phys. **32**, 4959 (1993).

[24] Y. Fujii, Z. Lu, Y. Soejima, A. Okazaki, I. Tanaka, and H. Kojima, Jpn. J. Appl. Phys. **33**, 4593 (1994).

[25] P. G. Radaelli, D. G. Hinks, A. W. Mitchell, B. A. Hunter, J. L. Wagner, B. Dabrowski, K. G. Vandervoort, H. K. Viswanathan, and J. D. Jorgensen, Phys. Rev. **B 49**, 4163 (1994).

[26] A. Okazaki and N. Ohama, J. Appl. Cryst. **12**, 450 (1979).

[27] N. Ohama, H. Sakashita, and A. Okazaki, J. Appl. Cryst. **12**, 455 (1979).

[28] Y. Fujii, private communication.

[29] H. You, U. Welp, and Y. Fang, Phys. Rev. **43**, 3660 (1991).

[30] T. Asahi, H. Suzuki, M. Nakamura, H. Takano, and J. Kobayashi, Phys. Rev. B **55**, 9125 (1997).

[31] W. Dmowski, R. J. McQueeney, T. Egami, Y. P. Feng, S. K. Sinha, T. Hinatsu, and S. Uchida, Phys. Rev. B **52**, 6829 (1995).

[32] A. J. Millis and K. M. Rabe, Phys. Rev. B **38**, 8908 (1988)

[33] Y. Yagil and E. K. H. Salje, Physica C **229**, 152 (1994)

[34] H. You, J. D. Axe, X. B. Kan, S. Hashimoto, S. C. Moss, J. Z. Liu, G. W. Crabtree, and D. J. Lam. Phys. Rev. B **38**, 9213 (1988).

[35] H. J. Kim and R. Moret, Physica C **156**, 363 (1988).

[36] Y. Motoi, K. Fujimoto, , H. Uwe, and T. Sakudo, J. Phys. Soc. Jpn. **60**, 384 (1991).

[37] Wu Ting, K. Fossheim, and Laegreid, Solid State Commun. **75**, 727 (1990).

[38] P. Böni, J. D. Axe, G. Shirane, R. J. Birgeneau, D. R. Gabbe, H. P. Jessen, M. A. Kastner, and C. J. Peters, Phys. Rev. B **38**, 185 (1988).

[39] R. J. Cava, A. Santoro, D. W. Johnson, Jr. and W. W. Rhodes, Phys. Rev. **B35**, 6716 (1987).

[40] A. Aharony, Phys. Rev. B **8**, 4270 (1973).

[41] C. T. Chen, L. H. Tjeng, J. Kwo, H. L. Kao, P. Rudolf, F. Sette, and R. M. Fleming, Phys. Rev. Lett. **68**, 2543 (1992).

[42] W. Schnelle, O. Hoffels, E. Braun, H. Bricher, and D. Wohlleben, In *Physics and Materials Science of High Temperature Superconductors II, Vol. 209 of NATO Advanced Study Institute, Series E,* edited by R. Kossowsky, B. Raveau, D. Wohlleben, and S. Patapis (Kluwer Academic, Dordrecht, 1992), p. 151.

[43] Y. Maeno, S. Nakayama, M. Irie, Y. Tanaka, S. Nishizaki, M. Nohara, Y. Omori, Y. Kitano, and T. Fujita, in *Advances in Superconductivity VI,* edited by T. Fujita and Y. Shiohara (Springer–Verlag, Berlin, 1994), Vol. 1, p. 103.

[44] C. murayama, Y. Iye, T. Enomoto and N. Mori, Y. Yamada, T. Matsumoto, Y. Kubo, Y. Shimakawa and T. Manako, Physica C **183**, 277 (1991).

[45] N. Yamada and M. Ido, Physica C **203**, 240 (1992).

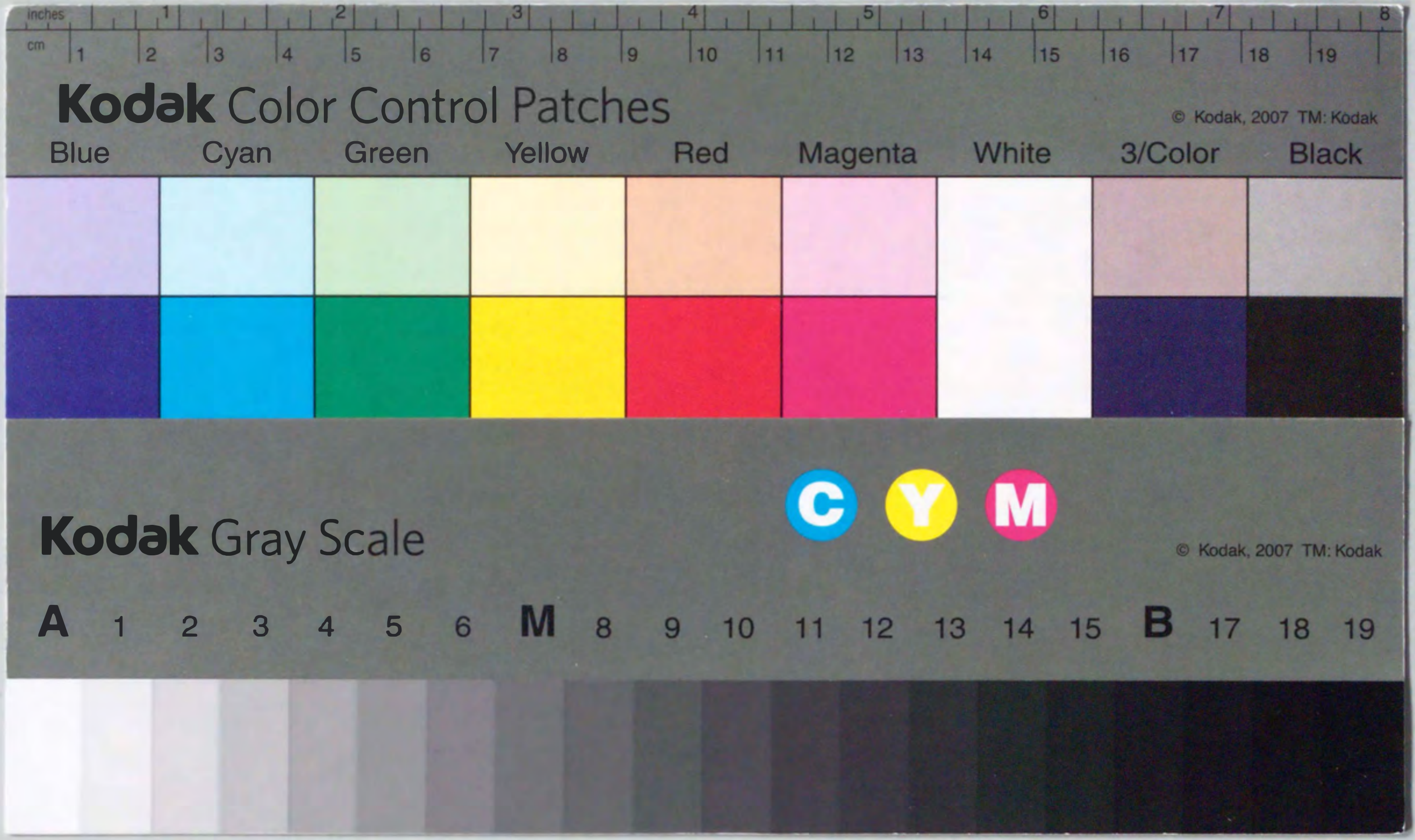
inches
1
2
3
4
5
6
7
8
cm
1
2
3
4
5
6
7
8
9
10
11
12
13
14
15
16
17
18
19
Kodak Color Control Patches
© Kodak, 2007 TM: Kodak
Blue
Cyan
Green
Yellow
Red
Magenta
White
3/Color
Black
C
Y
M
Kodak Gray Scale
© Kodak, 2007 TM: Kodak
A
1
2
3
4
5
6
M
8
9
10
11
12
13
14
15
B
17
18
19